

**Synthesis and Photoluminescence Properties of
Dysprosium Activated Full colour Emission
Phosphors**

Thesis submitted to the

UNIVERSITY OF KERALA

For the award of the Degree of

DOCTOR OF PHILOSOPHY

In

PHYSICS

Under the Faculty of Science

By

PARVATHI S. BABU

*Materials Science and Technology Division
CSIR-National Institute for Interdisciplinary
Science and Technology (NIIST)
Thiruvananthapuram – 695019
University of Kerala
Kerala, India*

December 2019

DECLARATION

I hereby declare that the Ph.D. thesis entitled “**Synthesis and Photoluminescence Properties of Dysprosium Activated Full colour Emission Phosphors**” is an independent work carried out by me at the **Materials Science and Technology Division (MSTD), CSIR - National Institute for Interdisciplinary Science and Technology (CSIR-NIIST), Thiruvananthapuram** under the supervision of **Dr. P. Prabhakar Rao** and it has not been submitted anywhere else for any other degree, diploma or title.

Parvathi S. Babu

Thiruvananthapuram

Date : 27.12.2019

27.12.2019

CERTIFICATE

This is to certify that the work embodied in the thesis entitled “**Synthesis and Photoluminescence Properties of Dysprosium Activated Full colour Emission Phosphors**” has been carried out by Mrs. Parvathi S. Babu under my supervision and guidance at the Material Science and Technology Division of CSIR - National Institute for Interdisciplinary Science and Technology (CSIR-NIIST), Thiruvananthapuram and the same has not been submitted elsewhere for any degree.

(Dr. P. Prabhakar Rao)

Thesis Supervisor

ACKNOWLEDGEMENTS

First and foremost, I owe the ALMIGHTY for the blessings bestowed upon me to be a portion of this wonderful world.

With immense pleasure, I heartily express my deep sense of gratitude to the valuable guidance and advice of my research supervisor, Dr. P. Prabhakar Rao. His keen observations, inspiring guidance as well as support helped me a lot in refining my ideas throughout this journey. It was indeed a great and privilege to work under his guidance and opening up my way to a research life. His constant encouragement and invaluable support from the initial to the final level has enabled me to develop an understanding of the subject.

I extend my gratitude towards Dr. A. Ajayaghosh, present Director, and former Directors Dr. Gangan Prathap and Dr. Suresh Das of CSIR-NIIST, Thiruvananthapuram, for providing me the necessary facilities and infrastructure of the institute for carrying out this work. I express my sincere thanks to Dr. Savithri S., Head, MSTD, Dr. Harikrishna Bhatt, Dr. P. Prabhakar Rao, Dr. M. L. P Reddy and Dr. M.T. Sebastian, Former Heads, MSTD for their support. And I also extend my sincere thanks to Dr. Luxmi Varma, former Head, CSTD and APC at CSIR-NIIST, for her timely help and advice. My sincere thanks also goes to Dr. M. L. P Reddy and Dr. Subratha Das for extending research facilities at various stages of my research work.

I gratefully acknowledge the Kerala State Council for Science Technology and Environment (KSCSTE), Government of Kerala for awarding the research fellowship 2013 and providing the financial support for carrying out this work. I acknowledge the Council of Scientific & Industrial Research (CSIR), New Delhi, India for providing research facilities for the completion of this work.

I also thank Mr. M. R. Chandran, Harish Raj V. R. for the help with the SEM Analysis. I am indebted to Mrs. Lucy Paul, Mr. V. Sreekantan, Shanoj P. S, M. P. Varkey, Haritha for the moral support and help at various stages of work.

I always cherish the support and warm friendship of former colleagues Dr. Sameera S., Dr. Mahesh S. K., Dr. Sumi S., Dr. Vaisakhan Thampi D. S., Mrs. Reshmi V. R., Dr Linda

Francis T., Mrs. Vineetha James, Dr. Divya S., Dr. Sreena T. S., Dr. Athira K. V.Raj, Ms. Renju U. A., Mrs. Suchithra V. G., Mrs. Ajuthara, Dr. Bradha Mahavan, Mrs. Aswathy B.A, Ms. Haritha, Mr. Shanoj P.S., Mrs. Soumya and Mr. N. Pruthiviraj Mr. Nikhil, Mrs. Aswathy R.S.

I wish to thank my present colleagues Mrs Joly A., Dr R. Raveendran, Mrs. K. Susy, Dr. Aranya S., Mr. Sajesh Sasidharan, Mrs. Veenas C. L., Mr. Ramesh Chandran B. R., Mr. Jyothish B., Mrs. Aiswaryamol N. S., Ms. Primsa I. P., Mrs. Simu Rajendran, Mrs. Preethi S., Dr. Reji K. Dhaman, Mr. Sarath Prabhav for their support during the completion of this work.

I would like to acknowledge the valuable contribution of Dr. Ramya A. R., Dr. Usha Gangan T. V., Dr. George T.M., Dr. Bejoy Mohandas, Dr. Sheethu Jose, Thejus P. K. Anaswara Jayaprakash, Shisina, Sreevalsa, Renjith to this thesis. I express my deep love and thankfulness to all inmates of Scholar's Hostel Athira K Jeevan, Dr. Remya P. R., Dr. Swetha S., Sayana C. R., Dr. Shimi M., Dr. Asha P. Tom, Dr. Maya, Aswathy. I also thank my friends Dr. Arya A Das, Shaban, Surjith, Renjith Radhakrishnan, Dhaneesh, Harikrishnan, Hari, Suneeth, Vishnu, Deepak, Amal, Kiran, Vilesh, Vidhya, and Mahesh.

At this moment, I remember with immense gratitude my parents, Late N. Saseendrababu, K. N. Revamma, my sister Lekshmy S. Babu, my cousins Dr. R. S. Rekha, Mr. Mahesh T., Mrs. Bindhu R. S., Mr. Jayapraksh, Mr. Dileep Kumar Mr. Nandhakumar S. Mr. Krishnakumar S. Mrs. Sakthi S. and nephews Govind Mahesh, Harshanandhan J. B., Anandakrishnan J. B. I always remember my Vally, T. K. Sarojini who took care of me and now my daughter, Dhvani Parvathi, from my day 1 on earth. She has always stood for me and it's all because of the love and prayers of the people who are always with me that now I am able to complete this thesis. I would like to record love and affection to my husband, Pinku Krishnan who walked along with me in all my endeavours, my daughter Dhvani Parvathi, who cooperated with me during the final preparations of the thesis, my parents-in-laws J. Krishnan and Omana Amma for treating me as their daughter.

At this point of time I wish to thank all those (if any) who directly or indirectly contributed to my research life and are missed from my list. Thank you.

Parvathi S. Babu

PREFACE

With the ever increasing demand for electricity, it's time to develop new light sources to replace the conventional light sources like incandescent bulbs and fluorescent lamps. Among the many ways of achieving white light, phosphor converted White LEDs (pc-WLEDs) are considered to be the next generation lighting devices due to their high luminous efficiency, low power consumption, good reliability, superior life time and environmental friendliness. There are two methods used to obtain white light emission from blue/near-UV LEDs. The combination of blue chip and yellow phosphors (YAG:Ce³⁺), has already been developed and is commercially available which has poor color rendering index (CRI~ 70–80) due to deficiency in the red region. To overcome this problem, another method is to employ a soft UV chip emitting ~400 nm wavelength with red, green and blue (RGB) phosphors, which also has some disadvantages such as low luminescent efficiency owing to the strong reabsorption of blue light by the red and green phosphors. With respect to these problems, the development of a novel, stable and efficient single-phase white-light emitting phosphor that can be effectively excited in the near UV/blue region is one of the most effective solutions and has attracted much attention for white LED applications. In this regard, Dy³⁺ doped phosphors having luminescence lines in the 470–500 nm region (due to ⁴F_{9/2}–⁶H_{15/2} magnetic dipole transition) and in the 570–600 nm region (due to the ⁴F_{9/2}–⁶H_{13/2} electric dipole transition) have attracted much attention because of their emission bands covering the visible region. Near white light emission in Dy³⁺-activated luminescent materials is obtained by mixing the complimentary colors, yellow and blue. Dy³⁺ ions emits white light in most of the host lattices at a suitable yellow to blue intensity ratio which in turn depends on the site symmetry, host composition, excitation wavelength and doping concentration of Dy³⁺ at the luminescent centers. Rare earth doped molybdates and tungstates with powellite/scheelite structure are considered as good host lattices under near-UV or blue excitation due to its MoO₄ tetrahedron unit and also for the luminescence of Dy³⁺ ions because of their excellent thermal and chemical stability. Recently there has been a growing interest on the optical properties of pyrochlore (general formula A₂B₂O₇) based phosphors because of their very high chemical and physical stability. Rare earth niobates, antimonates and tantalates with a general formula, Ln₃MO₇ have huge compositional and structural diversity and gained much attraction as functional materials in various applications. The main objective of the present research work is to study Dy³⁺

luminescence in various host systems and develop novel single-phase white-light emitting phosphor materials for phosphor converted White Light Emitting Diode (pc-WLED) applications.

The present thesis is organized into six chapters. Introduction chapter details solid state lighting technology and various approaches to white light generation. The chapter also depicts the need for developing new single phase white light emitting phosphors having high chemical stability. Emphasis is given on the electronic and luminescence properties of Dy^{3+} along with a brief literature review of Dy^{3+} luminescence in various host lattices. Main objectives of the current work are highlighted and the motivation and importance of choosing the various host structures is stressed.

Second chapter details the studies on the photoluminescent properties of a single phase white light emitting phosphors, $\text{Ca}(\text{La}/\text{Gd})_{1-x}\text{Nb}(\text{Mo}/\text{W})\text{O}_8 : x\text{Dy}^{3+}$ for pc-white LED applications. The photoluminescence properties indicated that Dy^{3+} doped $\text{Ca}(\text{La}/\text{Gd})_{1-x}\text{Nb}(\text{Mo}/\text{W})\text{O}_8$ phosphors has a strong absorption in near UV region and two sharp emission peaks in the visible region. The variation in the luminescence intensity with various Dy^{3+} concentrations in the $\text{Ca}(\text{La}/\text{Gd})_{1-x}\text{Nb}(\text{Mo}/\text{W})\text{O}_8$ host lattice was also studied to calculate the optimum doping concentration. The yellow/blue ratio and Commission Internationale de l'Éclairage color coordinates could be tuned by adjusting the concentration of Dy^{3+} .

White light emitting stannate pyrochlore based single phase phosphor $\text{CaLa}_{1-x}\text{SnNbO}_7 : x\text{Dy}^{3+}$ for pc-white LED applications are discussed in the third chapter. The phosphors emit white light with CIE color coordinates close to the standard coordinates of white light. These phosphors exhibit strong absorptions in the blue wavelength region which are suitable to use with blue LED chip for the white light generation. The substitution of Sr^{2+} ions to the pyrochlore A site further enhanced the f-f transition intensities. The substitution of $\text{Ln} = \text{La}, \text{Gd}, \text{Lu}, \text{Y}$ on the photoluminescence properties of $\text{CaLn}_{1-x}\text{SnNbO}_7 : x\text{Dy}^{3+}$ is also studied.

Chapter four details the synthesis and characterization of $\text{La}_3\text{Sb}_{1-x}\text{O}_7 : x\text{Dy}^{3+}$. Results demonstrate that phosphor materials could be effectively excited by UV light exhibiting white light emission. The effect of Dy^{3+} doping concentration on the emission characteristics of La_3SbO_7 phosphors was also discussed and the trend in the photoluminescence properties was analysed. The emission colours of all the doped samples are located in the white light region. The variation in the luminescence

properties with the substitution of the pentavalent ions, M = Nb, Ta, Sb in the $\text{La}_3\text{M}_{1-x}\text{O}_7 : x \text{Dy}^{3+}$ is also discussed.

Influence of various lanthanide ion (La, Gd, Y) substitution on the Dy^{3+} photoluminescence properties in $\text{Ca}_2\text{Ln}_3\text{Nb}_3\text{O}_7 : x \text{Dy}^{3+}$ host structures are discussed in the fifth chapter. The partial occupancy of the Ln^{3+} at the A and B site of the pyrochlore structure is studied. These phosphors exhibit the blue yellow emissions of Dy^{3+} ions with equally competing intensities and emit white light.

Conclusions drawn from the studies on the Dy^{3+} photoluminescence properties in these host structures which will help in the design of efficient single phase white light emitting phosphors for pc-WLED applications and future scope of the work are presented in the Chapter six.

CONTENTS

	Page
Declaration	i
Certificate	ii
Acknowledgements	iii
Contents	v
List of tables	ix
List of figures	xi
Abbreviations	xvii
Preface	xix
Chapter 1 Introduction and Literature Review	1 - 24
1.1 Introduction	3
1.2 Approaches of white light generation in light emitting diodes	4
1.2.1 RGB LEDs	4
1.2.2 Phosphor converted LEDs	5
1.3 Basic aspects of phosphor converted white LEDs	7
1.4 Basic Terminology	9
1.4.1 Color temperature and Correlated color temperature (CCT)	9
1.4.2 Commission International de l'Eclairage (CIE)	10
1.4.3 Color rendering index (CRI or Ra)	11
1.4.4 Luminous efficacy	11
1.4.5 Quantum yield	15
1.5 Phosphors for LED-based Solid-State Lighting	12
1.6 Basic requirement of a phosphor to be used in pc-WLEDs	14
1.7 Lanthanides	14
1.8 Luminescence properties of Dy ³⁺	18
1.9 A collection from the past	20
1.10 Objectives of the study	23

Chapter 2 Photoluminescent properties of single phase white light emitting phosphors $\text{Ca}(\text{La}/\text{Gd})_{1-x}\text{Nb}(\text{Mo}/\text{W})\text{O}_8 : x \text{Dy}^{3+}$ 25-56

	Abstract	26
2.1	Introduction	28
2.2	Experimental section	30
	2.2.1 Synthesis	30
	2.2.2 Characterisation Techniques	30
2.3	Results and discussion	31
	2.3.1 Powder X-ray diffraction analysis	31
	2.3.2 Morphological Studies	37
	2.3.3 Optical and Photoluminescence Studies	38
2.4	Conclusions	56

Chapter 3 White light emitting stannate pyrochlore based single phase phosphors $\text{CaLn}_{1-x}\text{SnNbO}_7 : x \text{Dy}^{3+}$ (Ln = La, Gd, Lu, Y) 58-87

	Abstract	59
3.1	Introduction	61
3.2	Experimental section	64
	3.2.1 Synthesis	64
	3.2.2 Characterisation Techniques	64
3.3	Results and discussion	65
	3.3.1 Powder X-ray diffraction analysis	65
	3.3.2 Morphological studies	67
	3.3.3 Optical and photoluminescence studies	68
	3.3.4 The effect of Sr^{2+} ions substitution on the optical properties of $\text{Ca}_{1-y}\text{Sr}_y\text{La}_{0.97}\text{Sn NbO}_7 : 0.03 \text{Dy}^{3+}$ ($y = 0, 0.1, 0.2, 0.3$) samples.	80
3.4	Conclusions	87

Chapter 4 Photoluminescent properties of $\text{La}_{3-x}\text{MO}_7 :x \text{Dy}^{3+}$	
(M = Sb, Ta, Nb) Phosphors	89-104
	Abstract
	90
4.1 Introduction	91
4.2 Experimental Section	93
4.2.1 Synthesis	93
4.2.2 Characterisation techniques	93
4.3 Results and discussion	93
4.3.1 Powder X-ray diffraction analysis	93
4.3.2 Photoluminescence studies	96
4.3.3 The effect of Dy^{3+} ions doping on the optical properties of $\text{La}_{3-x}\text{SbO}_7 :x \text{Dy}^{3+}$ ($x = 0, 0.025, 0.050, 0.075, 0.100$) samples	99
4.4 Conclusions	103
Chapter 5 Photoluminescent properties of single phase white light emitting phosphors $\text{Ca}(\text{La}/\text{Gd})_{1-x}\text{Nb}(\text{Mo}/\text{W})\text{O}_8 : x \text{Dy}^{3+}$	105-116
	Abstract
	107
5.1 Introduction	109
5.2 Experimental section	110
5.2.1 Synthesis	110
5.2.2 Characterisation Techniques	110
5.3 Results and discussion	110
5.3.1 Powder X-ray diffraction analysis	110
5.3.2 Photoluminescence Studies	112
5.4 Conclusions	116

Chapter 6 Conclusions and scope of future work	117-124
Future scope	120
References	121-124
List of Publications	125
List of Conference proceedings	126-127

List of tables

Table 1.1	Efficacy, CCT and CRI of various light sources	12
Table 2.1	Lattice parameters and unit cell volume of $\text{CaLa}_{1-x}\text{NbMoO}_8:x\text{Dy}^{3+}$ ($x = 0.020, 0.025, 0.030, 0.035, 0.050, 0.075$) samples	33
Table 2.2	Lattice parameters and unit cell volume of $\text{CaGd}_{1-x}\text{NbMoO}_8:x\text{Dy}^{3+}$ ($x = 0.020, 0.025, 0.030, 0.035, 0.050, 0.075$) samples	34
Table 2.3	Lattice parameters and unit cell volume of $\text{CaLa}_{1-x}\text{NbWO}_8:x\text{Dy}^{3+}$ ($x = 0.020, 0.025, 0.030, 0.035, 0.050, 0.075$) samples	36
Table 2.4	Lattice parameters and unit cell volume of $\text{CaGd}_{1-x}\text{NbWO}_8:x\text{Dy}^{3+}$ ($x = 0.020, 0.025, 0.030, 0.035, 0.050, 0.075$) samples.	36
Table 2.5	CIE color coordinate values and Y/B ratios of $\text{CaLa}_{1-x}\text{NbMoO}_8:x\text{Dy}^{3+}$ ($x = 0.020, 0.025, 0.030, 0.035, 0.050, 0.075$) samples. under 351 nm excitation.	48
Table 2.6	CIE color coordinate values and Y/B ratios of $\text{CaLa}_{1-x}\text{NbMoO}_8:x\text{Dy}^{3+}$ ($x = 0.020, 0.025, 0.030, 0.035, 0.050, 0.075$) samples. under 366 nm excitation.	48
Table 3.1	Lattice parameters and unit cell volume of Dy^{3+} doped $\text{CaLa}_{1-x}\text{SnNbO}_7$ samples.	66
Table 3.2	Y/B ratio of Dy^{3+} doped $\text{CaLa}_{1-x}\text{SnNbO}_7$ samples under different excitation wavelengths.	78
Table 3.3	CIE values of Dy^{3+} doped $\text{CaLa}_{1-x}\text{SnNbO}_7$ samples under different excitation wavelengths.	79
Table 3.4	Lattice parameters and unit cell volumes of $\text{Ca}_{1-y}\text{Sr}_y\text{La}_{0.97}\text{SnNbO}_7:0.03\text{Dy}^{3+}$ ($y = 0, 0.1, 0.2, 0.3$) samples.	81
Table 3.5	Y/B ratios and CIE values of $\text{Ca}_{1-y}\text{Sr}_y\text{La}_{0.97}\text{SnNbO}_7:0.03\text{Dy}^{3+}$ ($y = 0, 0.1, 0.2, 0.3$) samples under 452 nm excitation wavelengths.	85

List of figures

Figure 1.1	Different approaches of white light generation using LEDs.	5
Figure 1.2	The configurational coordinate diagram.	8
Figure 1.3	The 1931 CIE chromaticity coordinate diagram.	10
Figure 1.4	The energy level diagram of Dy ³⁺ ion.	19
Figure 2.1	Powder X-ray diffraction patterns of CaLa _{1-x} NbMoO ₈ :xDy ³⁺ ($x = 0.020, 0.025, 0.030, 0.035, 0.050, 0.075$).	31
Figure 2.2	Powder X-ray diffraction patterns of CaGd _{1-x} NbMoO ₈ :xDy ³⁺ ($x = 0.020, 0.025, 0.030, 0.035, 0.050, 0.075$).	32
Figure 2.3	Powder X-ray diffraction patterns of CaLa _{1-x} NbWO ₈ :xDy ³⁺ ($x = 0.020, 0.025, 0.030, 0.035, 0.050, 0.075$).	35
Figure 2.4	Powder X-ray diffraction patterns of CaGd _{1-x} NbWO ₈ :xDy ³⁺ ($x = 0.020, 0.025, 0.030, 0.035, 0.050, 0.075$).	35
Figure 2.5	Scanning electron micrographs of CaLa _{1-x} NbMoO ₈ :xDy ³⁺ phosphor powders with varying Dy ³⁺ concentrations: (a) $x = 0.020$, (b) $x = 0.025$, (c) $x = 0.030$, (d) $x = 0.035$, (e) $x = 0.050$, and (f) $x = 0.075$.	37
Figure 2.6	UV-Visible absorption spectra of CaLa _{1-x} NbMoO ₈ : xDy ³⁺ phosphor powders ($x= 0.020, 0.025, 0.030, 0.035, 0.050, 0.075$).	38
Figure 2.7	Excitation spectra of CaLa _{1-x} NbMoO ₈ :xDy ³⁺ ($x = 0.020, 0.025, 0.030, 0.035, 0.050, 0.075$) for an emission at 487 nm.	39
Figure 2.8	Excitation spectra of CaLa _{1-x} NbMoO ₈ :xDy ³⁺ ($x = 0.020, 0.025, 0.030, 0.035, 0.050, 0.075$) for an emission at 575 nm.	39
Figure 2.9	Excitation spectra of CaGd _{1-x} NbMoO ₈ :xDy ³⁺ ($x = 0.020, 0.025, 0.030, 0.035, 0.050, 0.075$) for an emission at 479 nm.	40
Figure 2.10	Excitation spectra of CaGd _{1-x} NbMoO ₈ :xDy ³⁺ ($x = 0.020, 0.025, 0.030, 0.035, 0.050, 0.075$) for an emission at 488 nm.	40
Figure 2.11	Excitation spectra of CaGd _{1-x} NbMoO ₈ :xDy ³⁺ ($x = 0.020, 0.025, 0.030, 0.035, 0.050, 0.075$) for an emission at 576 nm.	41
Figure 2.12	Emission spectra of CaLa _{1-x} NbMoO ₈ :xDy ³⁺ ($x = 0.020, 0.025, 0.030, 0.035, 0.050, 0.075$) under 351 nm excitation.	42
Figure 2.13	Emission spectra of CaLa _{1-x} NbMoO ₈ :xDy ³⁺ ($x = 0.020,$	42

	0.025, 0.030, 0.035, 0.050, 0.075) under 366 nm excitation.	
Figure 2.14	Emission spectra of $\text{CaLa}_{1-x}\text{NbMoO}_8:x\text{Dy}^{3+}$ ($x = 0.020, 0.025, 0.030, 0.035, 0.050, 0.075$) under 386 nm excitation.	43
Figure 2.15	Emission spectra of $\text{CaGd}_{1-x}\text{NbMoO}_8:x\text{Dy}^{3+}$ ($x = 0.020, 0.025, 0.030, 0.035, 0.050, 0.075$) under 352 nm excitation.	43
Figure 2.16.	Emission spectra of $\text{CaGd}_{1-x}\text{NbMoO}_8:x\text{Dy}^{3+}$ ($x = 0.020, 0.025, 0.030, 0.035, 0.050, 0.075$) under 366 nm excitation.	44
Figure 2.17	Emission spectra of $\text{CaGd}_{1-x}\text{NbMoO}_8:x\text{Dy}^{3+}$ ($x = 0.020, 0.025, 0.030, 0.035, 0.050, 0.075$) under 387 nm excitation.	44
Figure 2.18	Emission spectra of $\text{CaGd}_{1-x}\text{NbMoO}_8:x\text{Dy}^{3+}$ ($x = 0.020, 0.025, 0.030, 0.035, 0.050, 0.075$) under 449 nm excitation.	45
Figure 2.19	Emission spectra of $\text{CaGd}_{1-x}\text{NbMoO}_8:x\text{Dy}^{3+}$ ($x = 0.020, 0.025, 0.030, 0.035, 0.050, 0.075$) under 453 nm excitation.	45
Figure 2.20	Variation in the luminescent intensities with Dy^{3+} doping concentrations for the $\text{CaLa}_{1-x}\text{NbMoO}_8:x\text{Dy}^{3+}$ samples.	46
Figure 2.21	Variation in the luminescent intensities with Dy^{3+} doping concentrations for the $\text{CaGd}_{1-x}\text{NbMoO}_8:x\text{Dy}^{3+}$ samples.	47
Figure 2.22	Decay curves of $\text{CaLa}_{1-x}\text{NbMoO}_8: x\text{Dy}^{3+}$ ($x= 0.02, 0.025, 0.03, 0.035, 0.05, 0.075$) under an excitation of 351nm monitoring the emission at 575 nm.	49
Figure 2.23	Excitation spectra of $\text{CaLa}_{1-x}\text{NbWO}_8:x\text{Dy}^{3+}$ ($x = 0.020, 0.025, 0.030, 0.035, 0.050, 0.075$) for an emission at 478 nm.	49
Figure 2.24	Excitation spectra of $\text{CaLa}_{1-x}\text{NbWO}_8:x\text{Dy}^{3+}$ ($x = 0.020, 0.025, 0.030, 0.035, 0.050, 0.07$) for an emission at 487 nm.	50
Figure 2.25	Excitation spectra of $\text{CaLa}_{1-x}\text{NbWO}_8:x\text{Dy}^{3+}$ ($x = 0.020, 0.025, 0.030, 0.035, 0.050, 0.075$) for an emission at 575 nm.	50
Figure 2.26	Excitation spectra of $\text{CaGd}_{1-x}\text{NbWO}_8:x\text{Dy}^{3+}$ ($x = 0.020, 0.025, 0.030, 0.035, 0.050, 0.075$) for an emission at 479 nm.	51
Figure 2.27	Excitation spectra of $\text{CaGd}_{1-x}\text{NbWO}_8:x\text{Dy}^{3+}$ ($x = 0.020, 0.025, 0.030, 0.035, 0.050, 0.07$) for an emission at 488 nm.	51
Figure 2.28	Excitation spectra of $\text{CaGd}_{1-x}\text{NbWO}_8:x\text{Dy}^{3+}$ ($x = 0.020, 0.025, 0.030, 0.035, 0.050, 0.075$) for an emission at 575 nm.	52

Figure 2.29	Emission spectra of $\text{CaLa}_{1-x}\text{NbWO}_8:x\text{Dy}^{3+}$ ($x = 0.020, 0.025, 0.030, 0.035, 0.050, 0.075$) under 351 nm excitation.	53
Figure 2.30	Emission spectra of $\text{CaLa}_{1-x}\text{NbWO}_8:x\text{Dy}^{3+}$ ($x = 0.020, 0.025, 0.030, 0.035, 0.050, 0.075$) under 366 nm excitation.	53
Figure 2.31	Emission spectra of $\text{CaLa}_{1-x}\text{NbWO}_8:x\text{Dy}^{3+}$ ($x = 0.020, 0.025, 0.030, 0.035, 0.050, 0.075$) under 387 nm excitation.	65
Figure 2.32	Emission spectra of $\text{CaGd}_{1-x}\text{NbWO}_8:x\text{Dy}^{3+}$ ($x = 0.020, 0.025, 0.030, 0.035, 0.050, 0.075$) under 352 nm excitation.	66
Figure 2.33	Emission spectra of $\text{CaGd}_{1-x}\text{NbWO}_8:x\text{Dy}^{3+}$ ($x = 0.020, 0.025, 0.030, 0.035, 0.050, 0.075$) under 366 nm excitation.	67
Figure 2.34	Emission spectra of $\text{CaGd}_{1-x}\text{NbWO}_8:x\text{Dy}^{3+}$ ($x = 0.020, 0.025, 0.030, 0.035, 0.050, 0.075$) under 387 nm excitation.	68
Figure 3.1	Powder X-ray diffraction patterns of $\text{CaLn}_{0.97}\text{SnNbO}_7: 0.03 \text{Dy}^{3+}$ (Ln = La, Gd, Lu, Y) phosphor samples.	65
Figure 3.2	Powder X-ray diffraction patterns of $\text{CaLa}_{1-x}\text{SnNbO}_7: x\text{Dy}^{3+}$ ($x = 0.01, 0.02, 0.03, 0.04$) samples.	66
Figure 3.3	SEM micrographs of $\text{CaLa}_{1-x}\text{SnNbO}_7:x\text{Dy}^{3+}$ phosphor samples with different Dy^{3+} concentrations: (a) $x = 0.01$, (b) $x = 0.02$, (c) $x = 0.03$, (d) $x = 0.04$.	67
Figure 3.4	UV-Visible absorption spectra of $\text{CaLa}_{1-x}\text{SnNbO}_7: x\text{Dy}^{3+}$ ($x = 0.01, 0.02, 0.03, 0.04$) phosphor powders.	68
Figure 3.5	Excitation spectra of $\text{CaLn}_{0.97}\text{SnNbO}_7: 0.03 \text{Dy}^{3+}$ (Ln = La, Gd, Lu, Y) for an emission at 477 nm.	69
Figure 3.6	Excitation spectra of $\text{CaLn}_{0.97}\text{SnNbO}_7: 0.03 \text{Dy}^{3+}$ (Ln = La, Gd, Lu, Y) for an emission at 487 nm.	69
Figure 3.7	Excitation spectra of $\text{CaLn}_{0.97}\text{SnNbO}_7: 0.03 \text{Dy}^{3+}$ (Ln = La, Gd, Lu, Y) for an emission at 589 nm.	70
Figure 3.8	Excitation spectra of $\text{CaLa}_{1-x}\text{SnNbO}_7:x\text{Dy}^{3+}$ ($x = 0.01, 0.02, 0.03, 0.04$) for an emission at 477 nm.	70
Figure 3.9	Excitation spectra of $\text{CaLa}_{1-x}\text{SnNbO}_7:x\text{Dy}^{3+}$ ($x = 0.01, 0.02, 0.03, 0.04$) for an emission at 487 nm.	71
Figure 3.10	Excitation spectra of $\text{CaLa}_{1-x}\text{SnNbO}_7:x\text{Dy}^{3+}$ ($x = 0.01, 0.02, 0.03, 0.04$) for an emission at 589 nm.	71

Figure 3.11	Emission spectra of $\text{CaLn}_{0.97}\text{SnNbO}_7: 0.03 \text{ Dy}^{3+}$ (Ln = La, Gd, Lu, Y) under 338 nm excitation.	72
Figure 3.12	Emission spectra of $\text{CaLn}_{0.97}\text{SnNbO}_7: 0.03 \text{ Dy}^{3+}$ (Ln = La, Gd, Lu, Y) under 388 nm excitation.	73
Figure 3.13	Emission spectra of $\text{CaLn}_{0.97}\text{SnNbO}_7: 0.03 \text{ Dy}^{3+}$ (Ln = La, Gd, Lu, Y) under 452 nm excitation.	74
Figure 3.14	Emission spectra of $\text{CaLa}_{1-x}\text{SnNbO}_7:x\text{Dy}^{3+}$ ($x = 0.01, 0.02, 0.03, 0.04$) under 338 nm excitation.	74
Figure 3.15	Emission spectra of $\text{CaLa}_{1-x}\text{SnNbO}_7:x\text{Dy}^{3+}$ ($x = 0.01, 0.02, 0.03, 0.04$) under 388 nm excitation.	75
Figure 3.16	Emission spectra of $\text{CaLa}_{1-x}\text{SnNbO}_7:x\text{Dy}^{3+}$ ($x = 0.01, 0.02, 0.03, 0.04$) under 452 nm excitation.	75
Figure 3.17	Variation in the luminescent intensities with Dy^{3+} doping concentrations of $\text{CaLa}_{1-x}\text{SnNbO}_7:x\text{Dy}^{3+}$ ($x = 0.01, 0.02, 0.03, 0.04$) under 452 nm excitation for the emissions at 477nm (black line), 487 nm (red line) and 589 nm (blue line).	76
Figure 3.18	Emission spectra of $\text{CaLa}_{0.97}\text{SnNbO}_7:0.03\text{Dy}^{3+}$ under different excitation wavelengths. ($\lambda_{\text{ex}} = 338 \text{ nm}, 353 \text{ nm}, 388 \text{ nm}$ and 452 nm)	78
Figure 3.19	Decay curves of $\text{CaLa}_{1-x}\text{SnNbO}_7: x\text{Dy}^{3+}$ ($x = 0.01, 0.02, 0.03, 0.04$) under an excitation of 452 nm monitoring the emission at 589 nm.	80
Figure 3.20	Powder X-ray diffraction patterns of $\text{Ca}_{1-y}\text{Sr}_y\text{La}_{0.97}\text{SnNbO}_7: 0.03 \text{ Dy}^{3+}$ ($y = 0, 0.1, 0.2, 0.3$) samples.	81
Figure 3.21	Scanning electron micrographs of $\text{Ca}_{1-y}\text{Sr}_y\text{La}_{0.97}\text{SnNbO}_7: 0.03 \text{ Dy}^{3+}$ phosphor powders with varying Sr^{2+} concentrations: (a) $y = 0.1$, (b) $y = 0.2$, (c) $y = 0.3$.	82
Figure 3.22	UV-Visible absorption spectra of $\text{Ca}_{1-y}\text{Sr}_y\text{La}_{0.97}\text{SnNbO}_7: 0.03 \text{ Dy}^{3+}$ ($y = 0, 0.1, 0.2, 0.3$) phosphor powders.	83
Figure 3.23	Excitation spectra of $\text{Ca}_{1-y}\text{Sr}_y\text{La}_{0.97}\text{SnNbO}_7: 0.03 \text{ Dy}^{3+}$ ($y = 0, 0.1, 0.2, 0.3$) for an emission at 589 nm.	24
Figure 3.24	Emission spectra of $\text{Ca}_{1-y}\text{Sr}_y\text{La}_{0.97}\text{SnNbO}_7: 0.03 \text{ Dy}^{3+}$ ($y = 0,$	84

	0.1, 0.2, 0.3) samples under 452 nm excitation.	
Figure 3.25	Variation in the luminescent intensities of $\text{Ca}_{1-y}\text{Sr}_y\text{La}_{0.97}\text{SnNbO}_7 : 0.03 \text{ Dy}^{3+}$ ($y = 0, 0.1, 0.2, 0.3$) samples under 452 nm excitation for the emissions at 477nm (black line) and 589 nm (red line).	85
Figure 3.26	Decay curves of $\text{Ca}_{1-y}\text{Sr}_y\text{La}_{0.97}\text{SnNbO}_7 : 0.03 \text{ Dy}^{3+}$ ($y = 0, 0.1, 0.2, 0.3$) samples under an excitation of 452 nm monitoring the emission at 589 nm.	86
Figure 4.1	Powder X-ray diffraction patterns of $\text{La}_{2.95}\text{SbO}_7 : 0.050 \text{ Dy}^{3+}$.	94
Figure 4.2	Powder X-ray diffraction patterns of $\text{La}_{2.95}\text{TaO}_7 : 0.050 \text{ Dy}^{3+}$.	94
Figure 4.3	Powder X-ray diffraction patterns of $\text{La}_{2.95}\text{NbO}_7 : 0.050 \text{ Dy}^{3+}$	95
Figure 4.4	Excitation spectra of $\text{La}_{2.95}\text{MO}_7 : 0.050 \text{ Dy}^{3+}$ ($M = \text{Sb, Ta, Nb}$) for an emission at 479 nm.	96
Figure 4.5	Excitation spectra of $\text{La}_{2.95}\text{MO}_7 : 0.050 \text{ Dy}^{3+}$ ($M = \text{Sb, Ta, Nb}$) for an emission at 489 nm.	97
Figure 4.6	Emission spectra of $\text{La}_{2.95}\text{MO}_7 : 0.050 \text{ Dy}^{3+}$ ($M = \text{Sb, Ta, Nb}$) under 344 nm excitation.	98
Figure 4.7	Emission spectra of $\text{La}_{2.95}\text{MO}_7 : 0.050 \text{ Dy}^{3+}$ ($M = \text{Sb, Ta, Nb}$) under 358 nm excitation.	98
Figure 4.8	Emission spectra of $\text{La}_{2.95}\text{MO}_7 : 0.050 \text{ Dy}^{3+}$ ($M = \text{Sb, Ta, Nb}$) under 377 nm excitation.	99
Figure 4.9	Powder X-ray diffraction patterns of $\text{La}_{3-x}\text{SbO}_7 : x \text{ Dy}^{3+}$ ($x = 0, 0.025, 0.050, 0.075, 0.100$) samples.	100
Figure 4.10	Enlarged view of the (202) and (220) diffraction peaks of $\text{La}_{3-x}\text{SbO}_7 : x \text{ Dy}^{3+}$ ($x = 0, 0.025, 0.050, 0.075, 0.100$) showing the shift of the diffraction peaks towards the higher 2θ angle side with increasing concentration of Dy^{3+} ions.	100
Figure 4.11	Excitation spectra of $\text{La}_{3-x}\text{SbO}_7 : x \text{ Dy}^{3+}$ ($x = 0.025, 0.050, 0.075, 0.100$) for an emission at 479 nm.	101
Figure 4.12	Excitation spectra of $\text{La}_{3-x}\text{SbO}_7 : x \text{ Dy}^{3+}$ ($x = 0.025, 0.050, 0.075, 0.100$) for an emission at 489 nm.	101
Figure 4.13	Emission spectra of $\text{La}_{3-x}\text{SbO}_7 : x \text{ Dy}^{3+}$ ($x = 0.025, 0.050, 0.075, 0.100$) under 344 nm excitation.	102
Figure 4.14	Emission spectra of $\text{La}_{3-x}\text{SbO}_7 : x \text{ Dy}^{3+}$ ($x = 0.025, 0.050,$	102

	0.075, 0.100) under 358 nm excitation.	
Figure 4.15	Emission spectra of $\text{La}_{3-x}\text{SbO}_7: x \text{Dy}^{3+}$ ($x = 0.025, 0.050, 0.075, 0.100$) under 377 nm excitation	103
Figure 5.1	Powder X-ray diffraction patterns of $\text{Ca}_2\text{La}_{2.95}\text{Nb}_3\text{O}_7 : 0.05 \text{Dy}^{3+}$.	111
Figure 5.2	Powder X-ray diffraction patterns of $\text{Ca}_2\text{Gd}_{2.95}\text{Nb}_3\text{O}_7 : 0.05 \text{Dy}^{3+}$.	111
Figure 5.3	Powder X-ray diffraction patterns of $\text{Ca}_2\text{Y}_{2.95}\text{Nb}_3\text{O}_7 : 0.05 \text{Dy}^{3+}$.	112
Figure 5.4	Excitation spectra of $\text{Ca}_2\text{Ln}_{2.95}\text{Nb}_3\text{O}_7 : 0.05 \text{Dy}^{3+}$ (Ln = La, Gd, Y) for an emission at 479 nm.	113
Figure 5.5	Excitation spectra of $\text{Ca}_2\text{Ln}_{2.95}\text{Nb}_3\text{O}_7 : 0.05 \text{Dy}^{3+}$ (Ln = La, Gd, Y) for an emission at 489 nm.	113
Figure 5.6	Excitation spectra of $\text{Ca}_2\text{Ln}_{2.95}\text{Nb}_3\text{O}_7 : 0.05 \text{Dy}^{3+}$ (Ln = La, Gd, Y) for an emission at 579 nm.	114
Figure 5.7	Emission spectra of $\text{Ca}_2\text{Ln}_{2.95}\text{Nb}_3\text{O}_7 : 0.05 \text{Dy}^{3+}$ (Ln = La, Gd, Y) under 350 nm excitation.	115
Figure 5.8	Emission spectra of $\text{Ca}_2\text{Ln}_{2.95}\text{Nb}_3\text{O}_7 : 0.05 \text{Dy}^{3+}$ (Ln = La, Gd, Y) under 388 nm excitation.	115
Figure 5.9	Emission spectra of $\text{Ca}_2\text{Ln}_{2.95}\text{Nb}_3\text{O}_7 : 0.05 \text{Dy}^{3+}$ (Ln = La, Gd, Y) under 453 nm excitation.	116

Abbreviations

CCT	Correlated Color Temperature
CIE	Commission Internationale de l'Éclairage
CN	Co-ordination Number
CRI	Color Rendering Index
CT	Charge Transfer
CTB	Charge Transfer Band
CTS	Charge Transfer States
ED	Electric Dipole
EM	Emission
EX	Excitation
ET	Energy Transfer
ICDD	International Centre for Diffraction Data
InGaN	Indium Gallium Nitride
LMCT	Ligand to Metal Charge Transfer
LED	Light Emitting Diode
Ln	Lanthanide
MD	Magnetic Dipole
NTSC	National Television Standards Committee
NUV	Near Ultraviolet
OLED	Organic Light Emitting Diode
pc- WLED	Phosphor Converted White Light Emitting Diode
PL	Photoluminescence
RGB	Red Green and Blue
RE	Rare Earth
SEM	Scanning Electron Microscopy

SSL	Solid State Lighting
SSR	Solid State Reaction
UV	Ultraviolet
WLED	White Light Emitting Diode
YAG	Yttrium Aluminium Garnet
XRD	X-Ray Diffraction

Chapter 1

Introduction and Literature Review

1.1. Introduction

The subject of phosphors and luminescence has taken a new drive in exploring the technological development and understanding the different facets of everyday life. A large number of optoelectronic devices and displays have emerged in the lighting industry which relies greatly on the phosphor technology. Some of the discoveries being a pure conjecture in early 1990's has become a reality today. Phosphor converted White Light Emitting Diodes (pc-WLEDs) being the new light sources promise to displace and make obsolete the traditional light sources like incandescent lamps, fluorescent lamps and ubiquitous color Cathode Ray Tubes (CRT) which were earlier used in TV and computer monitors.

Phosphor converted white light emitting diodes (pc-WLEDs) are emerging as an ultimate light source in the lighting technology and provide an opportunity to reduce the energy usage. With the great demand for the fossil fuels and the environmental issues on their usage are continuously exerting pressure on the world energy infrastructure. High luminescence efficiency, long life time, low power consumption, better color stability, free of mercury, durability and environment friendly, are some of the key factors for the rapid development of the solid-state lighting based on high brightness white LEDs. Incandescent, fluorescent and high-intensity discharge lamps are the major traditional lighting sources, preferred for residential applications, commercial buildings and street and stadium lighting respectively. In an incandescent bulb, less than 5% of the power consumed is converted into light and the remaining is lost as heat. The efficiency of the conventional light sources, such as filament bulbs and fluorescent lamps is limited by the fundamental factors, involving large energy losses due to high stokes shift and heating losses. On the other hand, LEDs made of semiconductor materials have the potential of converting electricity to light with near unit efficiency. The development of blue light emitting diode was long awaited technology, because a white LED can be realized by use of blue LED with conventional red and green LED and phosphors.

The first light emitting diode dates back to 1907, when H. J. Round reported on light emission from a silicon carbide junction diode. On similar lines, Losev in 1927 observed an interesting emission from ZnO and SiC diodes. During that time, these developments largely remained unnoticed and LEDs were used exclusively for displays and in the indicator lamps. The first practical visible spectrum LED was developed, by

Nick Holonyak at General Electric in 1962. It was Shuji Nakamura's invention, that completely changed the fate of LEDs and took off LEDs to the general illumination purpose. They successfully fabricated a double hetero structure InGaN/GaN blue LED chips for the first time in 1993. In 1994 they were successful in producing high power blue InGaN/AlGaN LEDs.

1.2 Approaches of white light generation in light emitting diodes

1.2.1 RGB LEDs

In the traditional phosphor industry, there are basically three primary methods for producing white light from tricolor phosphors i.e. blue green and red and LEDs. At present, several phosphors are available for excitation at 250 nm (the dominant emission band of mercury lamps). In solid state lighting, however, the excitation wavelength is much longer, typically in the range 380 to 480 nm. The first one is the multiple LED approach, formed by combination of emissions from three or more monochromatic LEDs emitting light at different wavelengths via the blue, green and red and fabrication into a single device so that the blended light appears white. Even though this method is the simplest, LED package, device fabrication and colour mixing optics is the most expensive. In this method, there is no quantum deficit arising from Stokes shift and has excellent color coordinates and white point control. Since the light emission is from the individual LEDs, this method needs independent output power control on each LED and also there is a gap in the operating voltage between them making the operation quite cumbersome. With the variation in the drive current, there is instability of the colour temperature due to the degradation of colours from different LEDs. However, it is difficult to control the color quality and lifetime of the three independent LEDs (red, green, and blue) and therefore most white LEDs rely on the conversion of LED light via inorganic phosphors (luminescent materials). As such, advanced phosphors, with improved quantum yields and enhanced thermal stability, are required to develop the next generation of highly efficient, solid-state white lights.

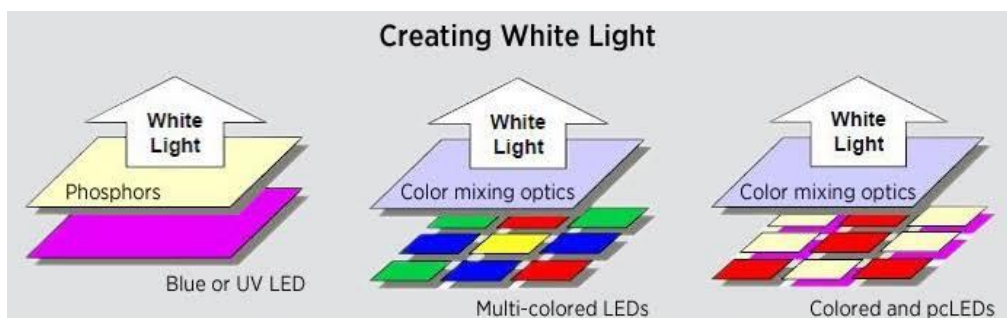


Figure 1.1 Different approaches of white light generation using LEDs.

1.2.2 Phosphor converted LEDs

Solid State lighting is a rapidly evolving and emerging technology and uses light emitting diodes (LEDs), organic light emitting diodes (OLED), or polymer light emitting diodes (PLED) as sources of illumination rather than electrical filaments, plasma, or gas. Phosphor converted White Light Emitting Diodes (pc-WLEDs) are an important class of SSL devices and has a greater efficiency of converting electricity to visible light that is likely to approach 50% within a few years. A second method uses a blue LED to excite a yellow-emitting phosphor. The combined blue and yellow light appears white. The third technique uses a near-UV or UV LED and multiple phosphors that emit light across the entire visible spectrum. White light is obtained by the complete absorption of UV light by the single phosphor or mixed RGB phosphors. Though it has excellent color rendering and gives good white, there is no control on the uniform coating of phosphors. The quantum deficit between the UV pump and the phosphors especially the low energy red phosphor, dissipates significant energy thus making this approach inherently less efficient than the RGB LED scheme for generating white light.

Ce³⁺-doped garnets.

The yellow phosphor, $\text{Y}_3\text{Al}_5\text{O}_{12}:\text{Ce}^{3+}$ (YAG:Ce), dating back to 1967, with compositional modifications, were primarily used in CRTs prior to use in pc-WLEDs. In pc-WLEDs, YAG: Ce^{3+} absorbs blue light from an InGaN chip through the allowed $4f^1 \rightarrow 5d^1$ transition and emits yellow light via the reverse $5d^1 \rightarrow 4f^1$ transition. The yellow emission due to the transition from the lowest excited $5d^1$ level to the spin-orbit split $4f^1$ ground states, giving rise to an extremely broad emission band with a FWHM > 100 nm. The complimentary combination of the yellow emission from YAG: Ce^{3+} and the blue radiation that “bleeds” through a YAG: Ce^{3+} coating is an approach to realize white light

emission with a daylight-like color temperature (CCT > 4000 K) and reasonable color rendering (CRI ~70- 80). The generation of white light by this approach enables pc-WLEDs to be used in many applications where color quality is not a key requirement, including backlights for portable displays and indicators. Since the white light generation based on InGaN Chip YAG: Ce³⁺ combination dominates the total pc-WLED market, current phosphor usage is heavily skewed toward YAG: Ce³⁺. Therefore, this method sets up as a benchmark for other LED phosphors. In YAG: Ce³⁺, the absorption and emission transitions are parity and spin allowed, giving strong absorption of blue LEDs and a fast decay time that prevents saturation quenching as observed in the earlier phosphors developed for lighting. The traditional CFL/LFL/CRT phosphors uses YAG: Ce³⁺ which is synthesized using high-purity precursors (Y₂O₃, Al₂O₃, CeO₂). The quantum efficiency (QE) of YAG: Ce³⁺ under blue LED excitation is >85%, even at 200⁰C, and YAG: Ce³⁺ doesn't degrade under blue LED excitation or moisture.

The main drawback of producing white light by YAG: Ce³⁺ is that they are limited to high CCTs and lower CRIs, due to a lack of a sufficient red spectral component. This limitation can be overcome to an extent by red shifting the Ce³⁺ 5d¹ → 4f¹ emission by Gd³⁺ substitution for Y³⁺, or Mg²⁺- Si⁴⁺ substitution for Al³⁺(octahedral)-Al³⁺(tetrahedral). Though the CCTs and CRIs are improved, this redshift decreases the efficiency, especially at high temperatures. The limitations for red component of the Ce³⁺-doped aluminate garnets further prompted the search for alternate garnet compositions. One alternative to the aluminium garnets is the silicate garnets phosphors with Ce³⁺ emission maxima ranging from 505-605 nm

Considering the potential advantages and the technical challenges of the various approaches to white light generation, the development of new, highly efficient single phase white emitting phosphors that can be efficiently excited at near UV or blue wavelengths is a challenging area to improve the efficiency of WLEDs. White light emission resulting from a single-phase phosphor is expected to obtain high luminous efficacy in comparison with that from two or three phosphors, because it could avoid multi-phosphors re-absorption of emission colors. White light emission from a single phase is economical and the device fabrication is easier, however this method suffers from lower CRI, lower luminous efficacy, lower chromatic stability under different currents. Therefore, single phase white-emitting phosphors are suited for UV-pumped WLEDs to improve the luminescence reproducibility and efficiency. Researchers across the

globe are designing new rules to synthesize new materials, for the development of complex inorganic phosphors. Most of the new luminescent materials which are basically inorganic phosphors are discovered either by chemical substitutions within known compounds or with high-throughput combinatorial searches. All these aforementioned approaches are specifically targeted for the discovery of novel phosphors that have an excellent probability of photoluminescence.

1.3 Basic aspects of phosphor converted white LEDs

Luminescence is a process in which matter emits non-thermal radiation, characteristic of the particular luminescent material. Luminescence varies from incandescence, in which the solids radiate light because of their high temperature. Luminescence arises because of the excitation of the atoms of the solids by some means without heating the substance. In luminescence, the electronic state of a substance is excited by some external energy, and the excitation energy is given off as light. The radiation emitted by a luminescent material is usually in the visible range, but can also be in other spectral regions such as UV and Infrared (IR). Various types of luminescence are there like photoluminescence, mechanoluminescence, electroluminescence and bioluminescence.

In photoluminescence (PL), a chemical compound absorbs photons or electromagnetic radiation and is excited to a higher energy state and then radiates photons back out, returning to a lower energy state. The configurational coordinate diagram as depicted in Figure 1.2 is usually used to describe the PL mechanism of an activator (Blasse and Grabmaier 1994). As shown in Figure 1.2, the total energy of the activator is plotted as a function of the distance between metal cations and anions in the lattice. The horizontal lines in the ground state and excited state curves denote the vibrational states. When the activator absorbs some radiation, it is raised to the excited state. The excitation and emission processes are illustrated by vertical arrows, showing that the nucleus of the activator stays at approximately the same position during these processes. It is the so-called Franck-Condon principle, based on the fact that an atomic nucleus is heavier than an electron and an electron moves much faster than a nucleus (Blasse and Grabmaier 1994). The energy difference between excitation and emission is known as the Stokes shift. The term photoluminescence takes into account of two phenomena such as

fluorescence and phosphorescence. Fluorescence corresponds to the emission process involving a spin allowed (singlet \rightarrow singlet) transition and is characterized by a short lifetime of about $< 10^{-8}$ s. On the other hand, phosphorescence corresponds to emission process involving a spin forbidden (triplet \rightarrow singlet) transition and is characterized by a long lifetime of about $> 10^{-8}$ s. Since inorganic phosphors for WLED applications are excited by the radiative emission of LED chips, the luminescence of the phosphors is expressed as photoluminescence.

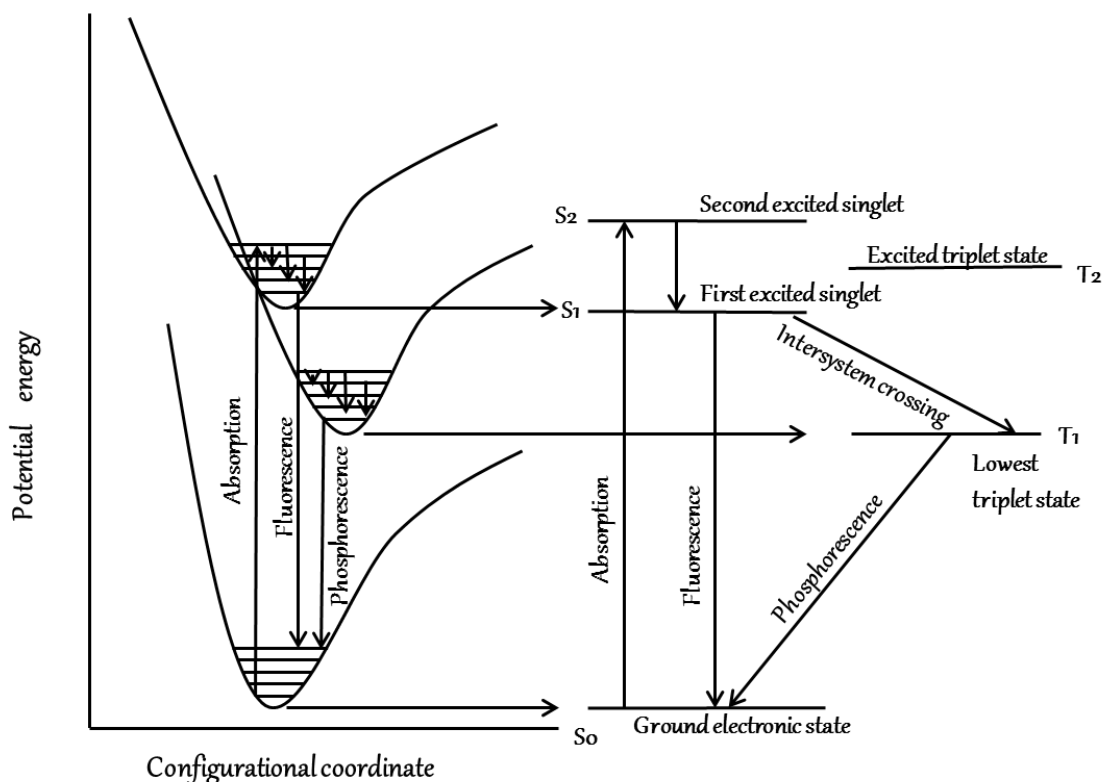


Figure 1.2 : The configurational coordinate diagram.

Phosphors consist of a host and an activator (also called luminescent center). According to the electronic transitions, the principal localized luminescent centers can be categorized as follows (below, an arrow to the right indicates optical absorption and to the left, emission) (Blasse and Grabmaier 1994, Ronda 2007).

- (i) $1s \leftrightarrow 2p$; e.g., F center
- (ii) $ns^2 \leftrightarrow ns np$; e.g., Ga^+ , Sn^{2+} , As^{3+} , Bi^{3+} , Cu^- , Ag^- , Au^-
- (iii) $nd^{10} \leftrightarrow nd^9(n+1)s$; e.g., Cu^+ , Ag^+ , Au^+
- (iv) $3d^n \leftrightarrow 3d^n$, $4d^n \leftrightarrow 4d^n$; e.g., first and second transition metal ions.
- (v) $4f^n \leftrightarrow 4f^n$, $5f^n \leftrightarrow 5f^n$; e.g., rare earth and actinide ions.

- (vi) $4f^n \leftrightarrow 4f^{n-1}5d$; e.g., Ce^{3+} , Sm^{2+} , Eu^{2+} , Tm^{2+} , Yb^{2+}
- (vii) A charge transfer transition (transition between an anion p electron and an empty cation orbital) e.g.: intramolecular transitions in complexes

Rare earth (RE) and transition metal (TM) ions are the cations most frequently used in phosphors. The line-shaped transitions are due to the $4f-4f$ transitions of RE ions and the broad bandshaped transitions are due to the $4f-5d$ transitions of RE ions and the $d-d$ transitions of TM ions are and coordination environment greatly affects these transitions (Blasse 1979).

1.4 Basic Terminology

Phosphor -converted white light emitting diodes (pc-WLEDs) as an excellent solid state light source for the next generation light industry have unique advantages like environment friendliness, energy savings, small volume and long persistence. The major challenges in pc-WLEDs is to achieve high chromatic stability, high luminous efficacy, price competitiveness, brilliant color rendering properties which are critically based on the phosphor properties. There a better understanding of these quantities is necessary to realize a good light source that finds applicability in various fields of general illumination.

1.4.1 Color temperature and Correlated color temperature (CCT)

Color temperature (Kelvin) is the absolute temperature at which a blackbody radiator must be functional that have the same chromaticity as that of the light source. [Kaufman *et al.* 1972, Khan M. N. 2014]. The light from an incandescent bulb is due to thermal radiation produced by the heating of the filament so that the bulb can be assumed to be very close to an ideal black body-radiator, the temperature of the filament is its color temperature. Various other light sources including fluorescent lamps emits light by means other than thermal radiations. Correlated color temperature (CCT) are color temperature values of light sources other than incandescent bulbs and is defined as the temperature of a black body whose chromaticity most nearly resembles that of a light. Lower CCT contributes to a warmer (more yellow-red) light, and a higher value of color temperature contributes to a colder (more blue) light. The natural daylight has a rather low CCT near dawn compared to a higher one during the day time. Considering the needs

of lighting one can choose between a warm light or cold light and to install a comfortable electrical lighting system.

1.4.2 Commission International de l'Eclairage (CIE)

The Commission Internationale de l'Eclairage in 1931 introduced CIE color coordinate diagram, as shown in Figure 1.3, by the representations of all of the chromaticities visible to the average person on a scale of x and y . [Stevens W. R 1969] Red, blue, green are the primary colors and any color can be produced by a suitable combinations of the three primaries. The Commission International de l'Eclairage (CIE) is the most widely used method to describe the composition of any color. Tristimulus values denoted by X , Y , Z , can be used to represent any color. The x , y , z , also called chromaticity coordinates are the ratios of X , Y , Z of the light to the sum of the three tristimulus values, $X+Y+Z$. (x, y) is usually used to represent the color. It is always essential only to quote the quantity of two of the reference stimuli to define a color since the three quantities (x, y, z) are made always to sum to 1. National Television Standards Committee (NTSC) standard colour coordinates of white are $(0.33, 0.33)$.

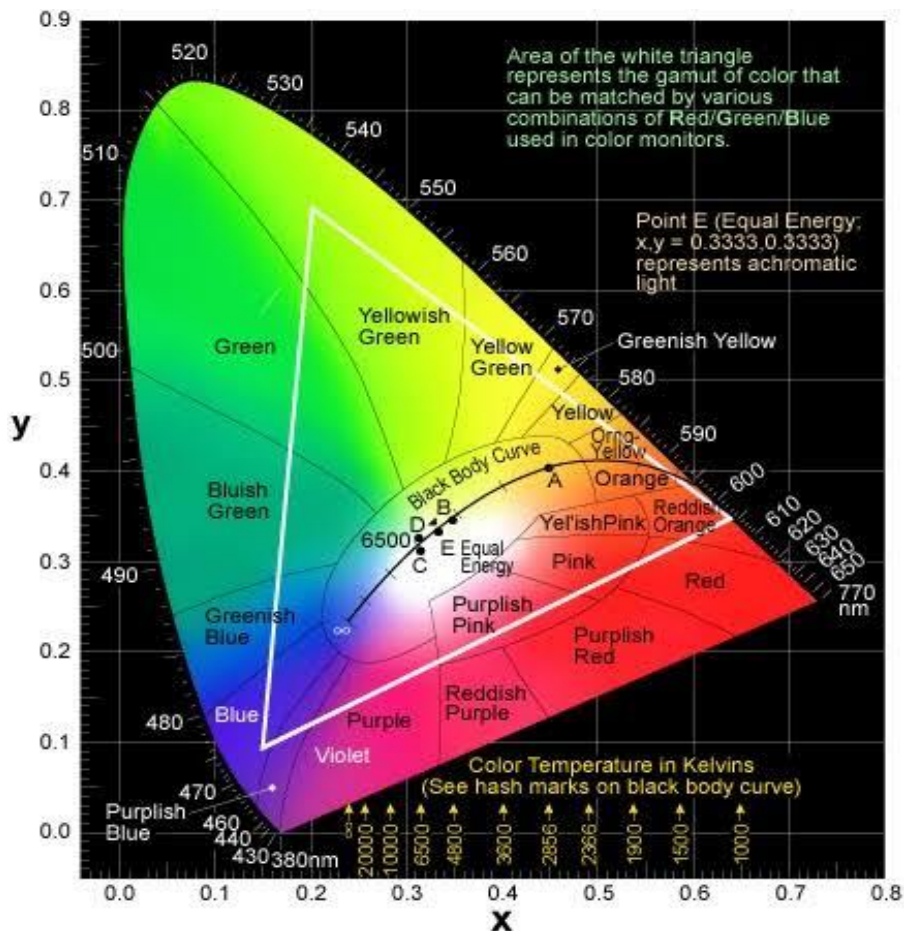


Figure 1.3 1931 CIE chromaticity coordinate diagram.

1.4.3 Color rendering index (CRI or Ra)

The color rendering index (CRI or Ra) is a unitless index rated on a scale from 0 to 100 and is a figure of merit of a light source to quantitatively reproduce the colors of various objects in comparison to sunlight. The sun and the incandescent bulb is defined as having a CRI of 100. The higher the CRI, the more accurately the colours are rendered. CRI was introduced on the fact that the same object look differently under different lighting spectral distributions. When an object is illuminated by a light source and also by a reference illuminate having the same correlated color temperature , CRI is calculated as the difference in the chromaticities of eight CIE standard color samples (CIE 1995) [Kaufman *et al.* 1972] The smaller the average differences in chromaticities, the higher the CRI.

1.4.4 Luminous efficacy

Luminous efficacy is a figure of merit for light source and gives a measure of the amount of energy converted into light of the source and how well the emitted light is perceived by the human eye. It is defined as the ratio of the total luminous flux emitted (lumens) to the input power (watts or equivalent). A higher CRI value demands a proper spectral dispersion covering all the visible range, and this leads to a luminous efficacy far below the theoretically attainable maximum value of a light source which is 683 lm/W Therefore, the luminous efficacy always contradicts with CRI.

1.4.5 Quantum yield

Quantum yield or the absolute quantum yield is the the ratio between the number of photons emitted and the number of photons absorbed and is an intrinsic property of the luminescence conversion process.

Efficacy, CCT and CRI of various light sources of some off the typical light sources are given in the table 1.1.

Table 1.1 Efficacy, CCT and CRI of various light sources

Light source	Efficacy lm/W	CCT K	CRI
Incandescent	15	2760	100
Linear Fluorescence	108	4100	85
Compact Fluorescence	63	2700	82
Halogen	22	3000	100
Metal halide	80-110	4000	70
Philips white LED A 19 lamp	69	2700	80

1.5 Phosphors for LED-based Solid-State Lighting

With the emerging energy crisis, it has become the need of the day to explore new sources of lighting to meet the requirements of modern man. Over the past decade, the efficacy of solid-state lighting (SSL) based upon InGaN LEDs has improved tremendously by a factor $>10x$: the efficacy of cool white LEDs surpasses the traditional and conventional linear fluorescent lamp (LFLs) efficacies (>100 lm/W) and warm white 1W LEDs surpasses compact fluorescent lamps (CFLs) efficacies ($>60-70$ lm/W). Artificial lighting is now driven to a new dimension in transforming the status of white light generation and that would finally lead to SSL market penetration in many lighting product segments. The United States Department of Energy has set a 2015 efficacy target for warm white packages as 138 lm/W and this significant technical achievement has been marked over the years. In Light Emitting Diodes based on SSL, InGaN semiconductors forms the basis for violet, blue, and green LEDs, while AlInGaP semiconductors can be used for the red and amber LEDs. Both of these semiconductor systems InGaN and AlInGaP tend to have much lower efficiencies in the visible region of the spectrum via green, yellow, and amber spectral regions. The limitations in generating white light for general lighting making use of InGaN and AlInGaP and its efficiency makes it necessary to employ phosphor down conversion materials (in spite of the

inherent Stokes losses) to generate full color emission for high efficacy LED packages, lamps, and fixtures. The maximum efficiency of blue and violet InGaN LEDs appears to be higher than the maximum efficiency for red ($\lambda_{\max} = 600\text{-}630\text{ nm}$) AlInGaP LEDs. The potential efficacy for a system, which focuses on the principle of phosphor down conversion of InGaN LEDs also termed as pcLEDs, spanning the entire white spectrum could be greater than systems using AlInGaP LEDs to generate red light, further motivating the development of LED phosphors across the visible spectrum.

In recent years, there has been extensive research in the development for phosphors that can be used in LFLs/CFLs, cathode-ray tubes (CRTs), and X-ray films, but most of these traditional phosphors are not suitable for pc WLEDs, limiting their efficiency to a greater extent. The decrease in efficiency is mainly due to the fact that these phosphors do not have a strong absorption of the violet or blue LED radiation, resulting in LED package losses from scattering. Also, many of the traditional phosphors developed so far has Eu^{3+} , Tb^{3+} , or Mn^{2+} as the activators whose transitions are forbidden with long decay times ($>1\text{ ms}$), causing phosphor quenching due to saturation from the high LED radiation flux on the phosphor. The saturation-based quenching is not observed in phosphor systems containing Ce^{3+} and Eu^{2+} with $5d^1 \rightarrow 4f^1$ Ce^{3+} or $4f^6 5d^1 \rightarrow 4f^7$ Eu^{2+} emission transitions that have decay times of $<100\text{ ns}$ and $<3\text{ }\mu\text{s}$, respectively. Finally, the phosphor temperature in LED packages can be $>150^\circ\text{C}$, and many LFL/CFL and CRT phosphors used currently have strong quenching at these temperatures. These additional requirements necessitate the development of new phosphors specifically for pc-WLEDs.

The challenges and additional requirements for developing novel, efficient and stable LED phosphors are balanced by larger potential composition spaces for LED phosphors versus that for LFL/CFL phosphors. Many silicate phosphors darken in the Hg plasma due to Hg-adsorption, and can only be made useful when coated with a protective layer to prevent this absorption. However, such reactions doesn't takes place for LEDs, opening up many potential phosphor compositions. In water-based fluorescent lamp phosphor suspensions, the use of phosphors that decompose in water are restricted. In the modern scenario, most of the packaging protocols avoid aqueous processing conditions and these restrictions are less of an issue in fabrication of LEDs. Eventhough, the processing issues might be alleviated, there are still potential issues with phosphor

stability at high humidity conditions, 85% relative humidity and at high temperatures around 85°C, since pc WLEDs are not necessarily hermetically sealed.

The basic requirements of the phosphors for pcWLED applications have been met by the discovery and development of new phosphors over the past 10 years. In the mean time, the field of LED phosphors has drastically taken a giant step from a single family of phosphor compositions, the Ce³⁺-doped aluminate garnets to a variety of oxides, silicates, aluminates, nitrides, oxynitrides, sulfides, and fluorides compositions, leading to commercial LEDs that cover a full range of white CCTs.

1.6 Basic requirement of a phosphor to be used in pc-WLEDs

Vincentinus Casciarolo, an Italian alchemist coined the term *Phosphor* in the early 17th century. In search of a novel metal, a heavy crystalline stone was fired and it emitted with a glow at a volcanic site. After sunlight exposure, emission of red light was observed from the sintered stone in dark. The sintered stone was BaSO₄ and BaS was the fired product which is a well known host for phosphor materials.

In due course various developments happened in the field of phosphors and all luminescent materials cannot be used as phosphors for application purposes. There are certain basic requirements for a phosphor material when it comes to the application point of view. Some of them are listed as follows.

1. A higher absorption in the emission range of the LEDs and the maximum value of excitation must be within the wavelength range of the pumping LED.
2. Pure white light with excellent properties like CRI and CCT can be obtained as the resultant of the emissions from the developed phosphor and the other phosphors.
3. Higher quantum efficiency (QE) of the phosphors maximizing the electrical to optical conversion efficiency of the LED package.
4. Reduced thermal quenching so that the phosphors can be used at elevated temperatures.
5. Higher chemical and thermal stability and thereby free from photo-bleaching.
6. For the large scale production, synthesis route should be easy to be cost effective.

1.7 Lanthanides

The 4f-4f electronic transitions between the energy levels of trivalent lanthanide ions which are doped into a host lattice plays a significant role in understanding the

chemistry of rare earth activated phosphors. The wavelength down conversion approach to solid state lighting (SSL), makes use of down conversion materials to produce visible light when excited by near-UV or blue emission from InGaN LEDs, involve lanthanide ion excitation processes via incident light absorption, energy transfers between the various dopants present in the host, radiative relaxation of the excited lanthanide ions via photon emission, and non-radiative relaxation processes via phonon emission or transfer of energy.

Lanthanides have versatile and unique luminescent properties and are capable of light emission in a wide range of wavelengths, covering the ultraviolet (UV), visible and near-infrared (NIR) regions, making them as ideal candidates for many applications, including lasers, lighting and optical fibres.

The lanthanides (Ln) are the group of fifteen chemical elements in the periodic table, from atomic numbers 57 to 71 Lanthanum(La), Cerium(Ce), Praseodymium(Pr), Neodymium(Nd), Promethium(Pm), Samarium(Sm), Europium(Eu), Gadolinium(Gd), Terbium(Tb), Dysprosium(Dy), Holmium(Ho), Erbium(Er), Tellurium(Tm), Ytterbium(Yb), Lutetium(Lu). Yttrium (Y) and Scandium (Z = 21) are also often included with the 15 lanthanides within the group of rare-earth elements. The ground state electronic configuration of the neutral lanthanide atoms is a Xe core ($1s^2 2s^2 2p^6 3s^2 3p^6 4s^2 3d^{10} 4p^6 5s^2 4d^{10} 5p^6$), with two or three outer electrons ($6s^2$ or $6s^2 5d^1$), and as ones moves along the lanthanide series from Lanthanum (La $4f^0$) to Lutetium (Lu $4f^{14}$) the successive filling of the 4f electronic shell occurs in this order via the number of 4f electrons ranging from 0 to 14. The ionised trivalent lanthanides loses the 5d and 6s electrons. The intrinsic properties of lanthanides are governed by the presence of the deep lying 4f shell ions which is partially filled. The partially filled 4f shell electrons are screened by the interactions due to external forces of the overlying $5s^2$ and $5p^6$ shells resulting in a number of discrete energy levels. Hence, the energy level diagram of the free ion and the incorporated ion has a very close resemblance because the crystal lattice scarcely affects the position of these energy levels.

In most of the rare earth (RE) ions, the number of energy levels is relatively large, except in Ce^{3+} and Eu^{2+} (and Yb^{3+}). The Ce^{3+} ion has only one 4f electron and this gives rise to two energy levels; the orbital and spin moments of the electron are parallel in the one state and anti-parallel in the other state. As the number of 4 f electrons increases, in general, a rapid increase in the number of possible states is observed. The energy levels

in addition to the discrete 4f levels are broad hatched bands which depends on a great extend on the lattice. The energy bands is categorised into two groups. One of the 4f electrons is raised to the higher 5d level: $4f^n \rightarrow 4f^{n-1}5d$ in the first group and the lattice has a strong influence on the 5d level. One of the electrons of the surrounding anions is promoted to the 4f orbit of central RE ion in the second group and is known as the charge transfer (CT) band (Blasse 1979). The nature of the surrounding ion affects the position of this energy band.

Optical transitions of Lanthanides

Lanthanide ions exhibit three types of optical transitions: 4f-4f transitions, 4f-5d transitions, and charge-transfer state transitions

4f-4f optical transitions

The 4f-f optical transition corresponds to transition of electrons between the different energy levels of the 4f orbitals of the same lanthanide ion. The 4f-4f electric-dipole transitions of the rare earth ions are strictly forbidden as the parity does not change by the Laporte's selection rule. These transitions are not only forbidden by the parity selection rule but also by the change in the spin quantum number S of the total angular momentum quantum number L. Generally, the corresponding emission bands are usually weak and narrow although they are observed in practice. The spin prohibition and the parity prohibition are relaxed to an extend while considering certain particular systems. 7F levels being composed of states with six parallel spins is not entirely correct. By taking into consideration the spin-orbit coupling, the spin prohibition was cancelled, 7F states are composed of a pure 7F state with a slight admixture of the pure 5D state. The parity prohibition can be cancelled by the influence of the crystal lattice by mixing the $4f^6$ configuration with a state possessing a different parity. The interactions are due to the odd crystal field terms, if the RE ion is situated at a site which is a centre of symmetry in a crystal lattice, the parity prohibition cannot be relaxed. The splitting of the 4f levels due to the crystal field splitting is smaller as the 4f electrons are well shielded from the environment of the surrounding ions.

4f-5d transitions

In 4f-5d transitions, one of the 4f electrons is excited to a 5d orbital of higher energy [Hatakoshi 2007] and these transitions are allowed for the emission and

absorption of electric dipole radiation. This type of excitation is usually denoted $4f^n \rightarrow 4f^{n-1}5d$ and is typically observed in Ce^{3+} ions ($4f^1$ configuration). Since empty, half filled or completely filled electron shell configurations are the most stable ones, the excess 4f electron of Ce^{3+} is easily transferred to the 5d orbital. The absorption which is obtained from the reflection spectrum and the excitation spectrum lies in the ultraviolet part of the spectrum and takes place in a number of discrete bands. The crystal field strongly influences the excited 5d state and splits the 5d level into a number of levels, which in turn is determined by the crystallographic symmetry at the position of the rare earth ion. The spectral position of the absorption bands resulting from a particular 4f-5d transition varies because the crystal field splitting also varies considerably from one lattice to the other. Unlike 4f-4f transitions, 4f-5d transitions are allowed, which results in strong and broad absorption cross-sections.

Charge-transfer state (CTS) transitions

The next possible optical absorption is the charge-transfer state (CTS) transition, in which 2p electrons from the neighbouring anions (e.g. O^{2-} in oxides) are transferred to a 4f orbital. Eu^{3+} ($4f^6$) shows this type of absorption which needs one additional electron to reach the half-filled configuration. Charge-transfer state (CTS) transition points to allowed optical transitions and result in broad and intense absorptions. Unlike 4f-5d transitions, there is no distinct splitting in the absorption spectra.

Selection rules for optical transitions

The intensity of the intra configurational f-f transitions is proportional to the square of the transition momentum, M and according to group theory, a transition is allowed if $M \neq 0$. Light is an electromagnetic wave with their electric field and magnetic fields in planes perpendicular to the direction of propagation, electric dipolar transitions (ED) and magnetic dipolar transitions (MD) needs to be taken into account. Magnetic dipole transitions are usually significantly weaker than electric dipole transitions (about two orders of magnitude smaller for lanthanide ions).

Selection rules for Electric Dipole transitions

The electric dipole (ED) operator is odd. ED transitions can only occur if $\langle \Psi_i | \Psi_f \rangle$ is odd. Ψ_i and Ψ_f are the wavefunctions associated with the initial and final states which means that Ψ_i and Ψ_f must have opposite parities. This is the so-called parity rule or Laporte rule. Electric dipole transitions are allowed if:

$\Delta S = 0$, $\Delta L = \pm 1$ and $\Delta J \leq \pm 6$ (but $J = 0 \rightarrow J' = 0$ transitions are forbidden)

If $J = 0$, $\Delta L = \pm 1$ and $\Delta J = \pm 2, \pm 4, \pm 6$

Selection rules for Magnetic Dipole transitions

The magnetic dipole (MD) operator, unlike the ED operator, is even. Therefore, MD transitions can only occur if $\langle \Psi_i | \Psi_f \rangle$ is even, Ψ_i and Ψ_f have same parities. Magnetic dipole transitions are allowed if:

$\Delta S = 0$, $\Delta L = 0$ and $\Delta J = 0, \pm 1$ (but $J = 0 \rightarrow J' = 0$ transitions are forbidden)

If $J = 0$, $\Delta L = 0$ and $\Delta J = \pm 1$

Forced Electric Dipole transitions

The 4f-4f electric dipole transitions between the 4f states of an isolated trivalent lanthanide ion are parity forbidden by the Laporte's selection rule. The parity selection rule is usually relaxed, when the lanthanides are introduced into a crystal, due to the mixing of the 4f wave functions with a small amount of opposite-parity wave functions (e.g. 5d states, charge transfer states, etc). As a result, forced electric dipole transitions are observed. These emissions are usually weak and very narrow.

1.8 Luminescence properties of Dy³⁺

The trivalent lanthanide activators possess special optical properties such as narrow and strong luminescence, long life times, emissions in the entire visible region (red, green and blue), good thermal and chemical stability. [Yuhua *et al.* 2015, Lin *et al.* 2011] Among these, trivalent dysprosium (Dy³⁺) ion is an excellent activator and have wide applications in mercury free lamps, field emission displays, and plasma display panels. Dysprosium has an atomic number of 66 and Dy³⁺ ion has 9 electrons in the 4f shell and the energy level diagram is given in the Figure 1.4. The yellow (570-600 nm) and blue (470-500 nm) emission bands in the visible region are assigned to the forbidden electric dipole transition of ${}^4F_{9/2} \rightarrow {}^6H_{13/2}$ and the allowed magnetic dipole transition of ${}^4F_{9/2} \rightarrow {}^6H_{15/2}$ respectively. [Blasse G 1994] Near white light emission in Dy³⁺ doped luminescent materials is obtained by controlling the yellow to blue (Y/B) intensity ratio to a desired level. The above Dy³⁺ ion transitions mainly depends on the site symmetry, host composition, excitation wavelength and doping concentration of Dy³⁺ at the luminescent centers. [Liu *et al.* 2012, Deng *et al.* 2014] Thus, the Y/B ratio of Dy³⁺

emission is greatly influenced by the covalent effect between Dy^{3+} and O^{2-} and it inversely relates with Z/r , where Z is the charge and r the ionic radius, or electronegativity of the surrounding element M in the ternary oxide Dy-O-M . [Su *et al.* 1993] The intra-configurational f-f transitions of RE^{3+} ions have weak excitation levels on account of forbidden parity selection rules. Therefore, the luminescence efficiency of RE^{3+} ions can be greatly improved by transferring the energy from a foreign species to RE^{3+} ions. [Naidu *et al.* 2012] Thereby, there is an immense interest in discovering white light emission phosphors based on a single luminescent center making use of the Dy^{3+} ions emission lines. Asymmetric ratio, the relative integrated intensity ratio of the electric dipole allowed (${}^4\text{F}_{9/2}$ - ${}^6\text{H}_{13/2}$) to the magnetic dipole allowed (${}^4\text{F}_{9/2}$ - ${}^6\text{H}_{15/2}$) transition depends on the host crystal structure and gives a measure of the structural distortion around Dy^{3+} ions and the nature of the doping sites. [Zhou *et al.* 2007] Reports show that the Y/B ratio of Dy^{3+} increases with the increase in the ionic radius of its surrounding elements. Thus, Dy^{3+} can be used as a luminescent structural probe to determine the site symmetry of rare earth ions.

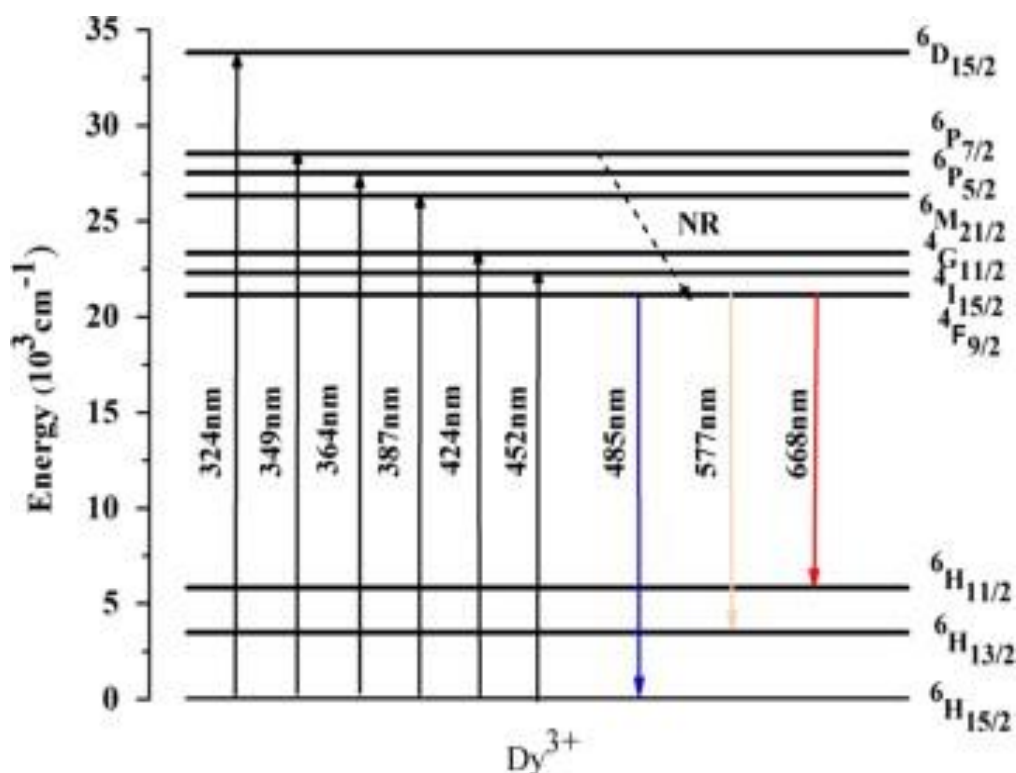


Figure 1.4 : The energy level diagram of Dy^{3+} ion.

1.9 A collection from the past

Due to the inherent and interesting luminescent properties, scheelite based metal tungstates (AWO_4 , A = Ca, Sr, Ba, Pb) have been investigated over the years and finds potential applications in various fields, such as solid-state lasers, phosphors, and scintillators. The A atoms are coordinated to eight oxygen atoms, forming the AO_8 clusters and the B atoms are surrounded by four oxygen atoms, forming the tetrahedral BO_4 clusters. Calcium tungstate ($CaWO_4$) is a self-activated blue emitting luminescent material and its photoluminescence properties can be modulated by the doping of RE ions like Eu^{3+} , Dy^{3+} , Sm^{3+} , and Tb^{3+} . WO_4^{2-} group has a strong broad absorption band in the near-ultraviolet (n-UV) region due to the charge transfer (CT) from oxygen to metal. Thus, the energy transfer (ET) process easily occurs from WO_4^{2-} group to RE ions, which in turn leads to a high external quantum efficiency of RE ions doped $CaWO_4$ phosphors.

Du *et al.* synthesized $CaWO_4 : xDy^{3+}$ color tunable phosphors by a simple conventional solid state reaction and reported that the emission color of $CaWO_4 : xDy^{3+}$ can be suitably tuned from blue to green, and finally to yellow by the modulation of excitation wavelength and Dy^{3+} ion concentration. The luminescent properties were investigated as a function of Dy^{3+} ion concentration under 258 nm and 353 nm. Electric dipole-dipole interaction is the cause behind concentration quenching for $x = 0.05$. The emission spectra of phosphors exhibited the characteristic blue yellow emission from Dy^{3+} ions and the cathodoluminescence spectra measured at different accelerating voltages and filament currents are consistent with the photoluminescence spectrum excited at 258 nm. The phosphors with tunable emissions may find potential applications in the fields of miniature color displays in the near future. [Du *et al.* 2015]

Sharma *et al.* reported the luminescence properties of $CaMO_4 : xDy^{3+}$ (M = Mo, W) nanoparticles prepared by an ethylene glycol route. Photoluminescence examinations revealed that all the doped phosphors shows yellow phosphorescence for tungstate samples and yellowish white for molybdate nanoparticles. The optimum doping concentration was obtained as $x = 0.07$ for $CaMoO_4 : xDy^{3+}$ samples and $x = 0.05$ for $CaWO_4 : xDy^{3+}$ samples. Dy^{3+} doping in the host tunes the emission wavelength from blue-green to white for $CaMoO_4$ and blue to yellow for $CaWO_4$ nanoparticles. This multicolour tuning emission could increase their applicability in fluorescent lamps and display panels. [Sharma *et al.* 2015]

Zhu *et al.* proposed a general hydrothermal route for the synthesis of nanocrystalline lanthanide stannates ($\text{Ln}_2\text{Sn}_2\text{O}_7$ ($\text{Ln}=\text{Y}, \text{La}-\text{Yb}$)) except for the radioactive Promethium. The mole ratio and the hydrothermal temperature played an important role in this hydrothermal synthesis. All the samples crystallized in cubic pyrochlore structure and can be indexed with their respective lanthanide stannates. Due to their high chemical stability, high melting points and efficient photoluminescence, rare-earth stannates may be promising phosphor materials. Photoluminescence studies of $\text{Tb}_2\text{Sn}_2\text{O}_7$, $\text{Dy}_2\text{Sn}_2\text{O}_7$ and $\text{Yb}_2\text{Sn}_2\text{O}_7$ were carried out and the $\text{Tb}_2\text{Sn}_2\text{O}_7$ exhibited photoluminescence in the green spectral region of 480–630 nm at 543 nm, caused by the $^5\text{D}_4 \rightarrow ^7\text{F}_5$ transition of Tb^{3+} . $\text{Yb}_2\text{Sn}_2\text{O}_7$ materials showed charge transfer luminescence of Yb^{3+} and this type of luminescence is important as these materials find possible applications in scintillation detectors in neutrino physics. CT luminescence is characterized by a broad emission band in the UV–vis spectral region. [Zhu *et al.* 2008]

Wang *et al.* reported the luminescent properties of Dy^{3+} doped $\text{La}_2\text{Sn}_2\text{O}_7$ nanocrystals through combustion synthesis and the transfer of energy from the $\text{La}_2\text{Sn}_2\text{O}_7$ host to dysprosium ions is also discussed. The pyrochlore structured nanocrystals with a hexagonal morphology less than 50 nm was synthesized for the first time. The full width at half maximum of the diffraction peaks of the Dy^{3+} doped $\text{La}_2\text{Sn}_2\text{O}_7$ nanocrystals is broader than that of the undoped samples indicating that the particle size decreases to a much smaller dimension by the doping of the Dy^{3+} ions into the lattice. [Wang *et al.* 2007]

Wang *et al.* performed the luminescence properties of $\text{La}_{2-x}\text{RE}_x\text{Sn}_2\text{O}_7$ ($\text{RE} = \text{Eu}$ and Dy) phosphor nanoparticles via a co-precipitation method and studied the effect of Eu^{3+} doping and $\text{Eu}^{3+}/\text{Dy}^{3+}$ co-doping on the luminescence properties of $\text{La}_2\text{Sn}_2\text{O}_7$ phosphors. The optimum concentration of the $\text{Eu}^{3+}/\text{Dy}^{3+}$ codoped $\text{La}_2\text{Sn}_2\text{O}_7$ is $x = 0.05$. The enhancement in the emission intensities is due to the efficient energy transfer from the Dy^{3+} ions to the Eu^{3+} ions. The exact mechanism underlying this concentration quenching phenomena is still not clear and can be due to the contributions from the interactions among the doped ions, energy migration through the lattice and cluster of activators, which act as killer sites. [Wang *et al.* 2006]

Cheng *et al.* investigated the photoluminescence and the catalytic oxidation activities in a series of rare earth stannates $\text{Ln}_2\text{Sn}_2\text{O}_7$ ($\text{Ln} = \text{Y}, \text{La}, \text{Pr}, \text{Nd}, \text{Sm}, \text{Eu}, \text{Tb}, \text{Dy}, \text{Ho}, \text{Er}, \text{Tm}, \text{Yb}$ and Lu), prepared by a general aqueous sol-gel route and inferred

that the properties changed remarkably with the variation of ionic radii of the rare earth elements. As the rare earth ionic radii decreases from La^{3+} to Lu^{3+} all the X-ray diffractions peaks are shifted to higher 2θ diffraction angle leading to a decrease in the lattice parameter. The lattice parameter decreases with a decrease in the ionic radii of the rare earth ions conforming to the lanthanide contraction phenomena. The catalytic performance on the CO oxidation indicates that the conversion of CO to CO_2 started at 120°C has a linear relationship with temperature regardless of the $\text{Ln}_2\text{Sn}_2\text{O}_7$ catalyst. However, on closer investigation, it is revealed that the CO oxidation activity changed significantly and has a dependence on the rare earth ion. [Cheng *et al.* 2008]

Eu^{3+} and Dy^{3+} - doped $\text{La}_2\text{Zr}_2\text{O}_7$ nanocrystals were prepared by an energy saving sol gel combustion method by Zhang *et al.* Among the rare earth ions, La^{3+} has a luminescence inertia and hence $\text{La}_2\text{Zr}_2\text{O}_7$ is selected as host material for the luminescent centers. Generally, $\text{RE}_2\text{Zr}_2\text{O}_7$ prepared at lower temperatures commonly forms the fluorite structure, in the present system, $\text{La}_2\text{Zr}_2\text{O}_7$ forms the pyrochlore phase even at a relatively lower temperature by the change in the processing conditions. All the doped samples exhibited the characteristic transitions of Eu^{3+} at 590nm ($^5\text{D}_0$ - $^7\text{F}_1$) and 610-630 nm range ($^5\text{D}_0$ - $^7\text{F}_2$) and Dy^{3+} transitions. The codoped samples have a prominent emission in the orange region due to the enforcement of the Eu^{3+} emission by the Dy^{3+} ions due to the migration of energy from Dy^{3+} to Eu^{3+} . [Zhang *et al.* 2006]

A single host white emitting phosphor, $\text{CaLaGa}_3\text{O}_7$ doped with varying concentration of Dy^{3+} was synthesized by chemical co-precipitation by Zhao *et al.* 2012. The Dy^{3+} ions acted as luminescent centers in the lattice, and are substituted for La^{3+} ions considering the matching ionic radius and valency in the single crystal lattice of $\text{CaLaGa}_3\text{O}_7$ where they were located in C_s sites. The phosphors showed the characteristic emissions of Dy^{3+} , Dy^{3+} are mainly located at a site lacking inversion symmetry, with intense yellow emission at 573 nm and the mechanism underlying the phenomena are also discussed and can be applied in both field emission displays and plasma display panels. [Zhao *et al.* 2012].

Kazakova *et al.* studied the optical absorption and the luminescence spectra of rare-earth tantalate single crystals RTaO_4 ($\text{R} = \text{Nd, Sm, Eu, Gd, Tb, Dy, Ho, Er, Tm, Yb, Y}$). and the possible mechanisms of luminescence with different rare-earth atoms R are also discussed. The single crystals crystallize in the fergusonite structure which is a distorted scheelite structure with a space group $\text{I}_{2/a}$. Luminescence is observed in YTaO_4 ,

TbTaO₄, EuTaO₄ and GdTaO₄ and all other matrices showed no luminescence. Intrinsic tantalate group luminescence may be the cause for the emission band in YTaO₄ single crystals where the tantalate group and the rare earth ions are excited by an X ray source. The two weak bands at 315 nm and 550 nm in the GdTaO₄ sample are due to the Gd³⁺ ion luminescence (⁶P_{7/2} - ⁸S_{7/2}) and by defects in the tantalate group surroundings (F-type centers), respectively. The nature of luminescence in these tantalate based single crystals is quite complicated and it depends on the nature of the tantalate group and the rare earth atoms. [Kazakova *et al.* 1997]

1.10. Objectives of the study

Researchers, chemists, physicists, and materials scientists all over the world are working single handed in the discovery and optimization of new phosphor materials that will contribute significantly in the day to day needs of the common man. In spite of the rapid progress that have been achieved, there are still many challenges and problems that need to be addressed to develop new phosphor materials to reach a supreme realm in replacing the conventional lighting technologies and paving a way for the global energy crisis. The discovery of new phosphor compositions is one step toward pc-WLEDs implementation with extensive process optimization including the various powder processing techniques and/or other ceramic processing methods such as sintering or glass-ceramic formation to make uniform phosphor parts and plates required to maximize conversion efficiencies and to obtain full color emission phosphors.

The commercially available pc-WLED produces white light by the combination of the complimentary colors, blue light from an InGaN chip and the yellow light from Ce³⁺ doped yttrium aluminium garnet (YAG:Ce³⁺) phosphor. However, the blue part of the white light is greatly governed by the drive current, temperature and the amount of phosphor. At this juncture, the output from an ultraviolet (UV) light source takes up the contribution of the InGaN chip in white light generation. UV LED chip-based WLEDs have great color stability when compared with the first method as all the colors are produced by phosphors. This approach has the main drawback of low luminescence efficiency due to the re-absorption of emission colors. White light emission can be produced in a single phase host by solely doping or multi doping of activator ions with good control of the emission colors, however the luminous emission efficiency and intensity still needs to be improved. The white light emitting luminescent materials based

on single phase possess unique advantages and have a greater control over multiple compositional phosphors in the form of color rendering and luminous efficiency by considering the color re-absorption and ratio control problems among phosphors. Therefore, the development of potential luminescent materials for display and lighting devices necessitates the search for new, thermally and chemically stable and good efficient single phase white light emitting phosphor materials with strong excitation strengths in the n-UV and blue range, which fulfils the demand of enhancing the luminescence efficiency and reproducibility of pc-WLEDs.

Chapter 2

Photoluminescent properties of single phase white light emitting phosphors $\text{Ca}(\text{La}/\text{Gd})_{1-x}\text{Nb}(\text{Mo}/\text{W})\text{O}_8 : x \text{Dy}^{3+}$

Parvathi S. Babu, et al.; Mater. Lett. 170 (2016) 196-198.

Abstract

A series of Dy^{3+} doped $\text{Ca}(\text{La}/\text{Gd})_{1-x}\text{Nb}(\text{Mo}/\text{W})\text{O}_8$ ($x = 0.020, 0.025, 0.030, 0.035, 0.050, 0.075$) phosphors were synthesized using a high temperature solid state method. Powder XRD, SEM, UV–Visible absorption spectroscopy, photoluminescence spectroscopy were used to investigate the structure, morphology, absorbance, photoluminescence respectively. Powder XRD results confirm the tetragonal phase for all the samples and detailed investigations on the photoluminescence properties indicated that Dy^{3+} doped $\text{Ca}(\text{La}/\text{Gd})_{1-x}\text{Nb}(\text{Mo}/\text{W})\text{O}_8$ phosphors has a strong absorption in near UV region and two sharp emission peaks in the visible region. The yellow (575/576 nm) and blue emissions (478/479nm, 487/488 nm) upon UV excitation resulted from the forced electric dipole transition of ${}^4\text{F}_{9/2} \rightarrow {}^6\text{H}_{13/2}$ and the magnetic dipole transition of ${}^4\text{F}_{9/2} \rightarrow {}^6\text{H}_{15/2}$ respectively. The luminescence emission properties of the samples have been investigated upon 351/352 nm, 366 nm, and 386/387 nm excitation and the emission colours of all the doped samples are located in the white light region. Therefore, Dy^{3+} doped $\text{Ca}(\text{La}/\text{Gd})_{1-x}\text{Nb}(\text{Mo}/\text{W})\text{O}_8$ phosphors can serve as a promising candidate for single-phase white-light emitting phosphors under near UV excitation.

2.1 Introduction

In recent years, with the advancement in the materials technology, there is a growing interest in developing inorganic phosphors that produce white light when doped with lanthanides. Solid state lighting offers high luminous efficiency, low power consumption, reliability, superior life time and environmental friendliness.[Phillips *et al.* 2007] White light emitting diodes are regarded as the next generation solid state lighting sources as they offer advantages over conventional lighting technologies like incandescent and fluorescent lamps. Exploring novel luminescent materials for WLEDs with high luminous efficacy, high quantum efficiency, high chromatic stability, brilliant color rendering properties, low correlated color temperature, thermal and chemical stability and price competitiveness has been a major challenge to material researchers.[Justel *et al.* 1998, Ye *et al.* 2010] One method of generating white light includes the combination of a blue InGaN LED chip and YAG:Ce³⁺ yellow emitting phosphor, however this method lacks good color rendering index (CRI) and stability of color temperature (CCT) and also the lighting color of the WLEDs fabricated by this method changes with drive voltage and the thickness of the phosphor coatings making it undesirable for large scale industrial production. The next method involves tri-color phosphors RGB (red-green-blue) excited by an ultraviolet source, although the CRI values are improved, however, the luminescence efficiency is relatively low owing to the strong re-absorption of the blue light by the red and green phosphors. Also the WLED device fabrication is quite complicated and it is difficult to control the color balance. There is a great demand for developing novel, stable and efficient single phase white light emitting phosphor that can be effectively excited in the near UV/blue region and has attracted much attention for white LED applications. The currently used methods for realizing white light emission in a single phase host involves doping of a single rare earth ion (Dy³⁺, Eu²⁺) into an appropriate host matrix, or by co-doping of suitable activators like Tm³⁺, Tb³⁺, Eu³⁺, Ce³⁺ simultaneously along with Dy³⁺ in hosts, by co-doping of different activator ions to control emission color via energy transfer (ET) processes, and also by controlling the defect concentrations and reaction conditions for defect-related luminescent materials.[Shang *et al.* 2014]

Dysprosium (Dy³⁺) ions exhibits two main emissions in the visible region, the yellow (570-600 nm) and blue (470-500 nm) emissions which are attributed to the forced electric dipole (ED) transition of $^4F_{9/2} \rightarrow ^6H_{13/2}$ and the magnetic dipole (MD) transition of

${}^4F_{9/2} \rightarrow {}^6H_{15/2}$ respectively. [Blasse G 1979] The hypersensitive ${}^4F_{9/2} \rightarrow {}^6H_{13/2}$ ($\Delta L = 2$, $\Delta J = 2$) transition of Dy^{3+} is strongly influenced by the crystal field environment of Dy^{3+} , hence Dy^{3+} ions can be used to probe the local structure of luminescent centers in a definite host lattice whereas the magnetic dipole transition hardly varies with the local symmetry. The emission has a white color which turns to yellow in host lattices where hypersensitivity is pronounced. [Blasse G 1994] The emission from Dy^{3+} ions has great dependence on the site symmetry and the chemical nature of the surrounding ions and the luminescent centers. When Dy^{3+} ions are located at a site with an inversion centre and high symmetry, luminescence is not observed. The yellow-to-blue intensity ratio (Y/B) of $CaNb_2O_6$, $Ca_2Nb_2O_7$, YVO_4 , $LaVO_4$, $Ba_2YV_3O_{11}$, $Ba_2GdV_3O_{11}$, $Ba_2LaV_3O_{11}$ clearly reveals that Y/B ratio of Dy^{3+} ions located at a site deviated from an inversion centre is greater than that located at a site without an inversion centre. Thus, the Y/B ratio of Dy^{3+} emission is mainly influenced by the nephelauxetic effect between Dy^{3+} and O^{2-} and it increases with decreasing Z/r , where Z is the charge and r the ionic radius, or electronegativity of the surrounding element M in the complex oxides Dy-O-M. [Su *et al.* 1993]

Rare earth doped molybdates and tungstates with powellite/scheelite structure are considered as good host lattices under n-UV (near-UV) or blue excitation due to its MoO_4/WO_4 tetrahedron unit and also for the luminescence of Dy^{3+} ions because of their excellent thermal and chemical stability. [Kaczmarek *et al.* 2013] In the $CaMoO_4$ host, each of the central molybdenum atom is coordinated to four oxygen atoms forming a relatively stable tetrahedral configuration and the cations to eight oxygen atoms from different tetrahedra. They belong to the tetragonal crystal structure with a space group of $I41/a$ and contains two formula units per unit cell. The MoO_4^{2-} complex has a strong absorption in the ultraviolet (UV) region due to the charge transfer from the oxygen to metal, resulting in the energy transfer from the MoO_4^{2-} group to the rare earth ions, thereby greatly enhancing the quantum efficiency of rare earth activated phosphors. $CaMoO_4 : Dy^{3+}$ phosphors codoped with K^+ , as a charge compensator prepared by hydrothermal method have been reported [Dutta *et al.* 2013] and white light emission is obtained in $CaLa_{1-x}NbMoO_8 : xDy^{3+}$ without codoping with charge compensation ions as Dy^{3+} ions are doped to the La^{3+} ion site. $CaMoO_4 : Dy^{3+}$ is an extensively studied material and has been prepared by ethylene glycol route, [Sharma *et al.* 2013] solid state ceramic method etc. Thus there is a growing need for exploring novel inorganic phosphor materials for lighting applications. In this regard, a series of $Ca(La/Gd)_{1-x}Nb(Mo/W)O_8$:

$x\text{Dy}^{3+}$ ($x = 0.020, 0.025, 0.030, 0.035, 0.050, 0.075$) samples have been synthesized by the conventional solid state route.

2.2 Experimental section

2.2.1 Synthesis

Preparation of $Ca(La/Gd)_{1-x}Nb(Mo/W)O_8: x\text{Dy}^{3+}$ ($x = 0.020, 0.025, 0.030, 0.035, 0.050, 0.075$) samples:

In the present work, a series of molybdate based powellite type white emitting phosphors $Ca(La/Gd)_{1-x}NbMoO_8: x\text{Dy}^{3+}$ ($x = 0.020, 0.025, 0.030, 0.035, 0.050, 0.075$) and tungstate based schellite type white emitting phosphors $Ca(La/Gd)_{1-x}NbWO_8: x\text{Dy}^{3+}$ ($x = 0.020, 0.025, 0.030, 0.035, 0.050, 0.075$) samples were prepared by the conventional solid state route using CaCO_3 , $\text{La}_2\text{O}_3/\text{Gd}_2\text{O}_3$, Nb_2O_5 , MoO_3/WO_3 , Dy_2O_3 (All chemicals are from Sigma Aldrich with 99.99% purity) as the starting materials. The required stoichiometric amounts of these materials were weighed and then mixed thoroughly in an agate mortar using acetone as the wetting medium. The mixing was followed by drying in an air oven maintained at a temperature of 100°C . The process of mixing and drying was repeated thrice to obtain a homogeneous mixture. The homogeneous mixture was made into a pellet and initially calcined at 1200°C for 6 hours on an alumina plate in an air atmosphere furnace. The calcination was repeated at 1200°C for 6 hours with intermittent grinding to obtain the final single phase sample. The calcined pellet was then ground into a fine powder for further characterizations.

2.2.2 Characterisation techniques

The crystalline structure and phase purity of the samples were examined by recording XRD patterns using a powder X-ray diffractometer (X'Pert Pro PANalytical) operated at 40 kV/30 mA with a Ni filtered Cu-K α radiation ($\lambda = 0.15406$ nm) in the 2θ range from 10° to 90° in 0.016° steps. Morphological studies of powder particles were done by a scanning electron microscope (JEOL, JSM-5600LV) operated at 15kV. Absorbance study of the samples were carried out using a Shimadzu, UV-2450 UV-Vis spectrophotometer in the 400–700 nm wavelength range using barium sulfate as a reference. The photoluminescence spectra were recorded on a Fluorolog HORIBA fluorescence spectrophotometer with a Xe lamp (450 W) as the excitation source. Luminescence lifetime of the phosphors was recorded by the phosphorimeter attached to

the Fluorolog@3 spectrofluorimeter. CIE chromaticity coordinates was calculated using the software CIE calculator.

2.3 Results and discussion

2.3.1. Powder X-ray diffraction analysis

Powder X-ray diffraction patterns of $\text{CaLa}_{1-x}\text{NbMoO}_8 : x\text{Dy}^{3+}$ ($x = 0.020, 0.025, 0.030, 0.035, 0.050, 0.075$) and $\text{CaGd}_{1-x}\text{NbMoO}_8 : x\text{Dy}^{3+}$ ($x = 0.020, 0.025, 0.030, 0.035, 0.050, 0.075$) samples are given in Figure 2.1 and Figure 2.2 respectively.

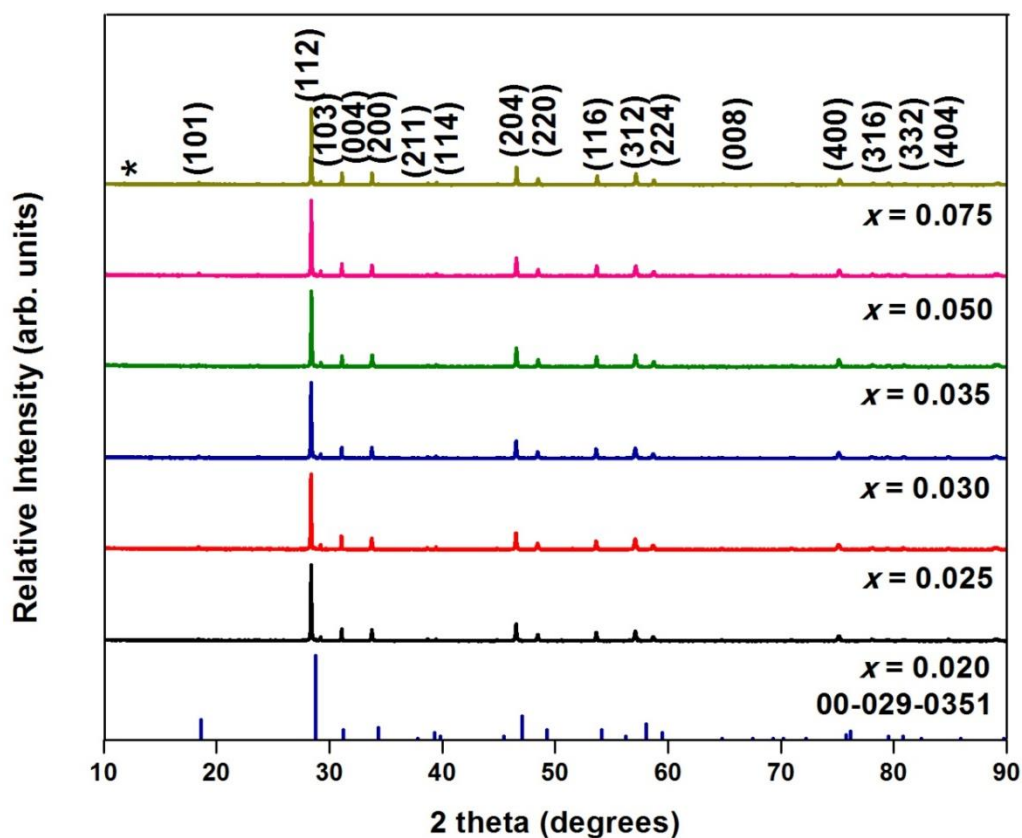


Figure 2.1: Powder X-ray diffraction patterns of $\text{CaLa}_{1-x}\text{NbMoO}_8 : x\text{Dy}^{3+}$ ($x = 0.020, 0.025, 0.030, 0.035, 0.050, 0.075$).

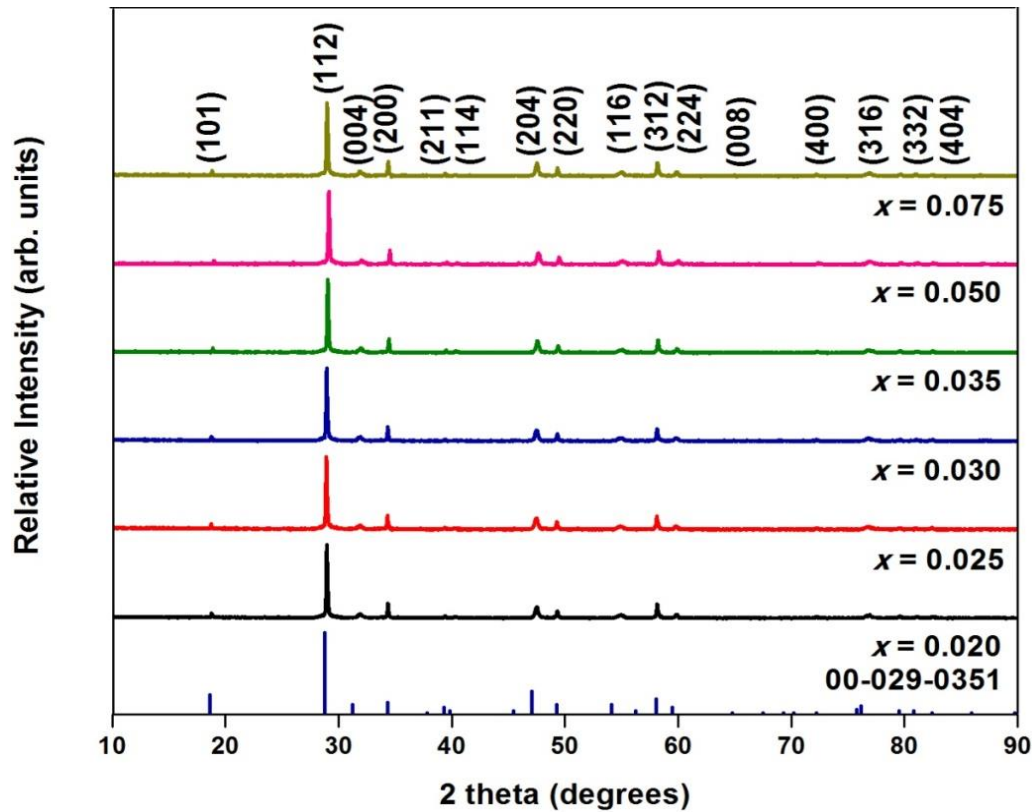


Figure 2.2 : Powder X-ray diffraction patterns of $\text{CaGd}_{1-x}\text{NbMoO}_8:x\text{Dy}^{3+}$ ($x = 0.020, 0.025, 0.030, 0.035, 0.050, 0.075$).

All the samples were in good agreement with the reported diffraction pattern of CaMoO_4 (JCPDS no. 00-29-0351; tetragonal powellite; space group $I4_1/a$). [Thomas *et al.* 2009] No extra peaks from impurities were observed and samples are highly crystalline due to the presence of the sharp and intense peaks. The prominent peaks corresponding to (112), (004), (200), (204), (220), (116) and (312) lattice planes are observed. In $\text{CaLa}_{1-x}\text{NbMoO}_8:x\text{Dy}^{3+}$ and $\text{CaGd}_{1-x}\text{NbMoO}_8:x\text{Dy}^{3+}$ host lattices, Ca^{2+} , $\text{La}^{3+}/\text{Gd}^{3+}$ and Dy^{3+} ions occupies the A site and are eight coordinated forming AO_8 polyhedra. Nb^{5+} and Mo^{6+} ions occupy the B sites and are coordinated to four oxygen atoms forming BO_4 tetrahedra. In the AO_8 polyhedra, each oxygen atom is connected to one Nb/Mo atoms. Thus, the two A atoms and one Nb/Mo atom is shared by each oxygen atom. Powellite structure results from the cubic close packing of A atoms and $\text{NbO}_4/\text{MoO}_4$ tetrahedral units in an ordered manner. One expects the Ca, La/Gd to be occupied at a VIII coordinated site (wyckoff coordinates, 4b: 0, 1/4, 5/8), and Mo and Nb in a VI coordinated site (wyckoff coordinate, 4a : 0, 1/4, 1/8) and O at (16f : x, y, z) site. At higher doping concentrations of Dy^{3+} ($x = 0.075$) a small intensity peak at $\sim 12^\circ 2\theta$

(marked as *) is observed which could be due to the presence of dysprosium molybdate for the $CaLa_{1-x}NbMoO_8:xDy^{3+}$ samples. Considering the matching ionic radius and valency one expects the Dy^{3+} (ionic radius : 0.1027 nm, CN = 8) ions to be doped to the La^{3+} (ionic radius : 0.116 nm, CN = 8)/ Gd^{3+} (ionic radius : 0.105 nm, CN = 8) sites than to the Ca^{2+} (ionic radius : 0.112 nm) site. The diffraction peaks of $CaLaNbMoO_8:Dy^{3+}$ are shifted to higher angles with increase in the concentration of Dy^{3+} , it can be incurred that this is due to the smaller ionic radius of Dy^{3+} than La^{3+} .

Table 2.1 : Lattice parameters and unit cell volume of $CaLa_{1-x}NbMoO_8:xDy^{3+}$ ($x = 0.020, 0.025, 0.030, 0.035, 0.050, 0.075$) samples.

x	Lattice Parameters		Unit Cell Volume
	a = b (Å)	c (Å)	(Å) ³
0.020	5.2397	11.5978	318.409
0.025	5.2316	11.5943	317.336
0.030	5.2307	11.5936	317.200
0.035	5.2304	11.5899	317.065
0.050	5.2266	11.5866	316.513
0.075	5.2224	11.5788	315.799

The lattice volume was found to decrease from $318.409 \times 10^{-3} \text{ (nm)}^3$ to $315.799 \times 10^{-3} \text{ (nm)}^3$ for the $CaLa_{1-x}NbMoO_8:xDy^{3+}$ samples and from $308.855 \times 10^{-3} \text{ (nm)}^3$ to $308.189 \times 10^{-3} \text{ (nm)}^3$ for the $CaGd_{1-x}NbMoO_8:xDy^{3+}$ samples with the increase in the Dy^{3+} concentration varying between 0.020 and 0.075 indicating the incorporation of Dy^{3+} ions into the lattice. Lattice parameters and unit cell volumes of Dy^{3+} doped $CaLa_{1-x}NbMoO_8$ and Dy^{3+} doped $CaGd_{1-x}NbMoO_8$ samples are listed in Table 2.1 and Table 2.2 respectively.

Table 2.2: Lattice parameters and unit cell volume of $CaGd_{1-x}NbMoO_8:xDy^{3+}$ ($x = 0.020, 0.025, 0.030, 0.035, 0.050, 0.075$) samples.

x	Lattice Parameters		Unit Cell Volume
	a = b (Å)	c (Å)	(Å) ³
0.020	5.2358	11.2665	308.855
0.025	5.2357	11.2641	308.778
0.030	5.2355	11.2641	308.754
0.035	5.2347	11.2623	308.611
0.050	5.2338	11.2525	308.236
0.075	5.2337	11.2512	308.189

Powder X-ray diffraction patterns of $CaLa_{1-x}NbWO_8:xDy^{3+}$ ($x = 0.020, 0.025, 0.030, 0.035, 0.050, 0.075$) and $CaGd_{1-x}NbWO_8:xDy^{3+}$ ($x = 0.020, 0.025, 0.030, 0.035, 0.050, 0.075$) samples are given in Figure 2.3 and Figure 2.4 respectively. All the samples were in good agreement with the reported diffraction pattern of $CaWO_4$ (JCPDS no. 00-41-1431; tetragonal scheelite; space group $I4_1/a$). [Thomas *et al.* 2011] No extra peaks from impurities were observed and samples are highly crystalline due to the presence of the sharp and intense peaks. The prominent peaks corresponding to (112), (004), (200), (204), (220), (116) and (312) lattice planes are observed. In $CaLa_{1-x}NbWO_8:xDy^{3+}$ and $CaGd_{1-x}NbWO_8:xDy^{3+}$ host lattices, Ca^{2+} , La^{3+}/Gd^{3+} and Dy^{3+} ions occupies the A site and are eight coordinated forming AO_8 polyhedra. Nb^{5+} and W^{6+} ions occupy the B sites and are coordinated to four oxygen atoms forming BO_4 tetrahedra. In the AO_8 polyhedra, each oxygen atom is connected to one Nb/W atoms. Thus, the two A atoms and one Nb/W atom is shared by each oxygen atom. Scheelite structure results from the cubic close packing of A atoms and NbO_4/WO_4 tetrahedral units in an ordered manner. One expects the Ca, La/Gd to be occupied at a VIII coordinated site (wyckoff coordinates, 4b: 0, 1/4, 5/8), and W and Nb in a VI coordinated site (wyckoff coordinate, 4a : 0, 1/4, 1/8) and O at (16f : x, y, z) site.

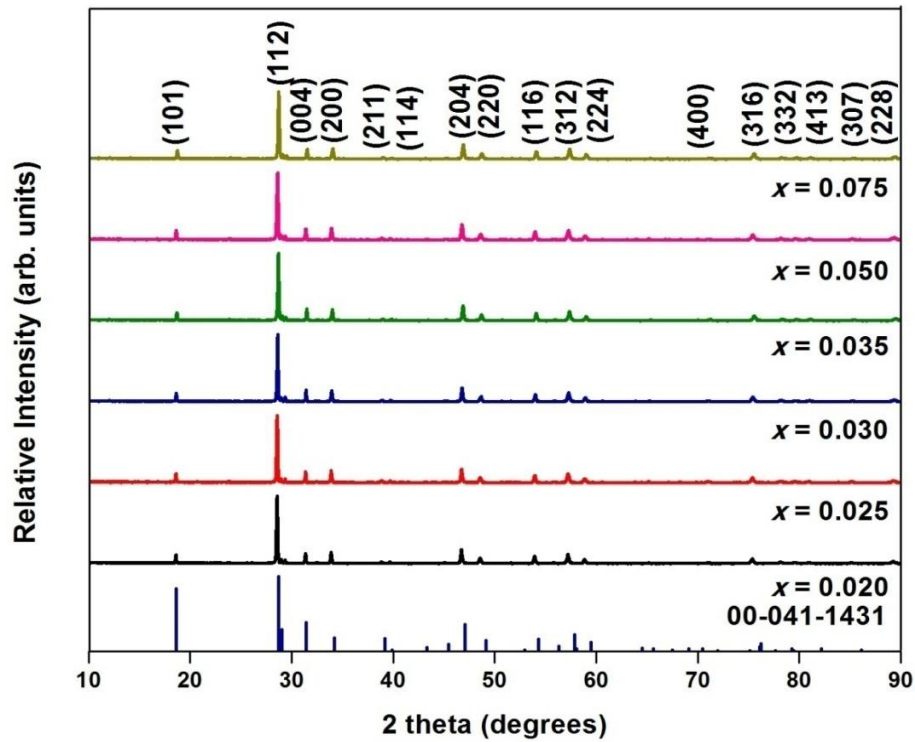


Figure 2.3 : Powder X-ray diffraction patterns of $\text{CaLa}_{1-x}\text{NbWO}_8:x\text{Dy}^{3+}$ ($x = 0.020, 0.025, 0.030, 0.035, 0.050, 0.075$).

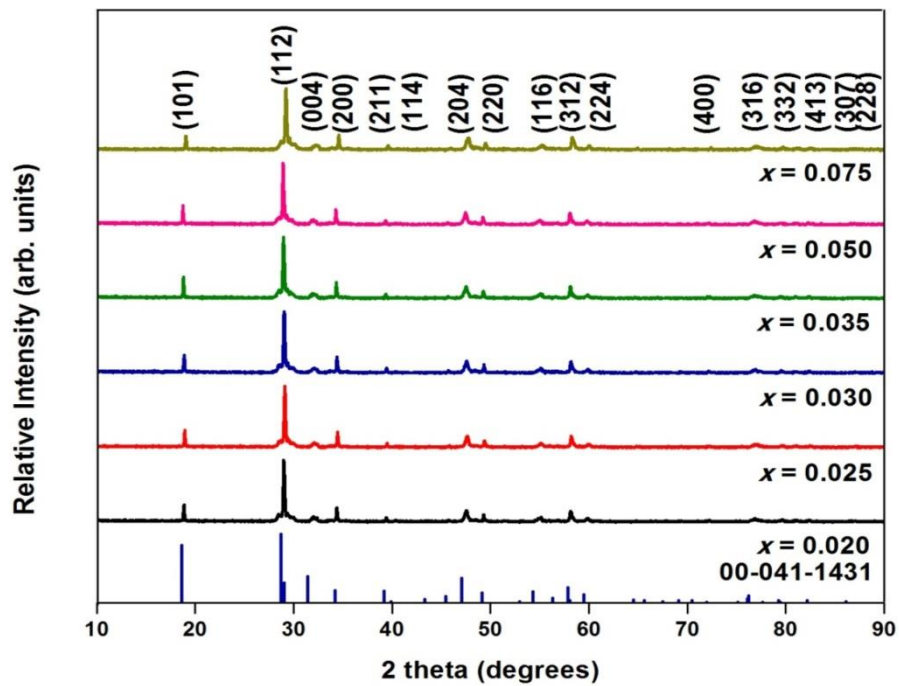


Figure 2.4: Powder X-ray diffraction patterns of $\text{CaGd}_{1-x}\text{NbWO}_8:x\text{Dy}^{3+}$ ($x = 0.020, 0.025, 0.030, 0.035, 0.050, 0.075$).

Considering the matching ionic radius and valency one expects the Dy^{3+} (ionic radius : 0.1027 nm, CN = 8) ions to be doped to the La^{3+} (ionic radius : 0.116 nm, CN = 8)/ Gd^{3+} (ionic radius : 0.105 nm, CN = 8) sites than to the Ca^{2+} (ionic radius : 0.112 nm) site.

Table 2.3 : Lattice parameters and unit cell volume of $CaLa_{1-x}NbWO_8:xDy^{3+}$ ($x = 0.020, 0.025, 0.030, 0.035, 0.050, 0.075$) samples.

x	Lattice Parameters		Unit Cell Volume
	a = b (Å)	c (Å)	(Å) ³
0.020	5.3541	11.5123	330.016
0.025	5.3447	11.5072	328.713
0.030	5.3441	11.4961	328.322
0.035	5.3425	11.4954	328.105
0.050	5.3341	11.4789	326.605
0.075	5.3245	11.4607	324.914

Table 2.4 : Lattice parameters and unit cell volume of $CaGd_{1-x}NbWO_8:xDy^{3+}$ ($x = 0.020, 0.025, 0.030, 0.035, 0.050, 0.075$) samples.

x	Lattice Parameters		Unit Cell Volume
	a = b (Å)	c (Å)	(Å) ³
0.020	5.2441	11.5211	316.837
0.025	5.2437	11.5177	316.695
0.030	5.2425	11.5129	316.418
0.035	5.2412	11.5081	316.047
0.050	5.2407	11.4976	315.781
0.075	5.2404	11.4963	315.709

The lattice volume was found to decrease from $330.016 \times 10^{-3} \text{ (nm)}^3$ to $324.914 \times 10^{-3} \text{ (nm)}^3$ for the $CaLa_{1-x}NbWO_8: xDy^{3+}$ samples and from $316.837 \times 10^{-3} \text{ (nm)}^3$ to $315.709 \times 10^{-3} \text{ (nm)}^3$ for the $CaGd_{1-x}NbWO_8: xDy^{3+}$ samples with the increase in the Dy^{3+} concentration varying between 0.02 and 0.075 indicating the incorporation of Dy^{3+} ions into the lattice. Lattice parameters and unit cell volumes of Dy^{3+} doped $CaLa_{1-x}NbWO_8$ and Dy^{3+} doped $CaGd_{1-x}NbWO_8$ samples are listed in Table 2.3 and Table 2.4 respectively.

2.3.2. Morphological Studies

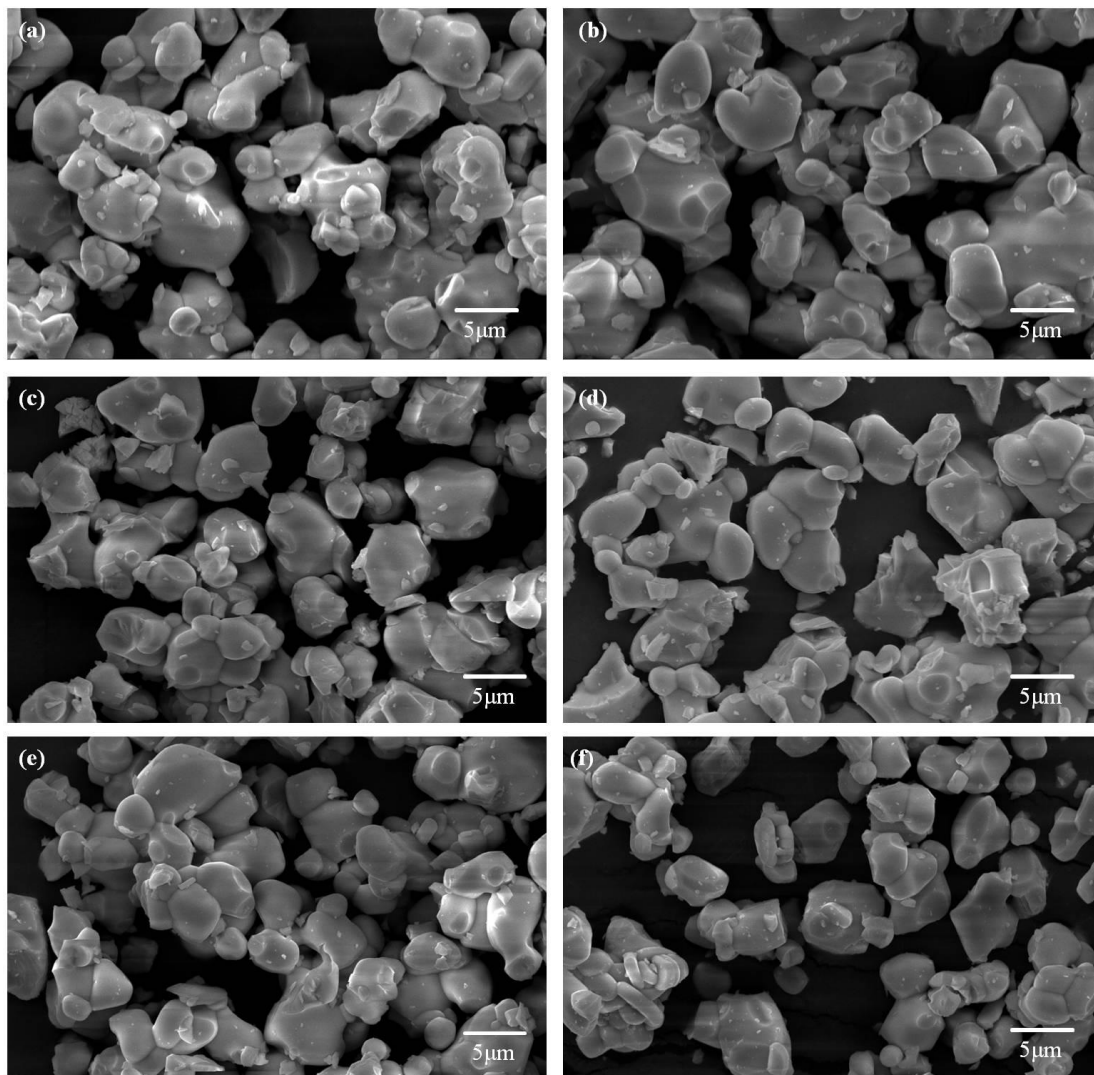


Figure 2.5 : Scanning electron micrographs of $CaLa_{1-x}NbMoO_8:xDy^{3+}$ phosphor powders with varying Dy^{3+} concentrations: (a) $x = 0.020$, (b) $x = 0.025$, (c) $x = 0.030$, (d) $x = 0.035$, (e) $x = 0.050$, and (f) $x = 0.075$.

Scanning electron micrographs of the samples were recorded and the morphology of all the Dy^{3+} doped samples are given in Figure 2.5. The particles were slightly agglomerated and were homogeneous with an average particle size of about 2 — 5 μm .

2.3.3. Optical and Photoluminescence Studies

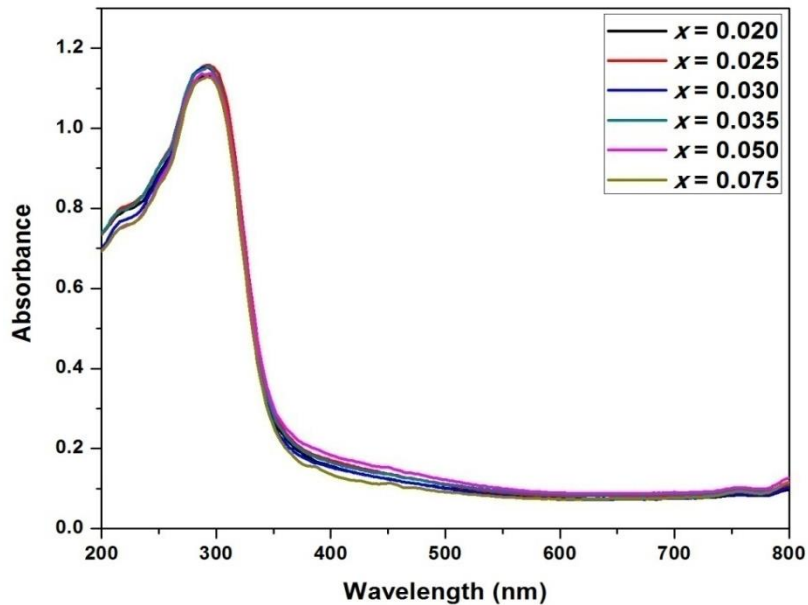


Figure 2.6 : UV-Visible absorption spectra of $CaLa_{1-x}NbMoO_8: xDy^{3+}$ phosphor powders ($x= 0.020, 0.025, 0.030, 0.035, 0.050, 0.075$).

The UV-Visible absorption spectra of Dy^{3+} doped $CaLaNbMoO_8$ is shown in Figure 2.6. The absorption spectra of $CaLaNbMoO_8$ exhibits a strong absorption band around 290 nm in the UV region which arises due to the ligand to metal charge transfer (LMCT) transitions of MoO_4/NbO_4 and $O^{2-} - Dy^{3+}$ groups in the host lattice. All the samples show a strong absorption edge around 366 nm. It is expected that these phosphors are excitable under both near UV and blue irradiation, which is one of the prerequisites for a phosphor material for pc WLEDs.

Photoluminescence excitation spectra of the $CaLa_{1-x}NbMoO_8: xDy^{3+}$ ($x= 0.020, 0.025, 0.030, 0.035, 0.050, 0.075$) samples were recorded and the spectrum profiles of the samples for an emission at 487 nm and 575 nm are given in Figure 2.7 and Figure 2.8 respectively.

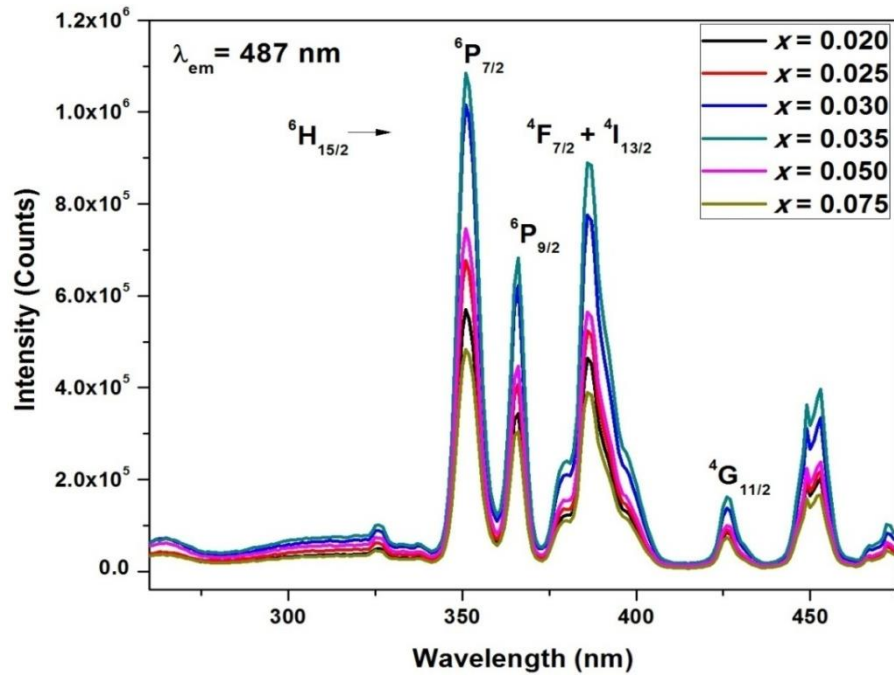


Figure 2.7 : Excitation spectra of $\text{CaLa}_{1-x}\text{NbMoO}_8:x\text{Dy}^{3+}$ ($x = 0.020, 0.025, 0.030, 0.035, 0.050, 0.075$) for an emission at 487 nm.

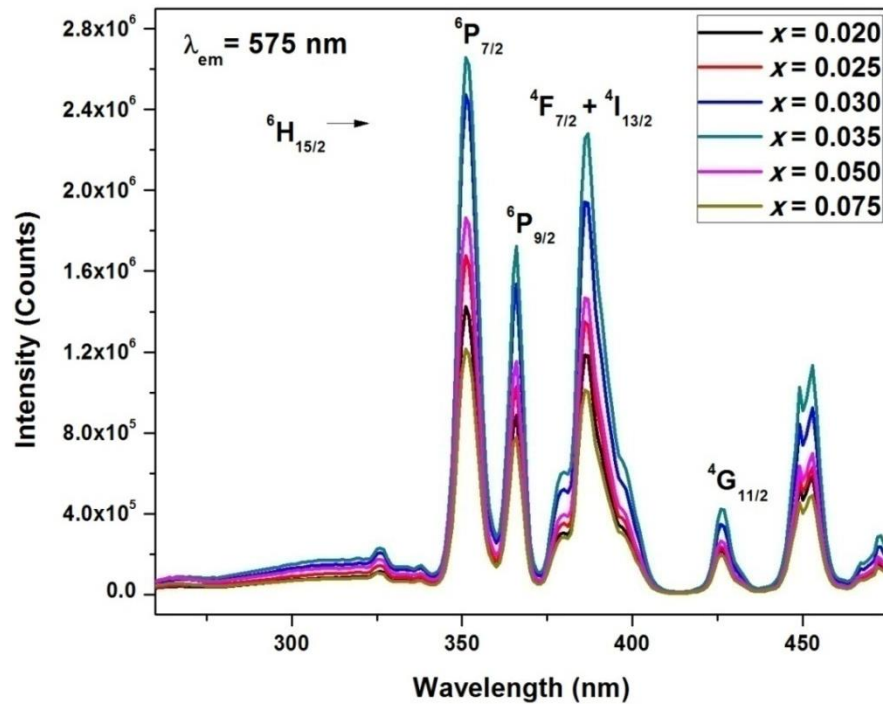


Figure 2.8 : Excitation spectra of $\text{CaLa}_{1-x}\text{NbMoO}_8:x\text{Dy}^{3+}$ ($x = 0.020, 0.025, 0.030, 0.035, 0.050, 0.075$) for an emission at 575 nm.

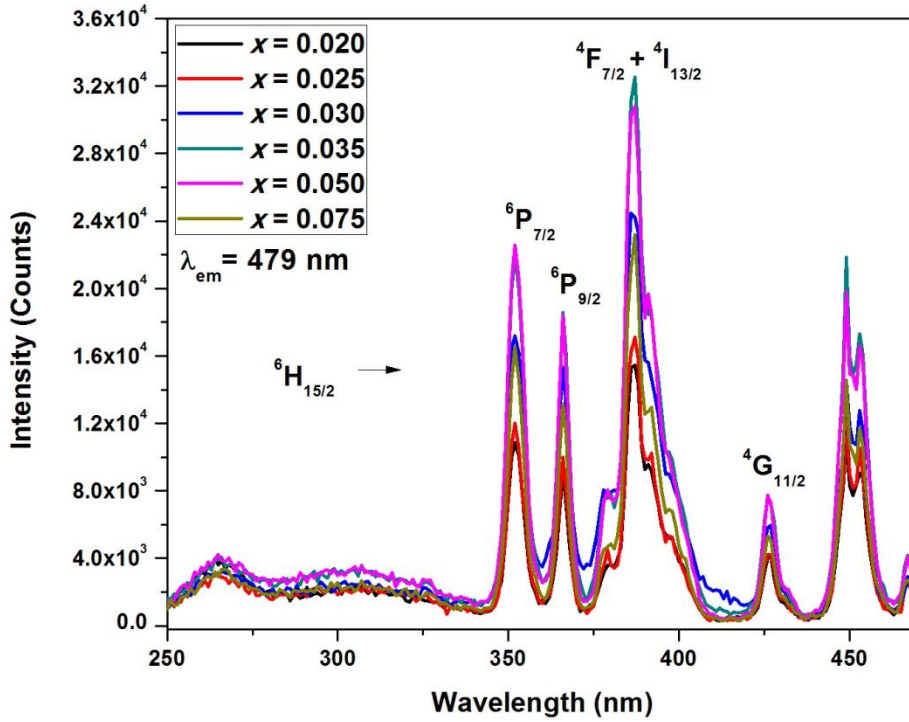


Figure 2.9 : Excitation spectra of $\text{CaGd}_{1-x}\text{NbMoO}_8:x\text{Dy}^{3+}$ ($x = 0.020, 0.025, 0.030, 0.035, 0.050, 0.075$) for an emission at 479 nm.

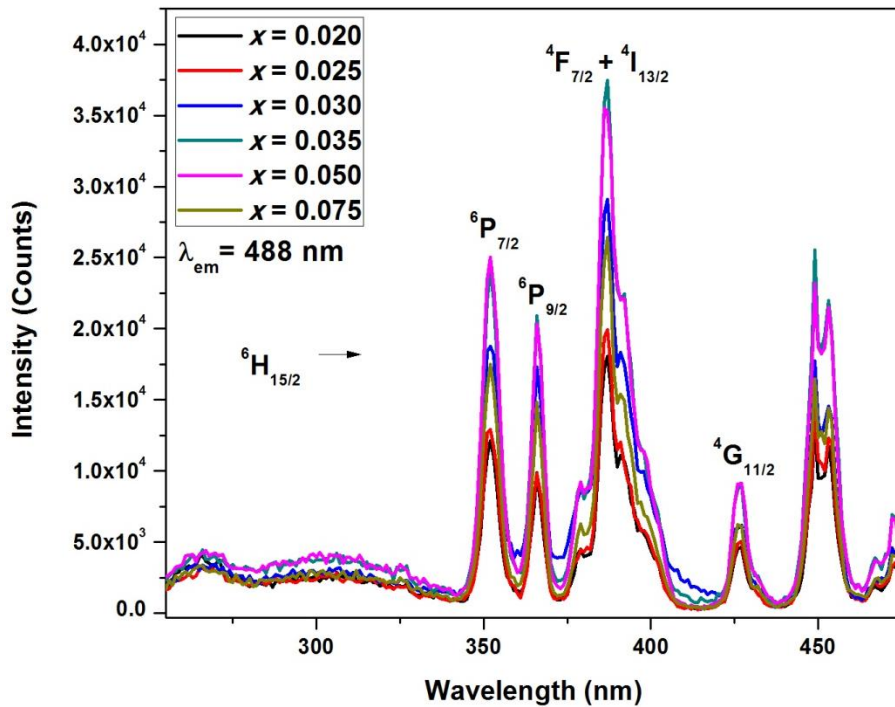


Figure 2.10 : Excitation spectra of $\text{CaGd}_{1-x}\text{NbMoO}_8:x\text{Dy}^{3+}$ ($x = 0.020, 0.025, 0.030, 0.035, 0.050, 0.075$) for an emission at 488 nm.

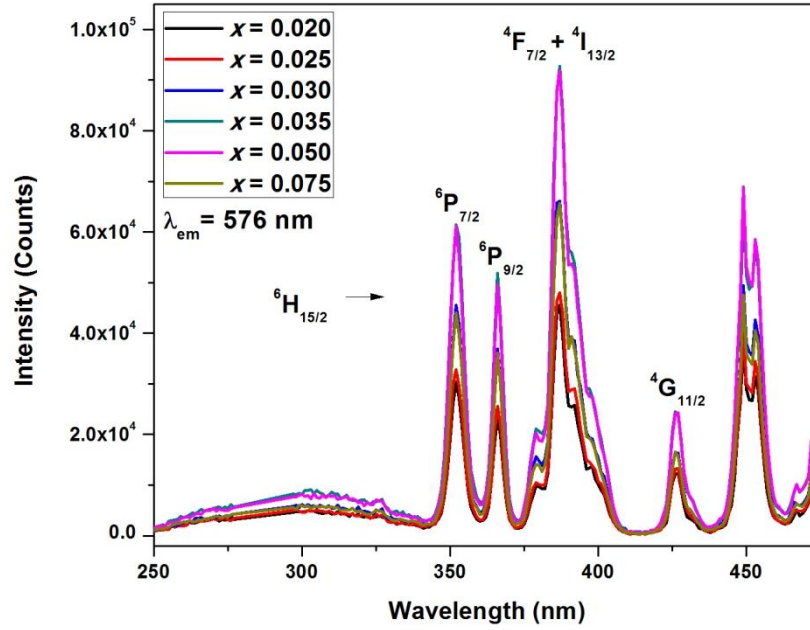


Figure 2.11 : Excitation spectra of CaGd_{1-x}NbMoO₈:xDy³⁺ ($x = 0.020, 0.025, 0.030, 0.035, 0.050, 0.075$) for an emission at 576 nm.

Photoluminescence excitation spectra of the CaGd_{1-x}NbMoO₈: xDy³⁺ ($x = 0.020, 0.025, 0.030, 0.035, 0.050, 0.075$) samples were recorded and the spectrum profiles of the samples for an emission at 479nm, 488 nm and 576 nm are given in Figure 2.9, Figure 2.10 and Figure 2.11 respectively. The excitation spectra consists of a broad and weak O²⁻ - Dy³⁺ charge transfer band and a series of sharp and intense f-f transition peaks of Dy³⁺. The sharp peaks beyond 350 nm due to the intra-configurational f-f transitions of Dy³⁺ peaks at 351/352 nm (⁶H_{15/2} → ⁶P_{7/2}), 366 nm (⁶H_{15/2} → ⁶P_{9/2}), 386/387 nm (⁶H_{15/2} → ⁴F_{7/2} + ⁴I_{13/2}) and 426 nm (⁶H_{15/2} → ⁴G_{11/2}). The sharp and intense excitation peaks in the UV region matches well to the outputs of the UV led chips making it a potential candidate in the application point of view. In general, the energy of the charge transfer state and 4f⁸5d¹ level is relatively large so that direct excitation with ultraviolet radiation of Dy³⁺ activated phosphors is not very effective. However, the energy transfer resulting from the excitation via host complex ions could be effective. [Yen *et al.* 2007] It is observed that the absorption peaks of the intra-configurational 4f transitions of Dy³⁺ increases with increasing concentration of dysprosium. The enhancement in the emission of Dy³⁺ is mainly due to the increased absorption of ⁶H_{15/2} → ⁶P_{7/2}, ⁶H_{15/2} → ⁶P_{9/2} and ⁶H_{15/2} → ⁴F_{7/2} + ⁴I_{13/2} transitions.

Photoluminescence emission spectra of $CaLa_{1-x}NbMoO_8:xDy^{3+}$ ($x = 0.020, 0.025, 0.030, 0.035, 0.050, 0.075$) samples under an excitation of 351 nm, 366 nm and 386 nm are given in Figure 2.12, Figure 2.13 and Figure 2.14 respectively.

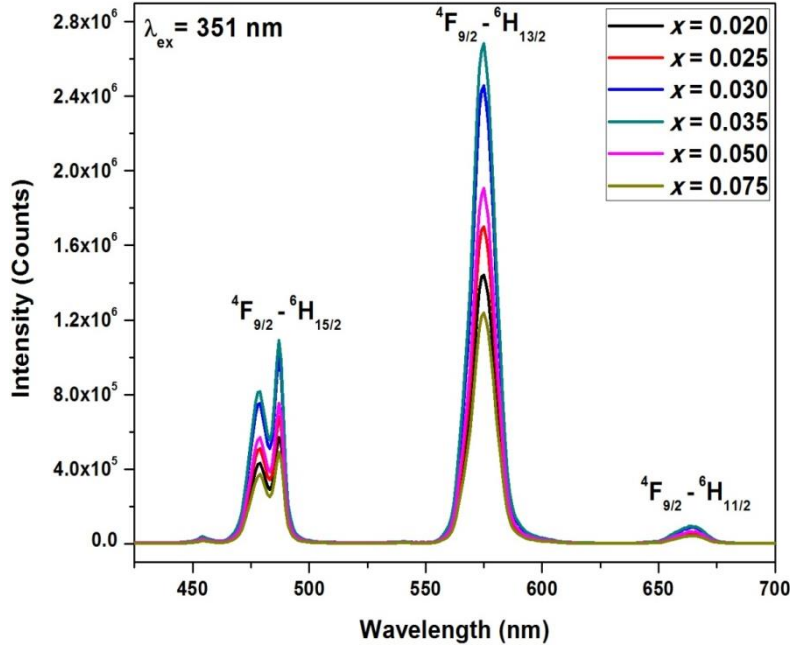


Figure 2.12 : Emission spectra of $CaLa_{1-x}NbMoO_8:xDy^{3+}$ ($x = 0.020, 0.025, 0.030, 0.035, 0.050, 0.075$) under 351 nm excitation.

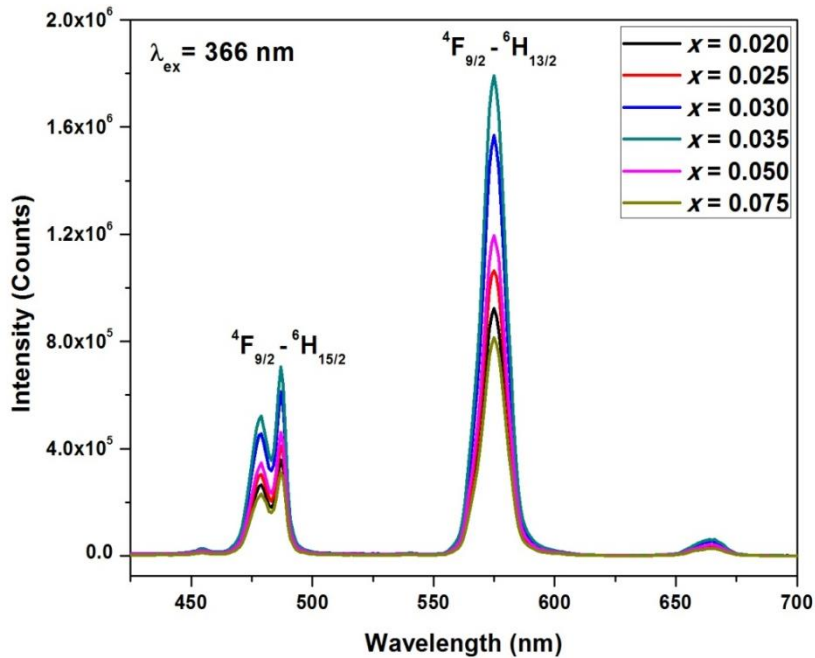


Figure 2.13 : Emission spectra of $CaLa_{1-x}NbMoO_8:xDy^{3+}$ ($x = 0.020, 0.025, 0.030, 0.035, 0.050, 0.075$) under 366 nm excitation.

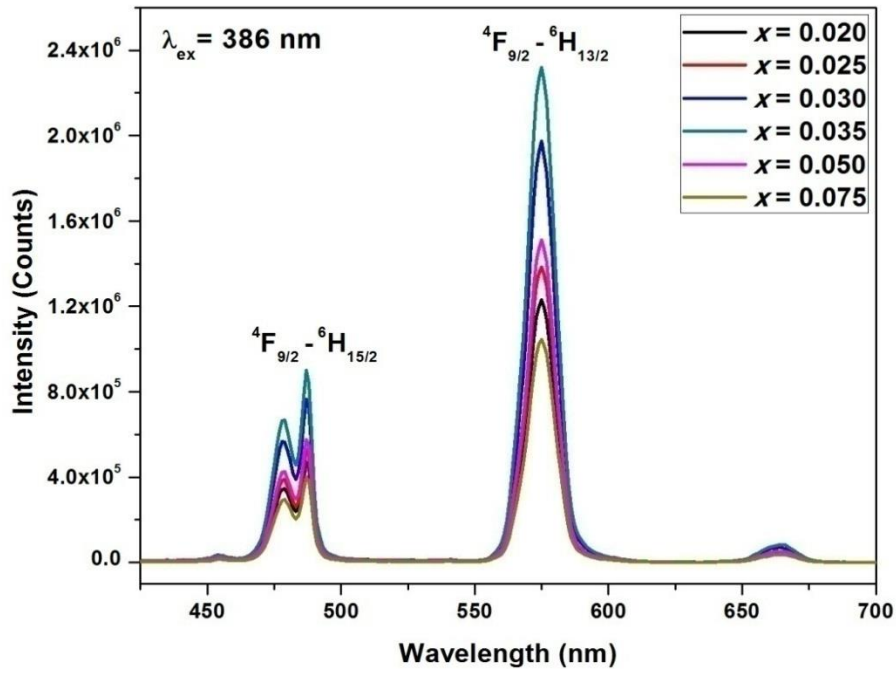


Figure 2.14 : Emission spectra of $CaLa_{1-x}NbMoO_8:xDy^{3+}$ ($x = 0.020, 0.025, 0.030, 0.035, 0.050, 0.075$) under 386 nm excitation.

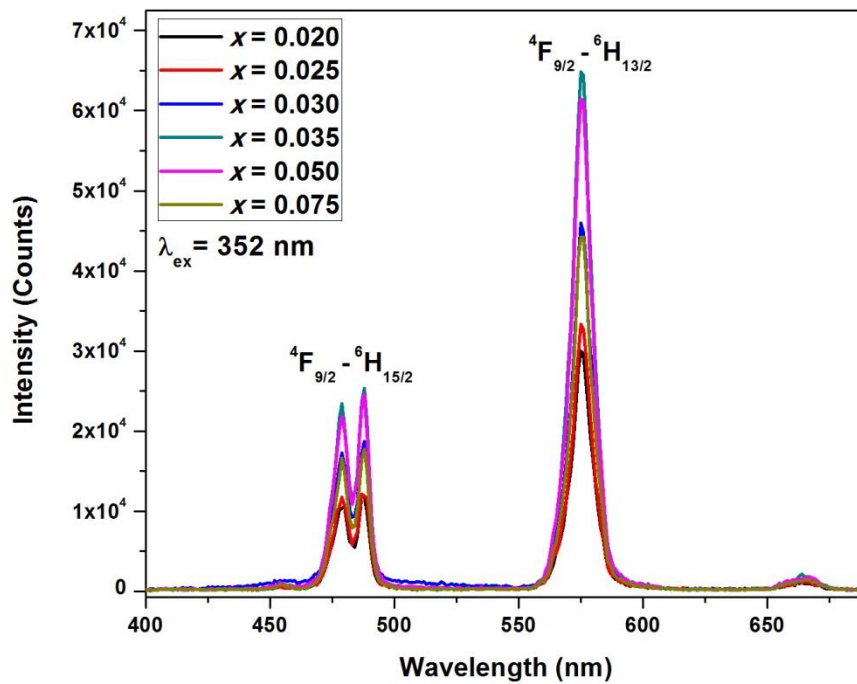


Figure 2.15 : Emission spectra of $CaGd_{1-x}NbMoO_8:xDy^{3+}$ ($x = 0.020, 0.025, 0.030, 0.035, 0.050, 0.075$) under 352 nm excitation.

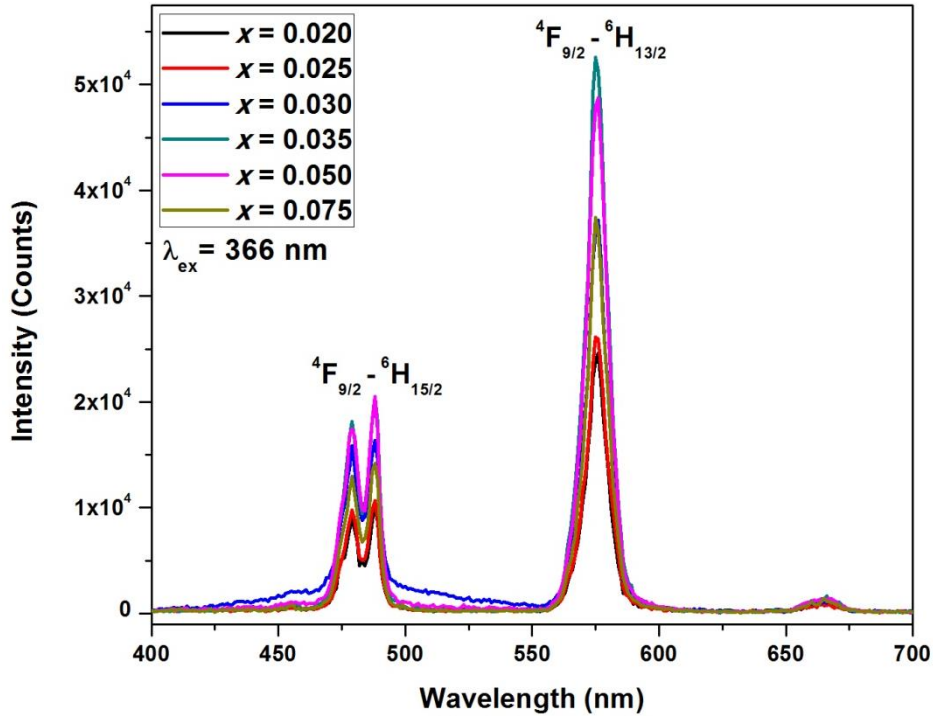


Figure 2.16 : Emission spectra of $\text{CaGd}_{1-x}\text{NbMoO}_8:x\text{Dy}^{3+}$ ($x = 0.020, 0.025, 0.030, 0.035, 0.050, 0.075$) under 366 nm excitation.

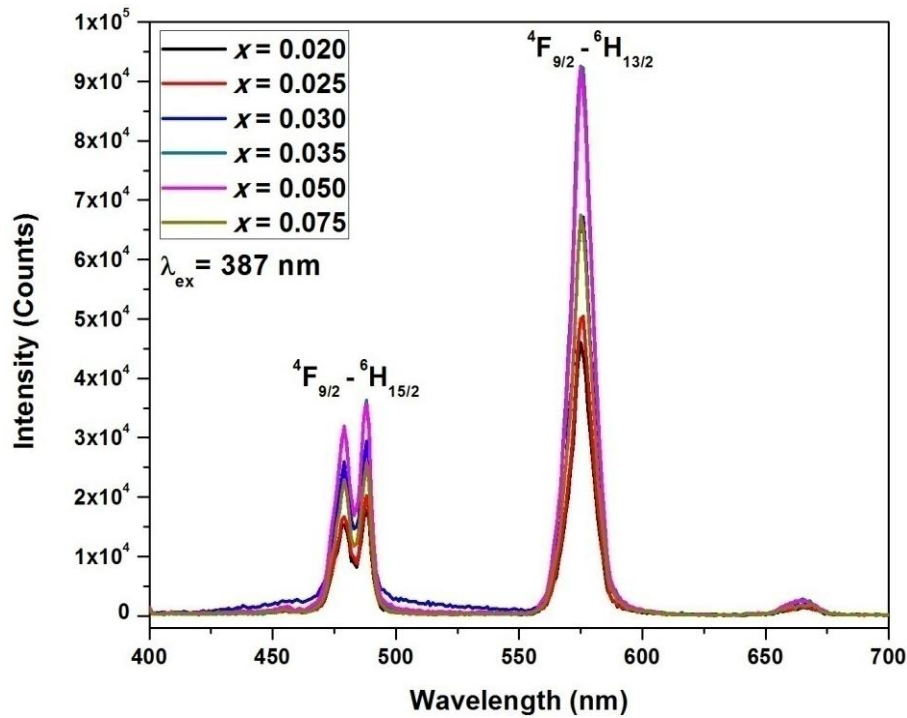


Figure 2.17 : Emission spectra of $\text{CaGd}_{1-x}\text{NbMoO}_8:x\text{Dy}^{3+}$ ($x = 0.020, 0.025, 0.030, 0.035, 0.050, 0.075$) under 387 nm excitation.

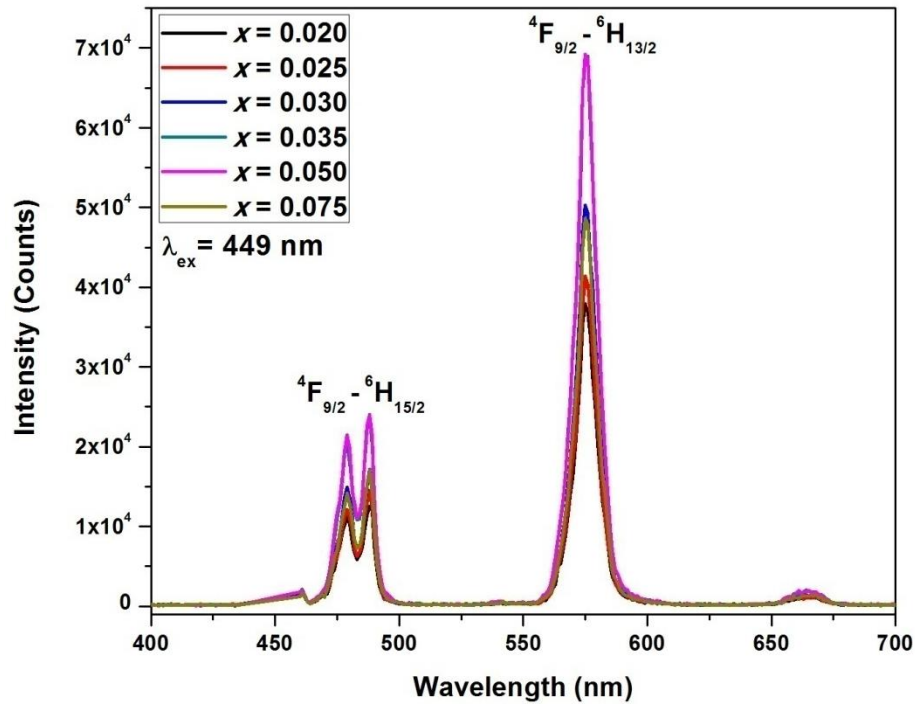


Figure 2.18 : Emission spectra of $\text{CaGd}_{1-x}\text{NbMoO}_8:x\text{Dy}^{3+}$ ($x = 0.020, 0.025, 0.030, 0.035, 0.050, 0.075$) under 449 nm excitation.

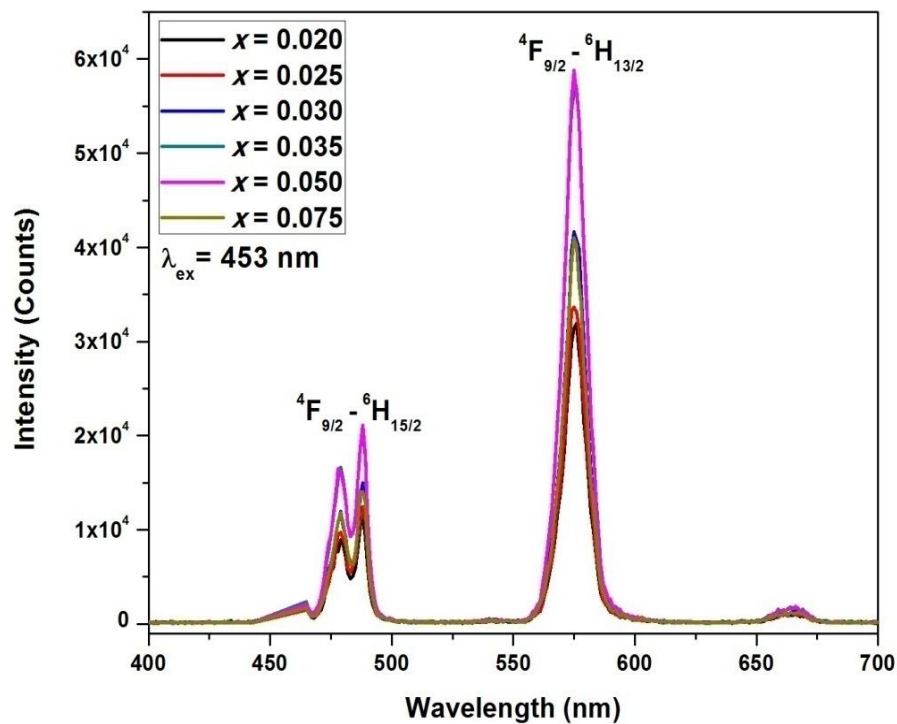


Figure 2.19 : Emission spectra of $\text{CaGd}_{1-x}\text{NbMoO}_8:x\text{Dy}^{3+}$ ($x = 0.020, 0.025, 0.030, 0.035, 0.050, 0.075$) under 453 nm excitation.

Photoluminescence emission spectra of $CaGd_{1-x}NbMoO_8:xDy^{3+}$ ($x = 0.020, 0.025, 0.030, 0.035, 0.050, 0.075$) samples under an excitation of 352 nm, 366 nm, 387 nm, 449 nm and 453 nm are given in Figure 2.15, Figure 2.16, Figure 2.17, Figure 2.18 and Figure 2.19 respectively. The luminescence emission properties have been carefully investigated upon 351 nm, 366 nm, and 386 nm excitations for the $CaLa_{1-x}NbMoO_8:xDy^{3+}$ samples and upon 352 nm, 366 nm, 387 nm, 449 nm and 453 nm excitations for the $CaGd_{1-x}NbMoO_8:xDy^{3+}$ samples. Upon all excitations the phosphor samples exhibited sharp peaks in the visible regions at 479 nm, 487/488 nm and 575/576 nm which are attributed to the magnetic dipole transition of ${}^4F_{9/2} \rightarrow {}^6H_{15/2}$ and the forced electric dipole transition of ${}^4F_{9/2} \rightarrow {}^6H_{13/2}$ respectively. A feeble red emission at 664 nm due to the ${}^4F_{9/2} \rightarrow {}^6H_{11/2}$ transition is also observed. When Dy^{3+} is situated at a site with low symmetry and without an inversion center, the yellow emission is dominant and the blue emission is stronger when Dy^{3+} ions occupies a site with high symmetry and with an inversion center. [Jena *et al.* 2015] The yellow emission is dominant in all the samples indicating that the local environment around Dy^{3+} ions lacks inversion symmetry. The blue and the yellow emissions combine together to give white light. Figure 2.20 shows the variation in the luminescent intensities with Dy^{3+} doping concentrations under 351 nm, 366 nm and 386 nm excitations for the emissions at 487 nm and 575 nm for the $CaLa_{1-x}NbMoO_8:xDy^{3+}$ samples.

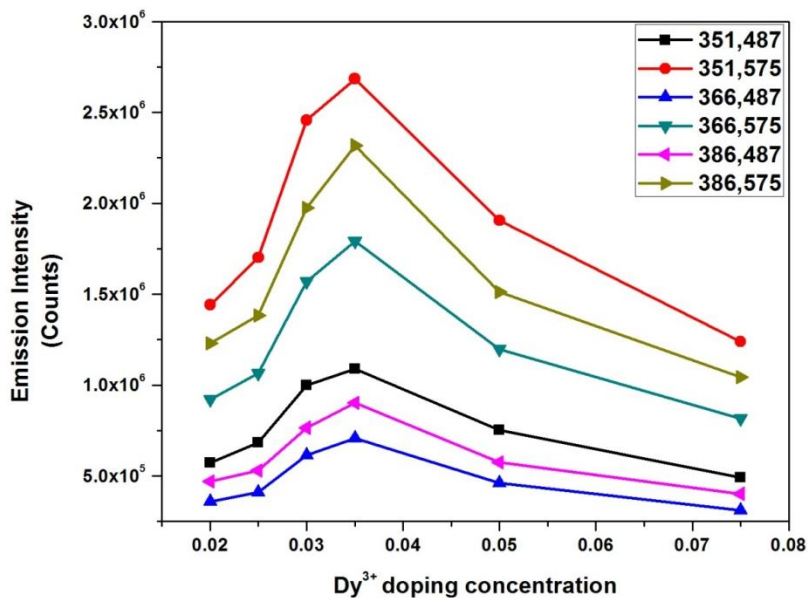


Figure 2.20 : Variation in the luminescent intensities with Dy^{3+} doping concentrations for the $CaLa_{1-x}NbMoO_8:xDy^{3+}$ samples.

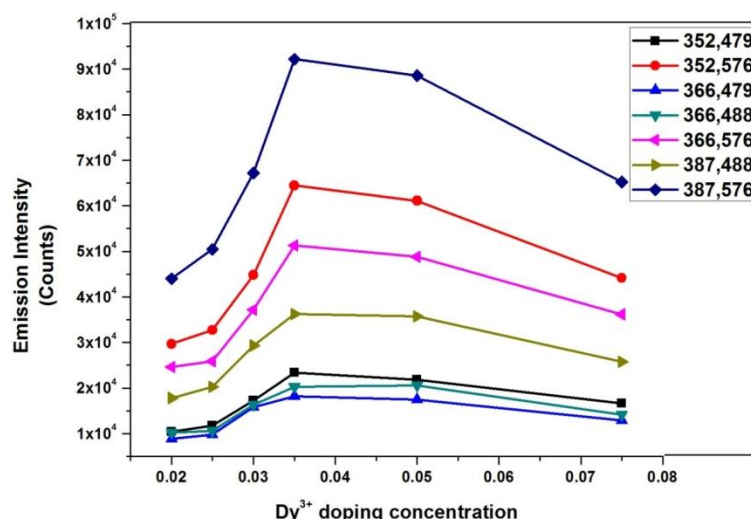


Figure 2.21 : Variation in the luminescent intensities with Dy^{3+} doping concentrations for the $CaGd_{1-x}NbMoO_8:xDy^{3+}$ samples.

The variation in the luminescent intensities with Dy^{3+} doping concentrations under 352 nm, 366 nm and 387 nm excitations for the selected emissions at 479 nm, 488 nm and 576 nm for the $CaGd_{1-x}NbMoO_8:xDy^{3+}$ samples are given in Figure 2.21. It is also observed that the emission intensities of all the samples are enhanced significantly with the increase in the concentration of the Dy^{3+} ions reaching a maximum at $x = 0.035$ and then decreases with further increase in Dy^{3+} concentration. Lower doping concentrations of the activator ions leads to weak luminescence and the higher doping concentration causes quenching of luminescence. This is termed as concentration quenching. The quenching of intensities is due to the increase of non-radiative energy transfer through cross-relaxation (${}^4F_{9/2} \rightarrow {}^6H_{9/2} + {}^6F_{11/2}$ and ${}^6H_{15/2} \rightarrow {}^6F_{13/2}$ transitions) and resonant energy levels where non-radiative losses occur due to the interaction between two Dy^{3+} ions. For the excitation wavelengths, the Dy^{3+} ion luminesces from ${}^4I_{13/2}$ level, quickly relax non-radiatively and populate the ${}^4F_{9/2}$ level, from where the radiative emission takes place to the lower energy levels. [Blasse G 1979] When Dy^{3+} is substituted for La^{3+} with the same valency in the phosphor host $CaLaNbMoO_8$, the Y/B ratio does not vary much with the variation in the concentration of Dy^{3+} . The CIE color coordinates values and Y/B ratios for $CaLa_{1-x}NbMoO_8:xDy^{3+}$ ($x = 0.020, 0.025, 0.030, 0.035, 0.050, 0.075$) samples excited at 351 nm and 366 nm are listed in Table 2.5 and Table 2.6 respectively. The CIE color coordinates of all the samples lies within the range of the standard chromaticity coordinates of white light.

Table 2.5 : CIE color coordinate values and Y/B ratios of $CaLa_{1-x}NbMoO_8: xDy^{3+}$ ($x = 0.020, 0.025, 0.030, 0.035, 0.050, 0.075$) samples. under 351 nm excitation.

x	Color Co-ordinates (x, y)	Y/B ratio
0.02	(0.392,0.424)	2.527
0.025	(0.393,0.425)	2.496
0.03	(0.391,0.422)	2.462
0.035	(0.391,0.422)	2.464
0.05	(0.392,0.424)	2.530
0.075	(0.393,0.425)	2.519

Table 2.6 : CIE color coordinate values and Y/B ratios of $CaLa_{1-x}NbMoO_8: xDy^{3+}$ ($x = 0.020, 0.025, 0.030, 0.035, 0.050, 0.075$) samples. under 366 nm excitation.

x	Color Co-ordinates (x, y)	Y/B ratio
0.02	(0.389, 0.421)	2.572
0.025	(0.393, 0.425)	2.594
0.03	(0.389, 0.421)	2.558
0.035	(0.389,0.422)	2.539
0.05	(0.391, 0.423)	2.597
0.075	(0.392, 0.424)	2.627

The photoluminescence decay curves of $CaLa_{1-x}NbMoO_8: xDy^{3+}$ ($x = 0.02, 0.025, 0.03, 0.035, 0.05, 0.075$) are shown in Figure 2.22. The curve gives the decay of $Dy^{3+} {}^4F_{9/2} \rightarrow {}^6H_{13/2}$ transition under 351 nm excitation. The curve can be fitted using the single exponential decay function,

$$y = y_0 + Ae^{(-x/t)}$$

where y_0 and A are constants and t is the decay time. The lifetimes of $\text{CaLa}_{1-x}\text{NbMoO}_8: x\text{Dy}^{3+}$ ($x = 0.02, 0.025, 0.03, 0.035, 0.05, 0.075$) ${}^4\text{F}_{9/2} \rightarrow {}^6\text{H}_{13/2}$ transition are obtained as 0.208, 0.200, 0.195, 0.191, 0.171 and 0.152 ms respectively. The decay curves of the $\text{CaGd}_{1-x}\text{NbMoO}_8: x\text{Dy}^{3+}$ ($x = 0.02, 0.025, 0.03, 0.035, 0.05, 0.075$) samples were not recorded since the emission intensities of the $\text{CaLa}_{1-x}\text{NbMoO}_8: x\text{Dy}^{3+}$ samples are much higher when compared with the $\text{CaGd}_{1-x}\text{NbMoO}_8: x\text{Dy}^{3+}$ phosphor samples.

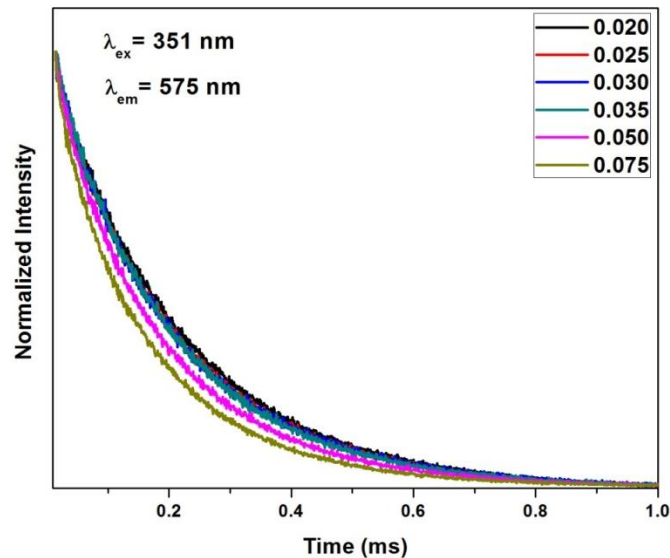


Figure 2.22 : Decay curves of $\text{CaLa}_{1-x}\text{NbMoO}_8: x\text{Dy}^{3+}$ ($x = 0.02, 0.025, 0.03, 0.035, 0.05, 0.075$) under an excitation of 351nm monitoring the emission at 575 nm.

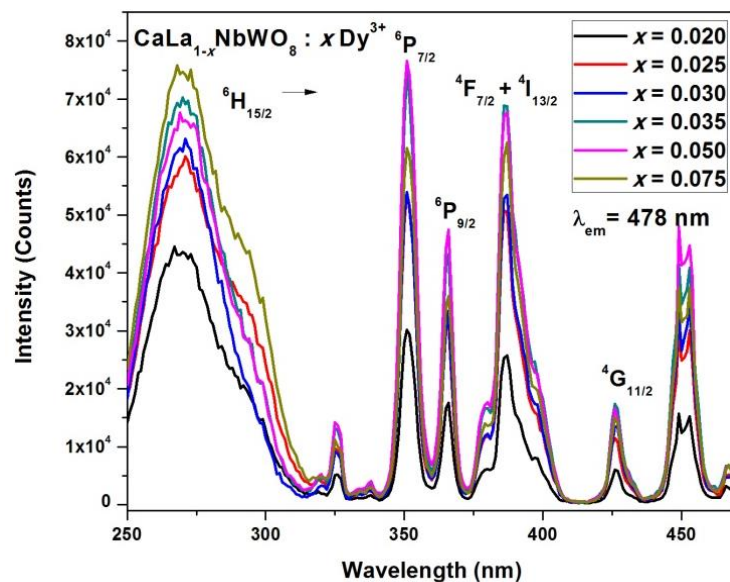


Figure 2.23 : Excitation spectra of $\text{CaLa}_{1-x}\text{NbWO}_8: x\text{Dy}^{3+}$ ($x = 0.020, 0.025, 0.030, 0.035, 0.050, 0.075$) for an emission at 478 nm.

Photoluminescence excitation spectra of the $\text{CaLa}_{1-x}\text{NbWO}_8: x\text{Dy}^{3+}$ ($x = 0.020, 0.025, 0.030, 0.035, 0.050, 0.075$) samples for an emission at 478 nm, 487 nm and 575 nm are given in Figure 2.23, Figure 2.24 and Figure 2.25 respectively.

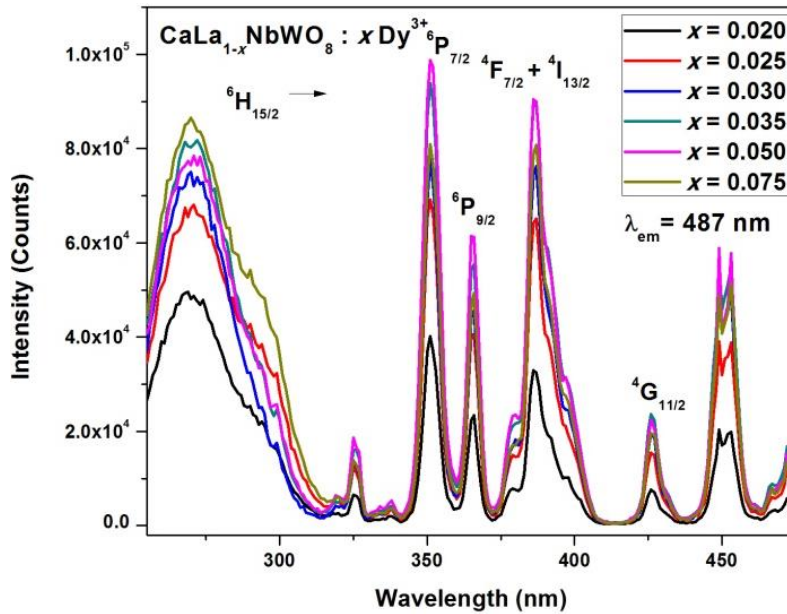


Figure 2.24 : Excitation spectra of $\text{CaLa}_{1-x}\text{NbWO}_8:x\text{Dy}^{3+}$ ($x = 0.020, 0.025, 0.030, 0.035, 0.050, 0.075$) for an emission at 487 nm.

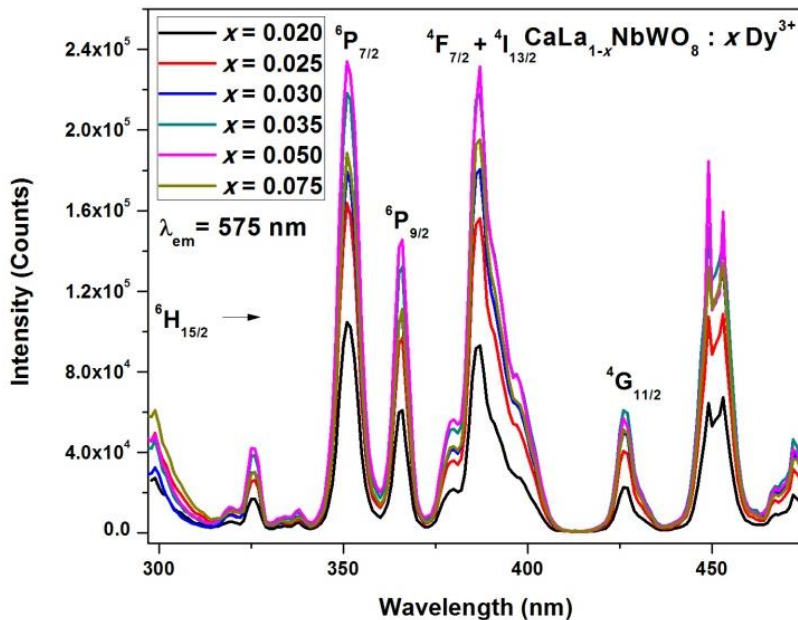


Figure 2.25 : Excitation spectra of $\text{CaLa}_{1-x}\text{NbWO}_8:x\text{Dy}^{3+}$ ($x = 0.020, 0.025, 0.030, 0.035, 0.050, 0.075$) for an emission at 575 nm.

Photoluminescence excitation spectra of the $CaGd_{1-x}NbWO_8:xDy^{3+}$ ($x= 0.020, 0.025, 0.030, 0.035, 0.050, 0.075$) samples for an emission at 479 nm, 488 nm and 575 nm are given in Figure 2.26, Figure 2.27 and Figure 2.28 respectively.

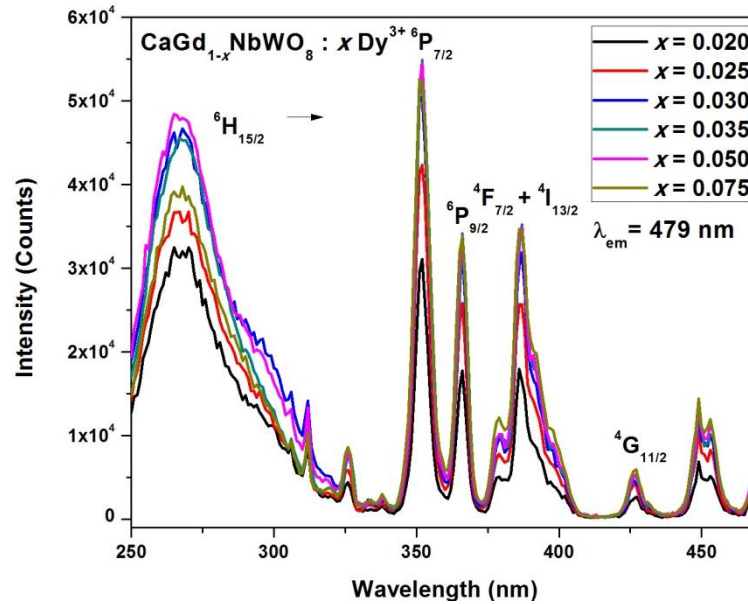


Figure 2.26 : Excitation spectra of $CaGd_{1-x}NbWO_8:xDy^{3+}$ ($x = 0.020, 0.025, 0.030, 0.035, 0.050, 0.075$) for an emission at 479 nm.

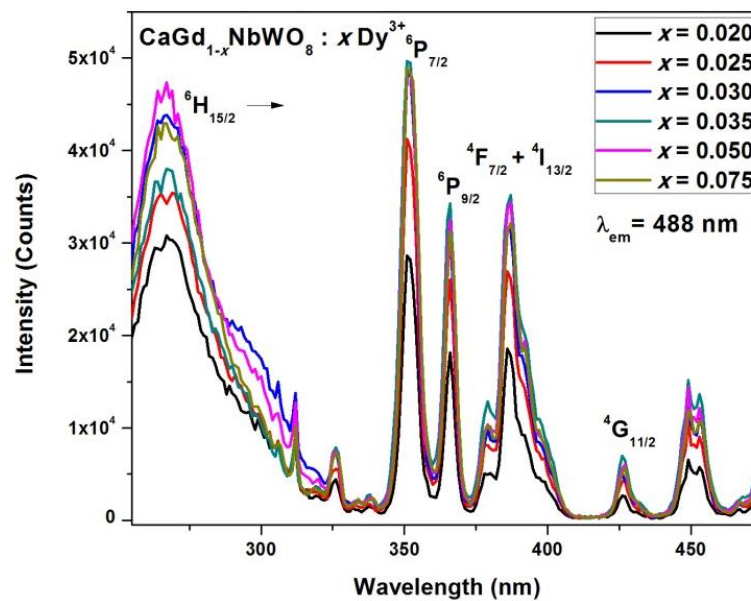


Figure 2.27 : Excitation spectra of $CaGd_{1-x}NbWO_8:xDy^{3+}$ ($x = 0.020, 0.025, 0.030, 0.035, 0.050, 0.075$) for an emission at 488 nm.

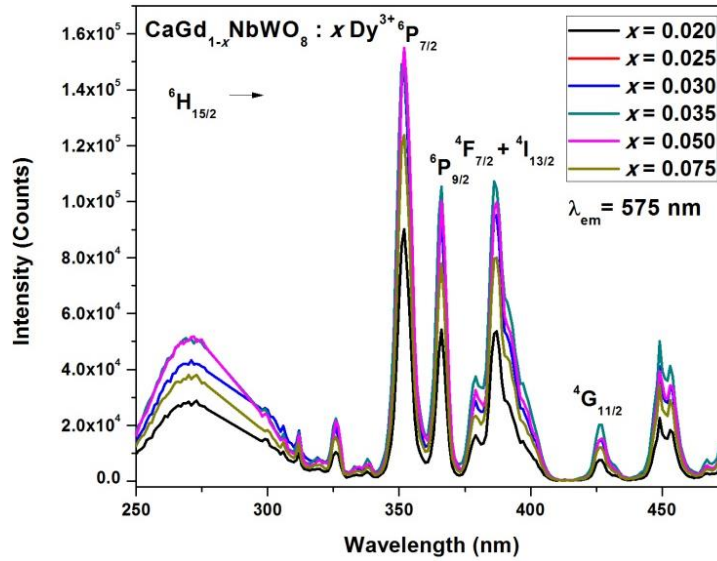


Figure 2.28 : Excitation spectra of $CaGd_{1-x}NbWO_8:xDy^{3+}$ ($x = 0.020, 0.025, 0.030, 0.035, 0.050, 0.075$) for an emission at 575 nm.

A broad band from 250 nm to 310 nm is assigned to the charge transfer transition from the oxygen to the metal. [Yin *et al.* 2012] This broad band in the excitation spectra results from the combination of $O_{2p} \rightarrow Dy_{4f}$ and $O_{2p} \rightarrow Nb_{4d}$ CT transitions. A series of sharp and intense peaks beyond 350 nm are due to the intra-configurational f-f transitions of Dy^{3+} at 351/352 nm (${}^6H_{15/2} \rightarrow {}^6P_{7/2}$), 366 nm (${}^6H_{15/2} \rightarrow {}^6P_{9/2}$), 387 nm (${}^6H_{15/2} \rightarrow {}^4F_{7/2} + {}^4I_{13/2}$) and 426 nm (${}^6H_{15/2} \rightarrow {}^4G_{11/2}$). The charge transfer transitions and the intraconfigurational f-f transitions of Dy^{3+} are of comparable intensities for the blue emissions at 478/479 nm and 487/488 nm in both the tungstate samples, however the CT band is broad and weak for the emissions in the yellow wavelength region. The sharp and intense excitation peaks in the UV region matches well to the outputs of the UV led chips making it a potential candidate in the application point of view. It is observed that the absorption peaks of the intra-configurational 4f transitions of Dy^{3+} increases with increasing concentration of dysprosium. The enhancement in the emission of Dy^{3+} is mainly due to the increased absorption of ${}^6H_{15/2} \rightarrow {}^6P_{7/2}$, ${}^6H_{15/2} \rightarrow {}^6P_{9/2}$ and ${}^6H_{15/2} \rightarrow {}^4F_{7/2} + {}^4I_{13/2}$ transitions. The $CaLa_{1-x}NbMoO_8:xDy^{3+}$ phosphor samples showed much better luminescence properties when compared with the $CaGd_{1-x}NbMoO_8:xDy^{3+}$ phosphor samples. The charge transfer band is almost flat in the molybdate samples, but in the case of the tungstate samples, the CT band is very strong and broad thereby transferring the energy to enhance the characteristic lines of the Dy^{3+} ion.

Photoluminescence emission spectra of $\text{CaLa}_{1-x}\text{NbWO}_8:x\text{Dy}^{3+}$ ($x = 0.020, 0.025, 0.030, 0.035, 0.050, 0.075$) samples under an excitation of 351 nm, 366 nm and 387 nm are given in Figure 2.29, Figure 2.30 and Figure 2.31 respectively.

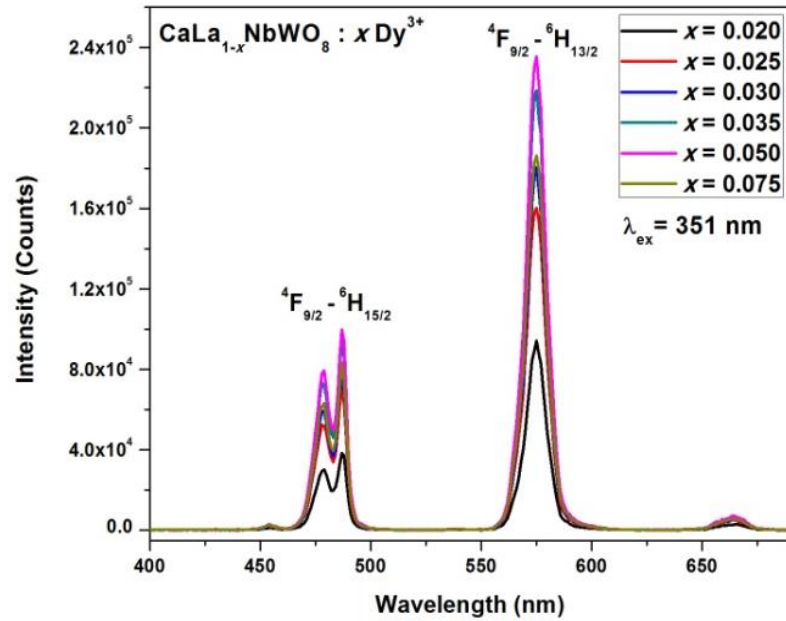


Figure 2.29 : Emission spectra of $\text{CaLa}_{1-x}\text{NbWO}_8:x\text{Dy}^{3+}$ ($x = 0.020, 0.025, 0.030, 0.035, 0.050, 0.075$) under 351 nm excitation.

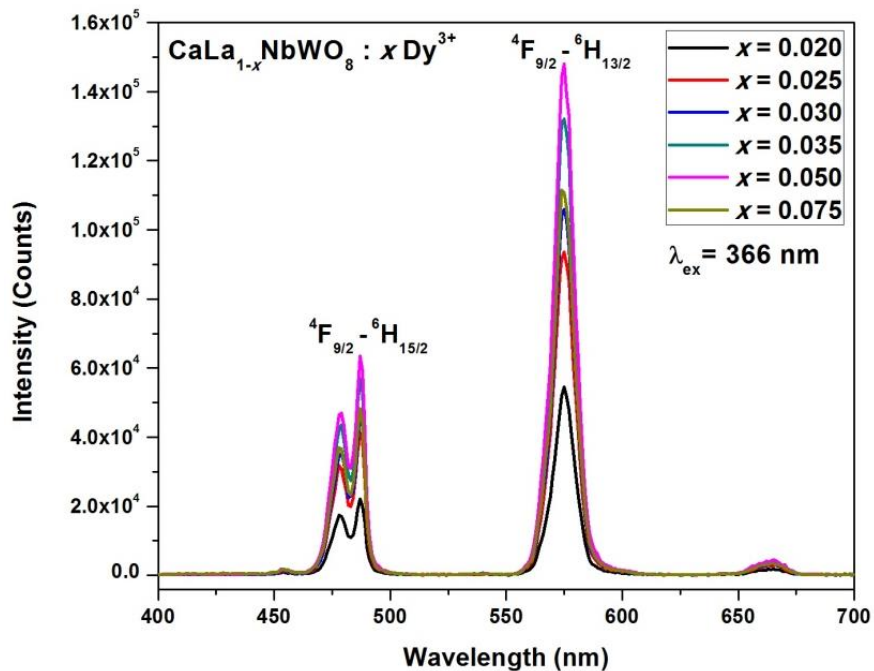


Figure 2.30 : Emission spectra of $\text{CaLa}_{1-x}\text{NbWO}_8:x\text{Dy}^{3+}$ ($x = 0.020, 0.025, 0.030, 0.035, 0.050, 0.075$) under 366 nm excitation.

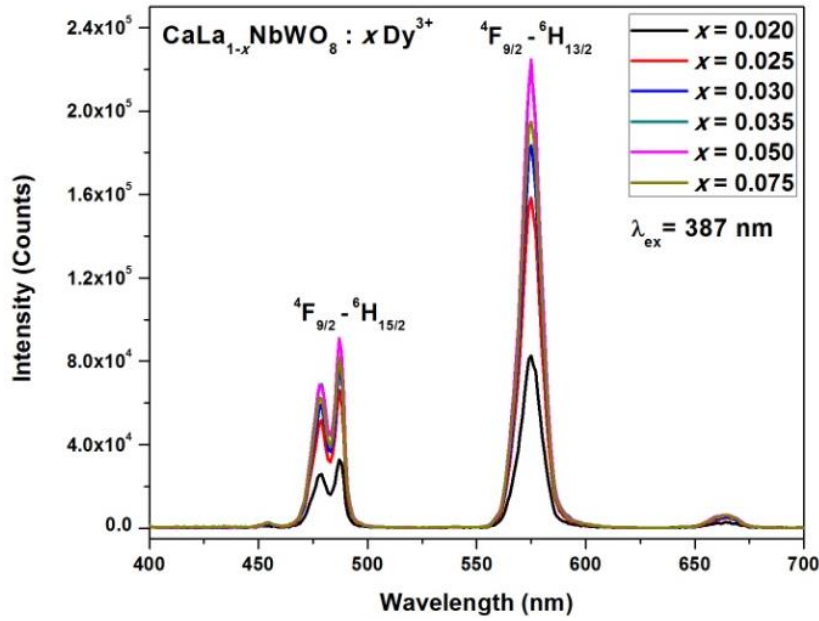


Figure 2.31 : Emission spectra of $CaLa_{1-x}NbWO_8 : xDy^{3+}$ ($x = 0.020, 0.025, 0.030, 0.035, 0.050, 0.075$) under 387 nm excitation.

Photoluminescence emission spectra of $CaGd_{1-x}NbMoO_8 : xDy^{3+}$ ($x = 0.020, 0.025, 0.030, 0.035, 0.050, 0.075$) samples under an excitation of 352 nm, 366 nm and 387 nm are given in Figure 2.32, Figure 2.33 and Figure 2.34 respectively.

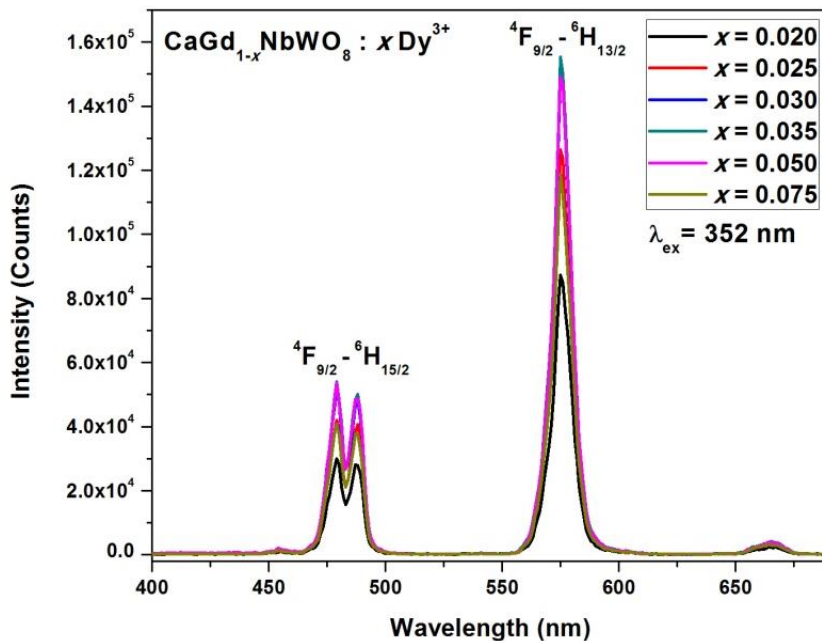


Figure 2.32 : Emission spectra of $CaGd_{1-x}NbWO_8 : xDy^{3+}$ ($x = 0.020, 0.025, 0.030, 0.035, 0.050, 0.075$) under 352 nm excitation.

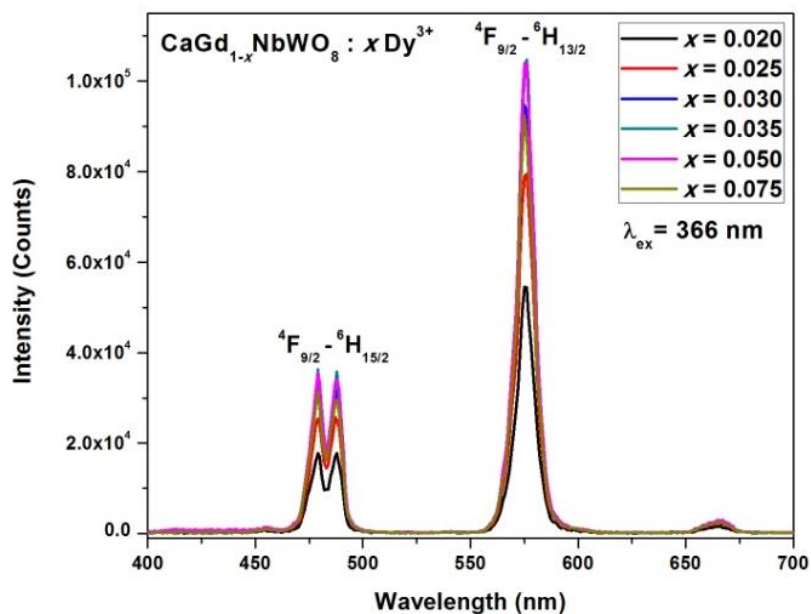


Figure 2.33 : Emission spectra of $\text{CaGd}_{1-x}\text{NbWO}_8:x\text{Dy}^{3+}$ ($x = 0.020, 0.025, 0.030, 0.035, 0.050, 0.075$) under 366 nm excitation.

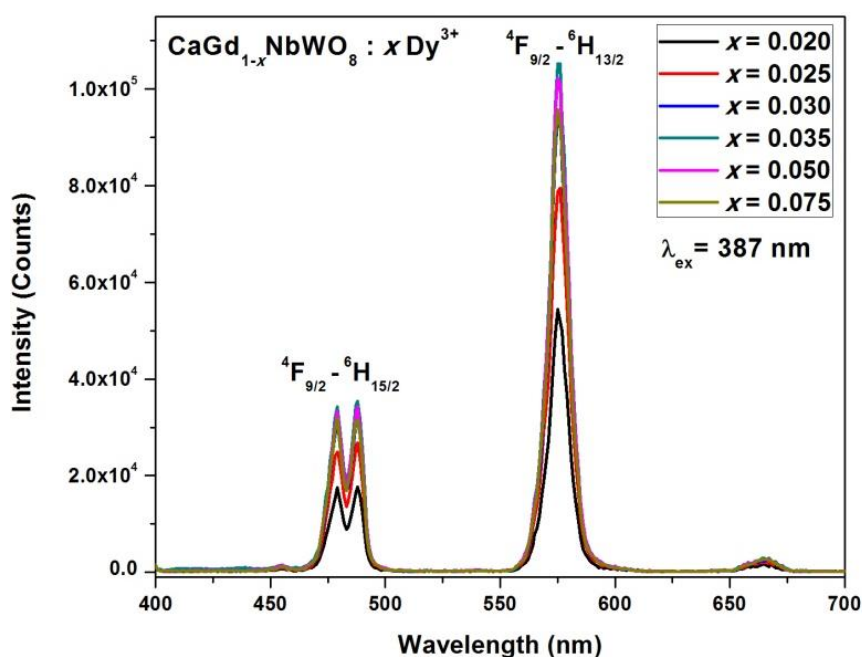


Figure 2.34 : Emission spectra of $\text{CaGd}_{1-x}\text{NbWO}_8:x\text{Dy}^{3+}$ ($x = 0.020, 0.025, 0.030, 0.035, 0.050, 0.075$) under 387 nm excitation.

The luminescence emission properties have been carefully investigated upon 351/52 nm, 366 nm, and 387 nm excitations for the $\text{Ca}(\text{La}/\text{Gd})_{1-x}\text{NbMoO}_8:x\text{Dy}^{3+}$ samples. Upon all excitations the phosphor samples exhibited sharp peaks in the visible regions at 478/479 nm, 487/488 nm and 575 nm which are attributed to the magnetic dipole

transition of ${}^4F_{9/2} \rightarrow {}^6H_{15/2}$ and the forced electric dipole transition of ${}^4F_{9/2} \rightarrow {}^6H_{13/2}$ respectively. A feeble red emission at 664 nm due to the ${}^4F_{9/2} \rightarrow {}^6H_{11/2}$ transition is also observed. The blue and the yellow emissions combine together to give white light.

The luminescence properties of Dy^{3+} activated phosphors are strongly influenced by the chemical nature of the surrounding ions and the luminescent centers. Thus, the yellow-to-blue intensity ratio (Y/B) of Dy^{3+} emission is mainly influenced by the nephelauxetic effect between Dy^{3+} and O^{2-} in the complex oxides Dy-O-M. The greater is the nephelauxetic effect, ie, greater the degree of covalency between Dy^{3+} and O^{2-} , the stronger is the yellow emission of the Dy^{3+} . Near-white-light emission can be observed in a phosphor by tuning the Y/B intensity ratio to a desired level. Reports show that the Y/B ratio of Dy^{3+} ions increases with the increase in the ionic radius of its surrounding elements. The yellow/blue intensity ratio and Commission Internationale de l'Eclairage (CIE) color coordinates of Dy^{3+} doped phosphors could be tuned by adjusting the concentration of Dy^{3+} . Therefore, Dy^{3+} doped inorganic host matrices are ideal candidates for a single phase white light emitting phosphors.

2.4. Conclusions

A series of single phase white light emitting phosphors $Ca(La/Gd)_{1-x}Nb(Mo/W)O_8: xDy^{3+}$ ($x = 0.020, 0.025, 0.030, 0.035, 0.050, 0.075$) were prepared by a conventional solid state method. The luminescence emission properties of the samples have been carefully investigated upon 351/352 nm, 366 nm, and 386 /387 nm excitation. The phosphor exhibits sharp peaks at 478/479 nm, 487/488 nm and 575/576 nm which are attributed to the magnetic dipole transition of ${}^4F_{9/2} \rightarrow {}^6H_{15/2}$ and the forced electric dipole transition of ${}^4F_{9/2} \rightarrow {}^6H_{13/2}$ respectively under all the excitation wavelengths. The yellow/blue ratio could be tuned keeping almost the color coordinates in the white light region by adjusting the concentration of Dy^{3+} . The $CaLa_{1-x}NbMoO_8:xDy^{3+}$ phosphors exhibited excellent luminescent properties in terms of the excitation and emission intensities and CIE values are closer to the NTSC values of white light and can be a potential candidate as a single phase white light emitting phosphor for WLED applications.

Chapter 3

**White light emitting stannate pyrochlore based
single phase phosphors
 $\text{CaLn}_{1-x}\text{SnNbO}_7 : x \text{Dy}^{3+}$ (Ln = La, Gd, Lu, Y)**

Parvathi S. Babu, et al.; J. Mater.Sci. :Mater. Electron. 30 (2019) 16174-16183.

Abstract

$CaLn_{0.97}SnNbO_7 : 0.03 Dy^{3+}$ ($Ln = La, Gd, Lu, Y$) and a new series of single phase pyrochlore based white phosphors, $CaLa_{1-x}SnNbO_7 : xDy^{3+}$ ($x = 0.01, 0.02, 0.03, 0.04$) and $Ca_{1-y}Sr_yLa_{0.97}SnNbO_7 : 0.03 Dy^{3+}$ ($y = 0.1, 0.2, 0.3$) were developed by a high temperature ceramic route. The phase purity and the crystalline structure of the as-prepared samples were characterised by powder X-ray diffraction method and the phosphors were found to crystallize into the cubic pyrochlore type structure. The photoluminescence properties were investigated and the results indicated that phosphors show a strong excitation levels in near UV (388 nm) and blue (452 nm) regions and emits intense complimentary blue (487 nm and 477 nm) and yellow (589 nm) light upon UV or blue excitation which can be assigned to the characteristic ${}^4F_{9/2} \rightarrow {}^6H_J$ ($J = 13/2$ and $15/2$) transitions of Dy^{3+} respectively. Thus the suitable combination of the above complimentary colors, yellow and blue is an approach to realize a full color emission and the Commission Internationale de l'Eclairage (CIE) color coordinates of the resultant phosphors lie in the white light region (0.38, 0.36) close to the standard chromacity coordinates (white light) of NTSC. The substitution of bigger ion like Sr^{2+} for Ca^{2+} enhanced significantly the photoluminescence properties by way of their excitation and emission intensities due to increased polarizability and distortion of the Dy^{3+} environment. These results demonstrate that $CaLn_{0.97}SnNbO_7 : 0.03 Dy^{3+}$ ($Ln = La, Gd, Lu, Y$), $CaLa_{1-x}SnNbO_7 : xDy^{3+}$ and $Ca_{1-y}Sr_yLa_{0.97}SnNbO_7 : 0.03 Dy^{3+}$ are promising single phased white phosphor for pc-WLED applications.

3.1 Introduction

Luminescence of lanthanide based rare earth doped phosphors with tailored engineering is gaining interest as they find many applications in the lighting technology. Phosphor materials have been extensively investigated in discovering white light emission in a single phase host system and is transforming to a highly competent field. [Narukawa *et al.* 2010] Solid State Lighting (SSL) technology through phosphor converted white light emitting diodes (pc-WLEDs), with an excellent color rendering index, tunable correlated color temperature, pure CIE chromaticity coordinates, high quantum efficiency, compactness, high luminous efficacy, environmental friendliness and energy saving are the promising next generation lighting and can surpass the drawbacks of the conventional lighting sources. [McKittrick *et al.* 2014] The commercially available pc-WLED produces white light by the combination of the complimentary colors, blue light from an InGaN chip and the yellow light from Ce^{3+} doped yttrium aluminium garnet (YAG: Ce^{3+}) phosphor. However, the blue part of the white light is greatly governed by the drive current, temperature and the amount of phosphor. At this juncture, the output from an ultraviolet (UV) light source takes up the contribution of the InGaN chip in white light generation. UV LED chip-based WLEDs have great color stability when compared with the first method as all the colors are produced by phosphors. This approach has the main drawback of low luminescence efficiency due to the re-absorption of emission colors. White light emission can be produced in a single phase host by solely doping or multi doping of activator ions with good control of the emission colors, however the luminous emission efficiency and intensity still needs to be improved. The white light emitting luminescent materials based on single phase possess unique advantages and have a greater control over multiple compositional phosphors in the form of color rendering and luminous efficiency by considering the color re-absorption and ratio control problems among phosphors. [Shang *et al.* 2014] Therefore, the development of potential luminescent materials for display and lighting devices necessitates the search for new, thermally and chemically stable and good efficient single phase white light emitting phosphor materials with strong excitation strengths in the n-UV and blue range, which fulfils the demand of enhancing the luminescence efficiency and reproducibility of pc-WLEDs.

The trivalent lanthanide activators possess special optical properties such as narrow and strong luminescence, long life times, emissions in the entire visible region (red, green and blue), good thermal and chemical stability. [Yuhua *et al.* 2015, Lin *et al.* 2011] Among these, trivalent dysprosium (Dy^{3+}) ion is an excellent activator and have wide applications in mercury free lamps, field emission displays, and plasma display panels. The yellow (570-600 nm) and blue (470-500 nm) emission bands in the visible region are assigned to the forbidden electric dipole transition of ${}^4F_{9/2} \rightarrow {}^6H_{13/2}$ and the allowed magnetic dipole transition of ${}^4F_{9/2} \rightarrow {}^6H_{15/2}$ respectively. [Blasse G 1994] Near white light emission in Dy^{3+} doped luminescent materials is obtained by controlling the yellow to blue (Y/B) intensity ratio to a desired level. The above Dy^{3+} ion transitions mainly depends on the site symmetry, host composition, excitation wavelength and doping concentration of Dy^{3+} at the luminescent centers. [Liu *et al.* 2012, Deng *et al.* 2014] Thus, the Y/B ratio of Dy^{3+} emission is greatly influenced by the covalent effect between Dy^{3+} and O^{2-} and it inversely relates with Z/r , where Z is the charge and r the ionic radius, or electronegativity of the surrounding element M in the ternary oxide $Dy-O-M$. [Su *et al.* 1993] The intra-configurational f-f transitions of RE^{3+} ions have weak excitation levels on account of forbidden parity selection rules. Therefore, the luminescence efficiency of RE^{3+} ions can be greatly improved by transferring the energy from a foreign species to RE^{3+} ions. [Naidu *et al.* 2012] Thereby, there is an immense interest in discovering white light emission phosphors based on a single luminescent center making use of the Dy^{3+} ions emission lines.

Pyrochlore oxides of the general formula $A_2B_2O_7$ (A is a 2^+ or 3^+ ion and B is a 5^+ or 4^+ ion) with a space group $Fd-3m$ with eight molecules per unit cell ($Z = 8$) have wide technological applications owing to their interesting electrical, thermal, magnetic, dielectric, optical and catalytic properties and allows wide variety of aliovalent cation substitution including rare earth ions in the crystal lattice. [Kennedy *et al.* 1997, Fujihara *et al.* 2005, Nobre *et al.* 2003] Recently, lanthanide stannates ($Ln_2Sn_2O_7$ ($Ln = Y, La-Lu$)) have shown interesting properties such as catalytic converter in automobile exhaust gas and combustion gas control, and efficient phosphor materials due to their high chemical stability and melting points (>2000 °C). [Zhu *et al.* 2008] The A sites are occupied by the bigger cations, Ca^{2+} (CN = 8, 1.12 Å), Sr^{2+} (CN = 8, 1.26 Å) La^{3+} (CN = 8, 1.16 Å), and Dy^{3+} (CN = 8, 1.027 Å), at $16d$ (1/2, 1/2, 1/2), eight coordinated forming distorted cubes that constitutes six equal oxygen (O) at a slightly smaller distance from

the central cations and two axial oxygen atoms are at the 8b site. The smaller B cations, Sn^{4+} (CN = 6, 0.69 Å) and Nb^{5+} (CN = 6, 0.64 Å) are at 16c sites (0, 0, 0), six coordinated forming trigonal antiprisms where all the six oxygens are equally placed from the central cations. There are two unique crystallographically nonequivalent lattice sites for oxygen: one at the 48f sites ($x, 1/8, 1/8$) with limiting values of x being 0.3125 and 0.3750 and the other at the 8b sites ($3/8, 3/8, 3/8$). [Subramanian *et al.* 1983] The two types of the cation coordination polyhedra have the D_{3d} symmetry. The radius ratio (RR) criteria, difference in charge, electronic configuration and the polarizability of the cation are crucial for a perfect cubic pyrochlore structure. The host composition modifies the crystal field strength, covalency and energy transfer, and in turn influences the color, intensity and luminescent efficiency of the materials. Wang *et al.* reported the luminescent properties of Dy^{3+} doped $La_2Sn_2O_7$ nanocrystals through combustion synthesis and the transfer of energy from the $La_2Sn_2O_7$ host to dysprosium ions is discussed. [Wang *et al.* 2007] The same group performed the luminescence properties of $La_{2-x}RE_xSn_2O_7$ (RE = Eu and Dy) phosphor nanoparticles via a co-precipitation method and studied the effect of Eu^{3+} doping and Eu^{3+}/Dy^{3+} co-doping on the luminescence properties of $La_2Sn_2O_7$ phosphors. [Wang *et al.* 2006] Cheng *et al.* investigated the photoluminescence and the catalytic oxidation activities in the rare earth stannates $Ln_2Sn_2O_7$ ($Ln = Y, La, Pr, Nd, Sm, Eu, Tb, Dy, Ho, Er, Tm, Yb$ and Lu), and inferred that the properties changed remarkably with the variation of ionic radii of the rare earth elements. [Cheng *et al.* 2008] However, so far there is no detailed investigation of Dy^{3+} doped pyrochlore type materials for producing white light. Therefore, we made an attempt to study the Dy^{3+} doped quaternary pyrochlore system in order to introduce more distortion to manipulate the blue yellow emissions to produce for a white light emission. In this regard, trivalent dysprosium (Dy^{3+}) doped $CaLa_{1-x}SnNbO_7$ proves to be a promising candidate for phosphor converted white-light emitting diodes using UV-LED chip. In the present study, $CaLn_{0.97}SnNbO_7 : 0.03 Dy^{3+}$ ($Ln = La, Gd, Lu, Y$) and a series of $CaLa_{1-x}SnNbO_7$ doped with Dy^{3+} ($x = 0.01, 0.02, 0.03, 0.04$) and $Ca_{1-y}Sr_yLa_{0.97}SnNbO_7 : 0.03 Dy^{3+}$ ($y = 0.1, 0.2, 0.3$) phosphors were developed by a ceramic high temperature route and their excitation and emission properties were investigated.

3.2 Experimental section

3.2.1 Synthesis

Preparation of $CaLn_{0.97}SnNbO_7 : 0.03 Dy^{3+}$ ($Ln = La, Gd, Lu, Y$), $CaLa_{1-x}SnNbO_7 : xDy^{3+}$ ($x = 0.01, 0.02, 0.03, 0.04$) and $Ca_{1-y}Sr_yLa_{0.97}SnNbO_7 : 0.03 Dy^{3+}$ ($y = 0.1, 0.2, 0.3$) samples:

In the present work, $CaLn_{0.97}SnNbO_7 : 0.03 Dy^{3+}$ ($Ln = La, Gd, Lu, Y$) and a series of $CaLa_{1-x}SnNbO_7 : xDy^{3+}$ ($x = 0, 0.01, 0.02, 0.03, 0.04$) and $Ca_{1-y}Sr_yLa_{0.97}SnNbO_7 : 0.03 Dy^{3+}$ ($y = 0.1, 0.2, 0.3$) phosphor samples were developed by the conventional high temperature ceramic route by taking $CaCO_3$, $SrCO_3$, La_2O_3 , Gd_2O_3 , Lu_2O_3 , Y_2O_3 , SnO_2 , Nb_2O_5 , Dy_2O_3 (All chemicals are from Sigma Aldrich, 99.99% purity) as the starting raw materials. The right stoichiometric amounts of these chemicals were taken and then mixed nicely in an agate mortar using acetone medium. After homogeneous mixing the product was kept for drying in an air oven maintained at $100^\circ C$ temperature. The above process of mixing and drying was done many times to get a homogeneous product. The obtained product was made into a pellet and first calcined at $1200^\circ C$ for 6 h on an alumina plate in an electrically heated furnace. Then the calcination was done at $1300^\circ C$ for 6 h with an intermittent powdering to obtain the final single phase sample. The calcined pellet was made into a fine powder for further characterizations.

3.2.2 Characterisation techniques

The crystalline structure was verified by the X-ray powder diffraction (XRD) analysis using powder X-ray diffractometer (X'Pert Pro PANalytical). The diffraction patterns were recorded in the 2θ scan range from 10° to 90° with a step size of 0.016° with the system operating at 40 kV/30 mA with a Ni filtered Cu-K α radiation ($\lambda=0.15406$ nm). The shape and size of the phosphor particles was examined by a scanning electron microscope (JEOL, JSM-5600LV) operated at 15kV. Absorbance study of the samples were carried out using a Shimadzu, UV-2450 UV-Vis spectrophotometer in the 400–700 nm wavelength range using barium sulfate as a reference. The photoluminescence measurements were made on a Fluorolog HORIBA fluorescence spectrophotometer with a Xe lamp (450 W) as the excitation source. Luminescence lifetime of the phosphors was obtained by the phosphorimeter attached to the Fluorolog@3 spectrofluorimeter. CIE chromaticity coordinates were obtained using the software CIE calculator.

3.3 Results and discussion

3.3.1. Powder X-ray diffraction analysis

Powder X-ray diffraction patterns of $\text{CaLn}_{0.97}\text{SnNbO}_7 : 0.03 \text{Dy}^{3+}$ ($\text{Ln} = \text{La, Gd, Lu, Y}$) and $\text{CaLa}_{1-x}\text{SnNbO}_7 : x\text{Dy}^{3+}$ ($x = 0.01, 0.02, 0.03, 0.04$) samples are shown in Figure 3.1 and Figure 3.2 respectively.

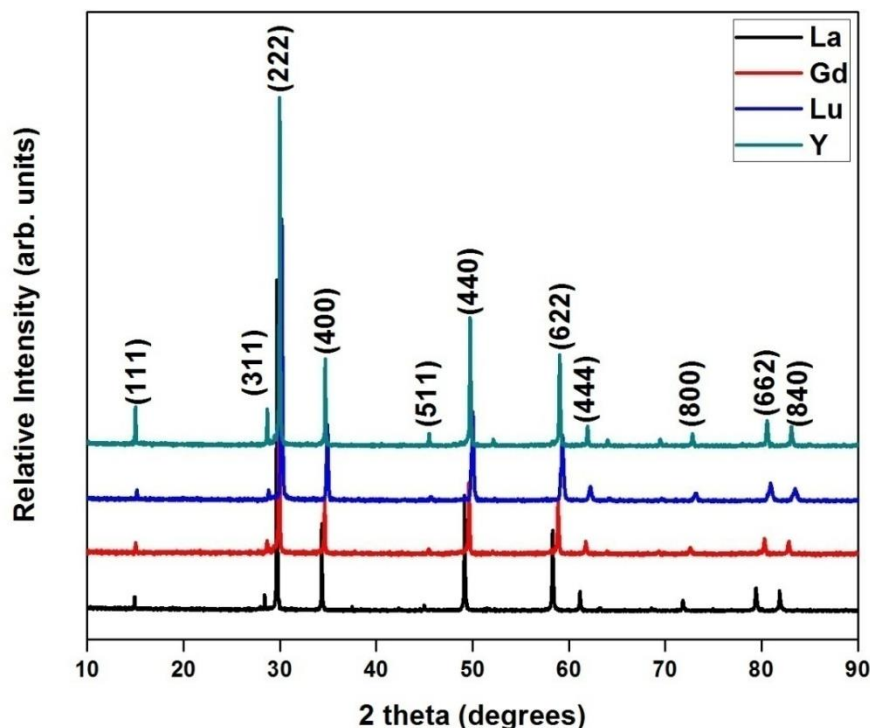


Figure 3.1 : Powder X-ray diffraction patterns of $\text{CaLn}_{0.97}\text{SnNbO}_7 : 0.03 \text{Dy}^{3+}$ ($\text{Ln} = \text{La, Gd, Lu, Y}$) phosphor samples.

The strong and sharp diffraction peaks indicate that samples are highly crystalline and no additional peaks from impurities were observed with incorporation of Dy^{3+} ions. Considering the matching ionic radius and coordination number of the ions, in all the cases one expects the Dy^{3+} ions are incorporated to the Ln^{3+} sites [Shannon R. D. 1976]. All the $\text{CaLn}_{0.97}\text{SnNbO}_7 : 0.03 \text{Dy}^{3+}$ ($\text{Ln} = \text{La, Gd, Lu, Y}$) compositions crystallize in the cubic pyrochlore type structure with a space group Fd-3m forming their their respective lanthanide stannates. For the $\text{CaLa}_{1-x}\text{SnNbO}_7 : x\text{Dy}^{3+}$ ($x = 0.01, 0.02, 0.03, 0.04$) compositions all the phosphor samples crystallize in the cubic pyrochlore type structure with a space group Fd-3m in line with the JCPDS file No. 01-088-0446. [Mahesh *et al.* 2012].

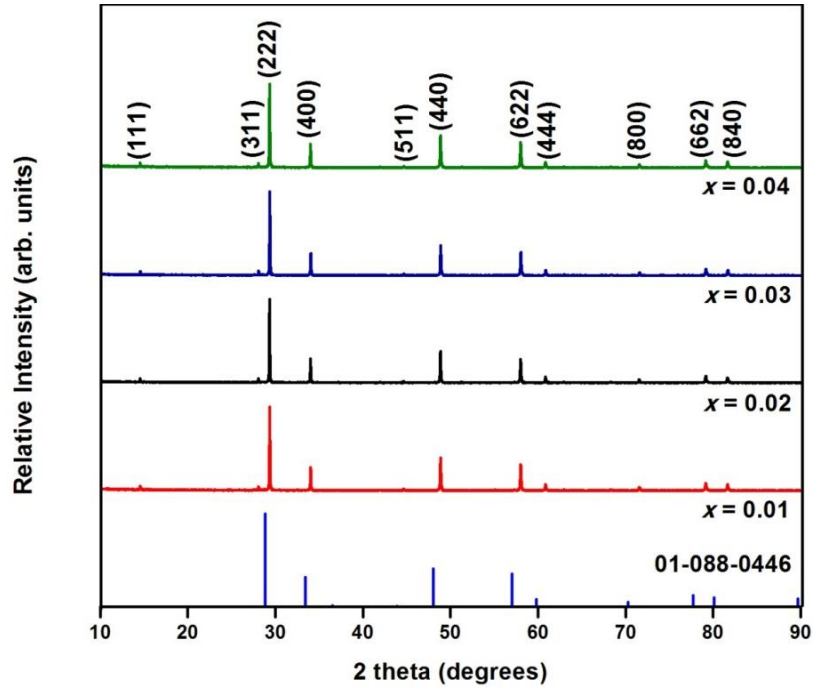


Figure 3.2 : Powder X-ray diffraction patterns of $\text{CaLa}_{1-x}\text{SnNbO}_7 : x\text{Dy}^{3+}$ ($x = 0.01, 0.02, 0.03, 0.04$) samples.

Table 3.1. : Lattice parameters and unit cell volume of Dy^{3+} doped $\text{CaLa}_{1-x}\text{SnNbO}_7$ samples.

x	Lattice Parameters $a = b = c$ (\AA)	Unit Cell Volume (\AA) ³
0.01	10.5451	1172.6059
0.02	10.5431	1171.9389
0.03	10.5429	1171.8722
0.04	10.5419	1171.5388

In the pyrochlore structure Dy^{3+} (ionic radius: 1.027 \AA) ions are incorporated to the La^{3+} (ionic radius: 1.16 \AA) sites than to the Ca (ionic radius: 1.12 \AA) site accounting for the same valence state and the matching ionic radius. [Shannon R. D. 1976] Incorporation of Dy^{3+} ions into the lattice decreases the lattice volume from $1172.6059 (\text{\AA})^3$ to $1171.5388 (\text{\AA})^3$ with the variation in the Dy^{3+} concentration through 0.01 to 0.04. The decreasing

trend in the lattice parameter values when Dy^{3+} ions replaces comparatively larger La^{3+} ions with increasing Dy^{3+} ion concentration further confirms the effective doping of Dy^{3+} into the crystal lattice. Lattice parameters and unit cell volumes of Dy^{3+} doped $CaLa_{1-x}SnNbO_7$ samples are listed in Table 3.1.

3.3.2. Morphological Studies

Scanning electron micrographs of the phosphor powder samples were imaged and the morphology of all the Dy^{3+} incorporated samples is given in Figure 3.3. The particles were slightly agglomerated and were homogeneous with an average particle size of about 0.5 — 1 μm .

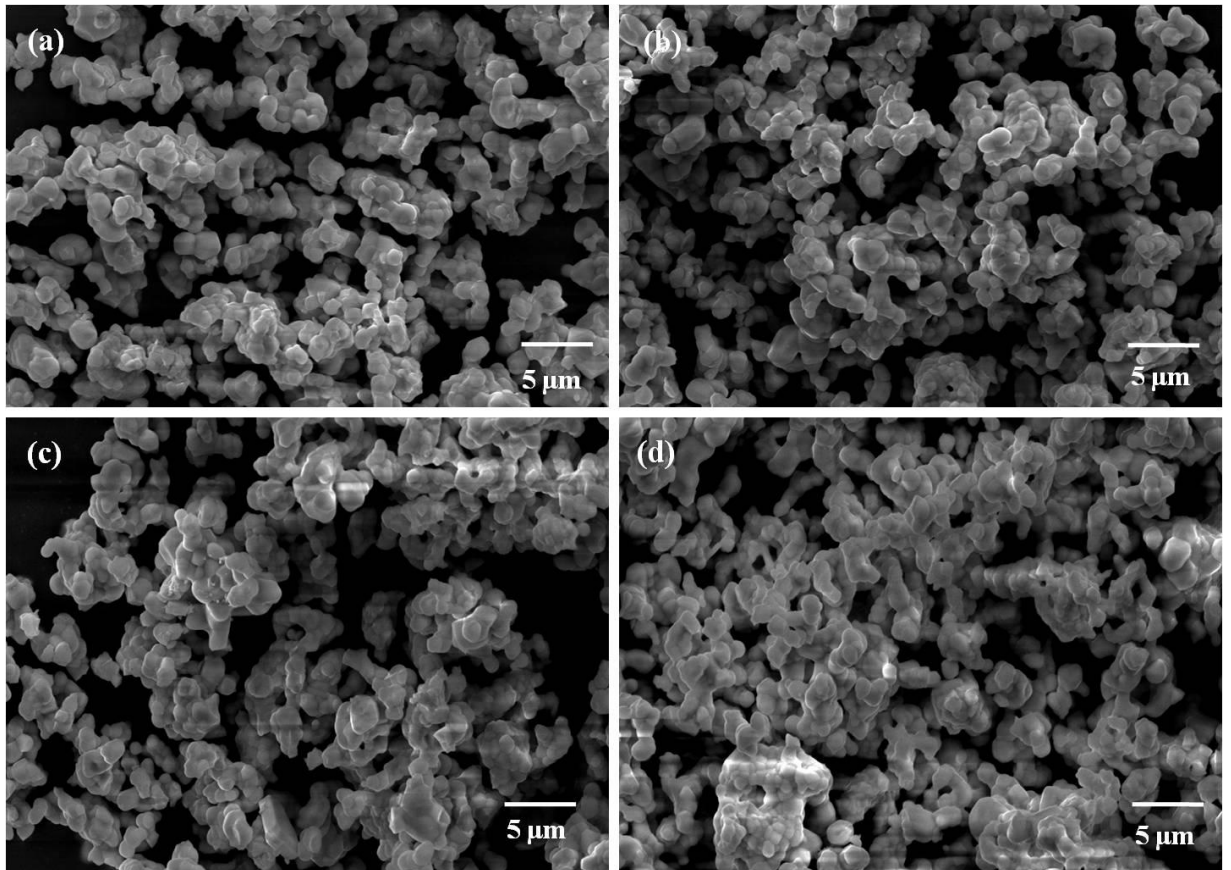


Figure 3.3 : SEM micrographs of $CaLa_{1-x}SnNbO_7:xDy^{3+}$ phosphor samples with different Dy^{3+} concentrations: (a) $x = 0.01$, (b) $x = 0.02$, (c) $x = 0.03$, (d) $x = 0.04$.

3.3.3. Optical and Photoluminescence Studies

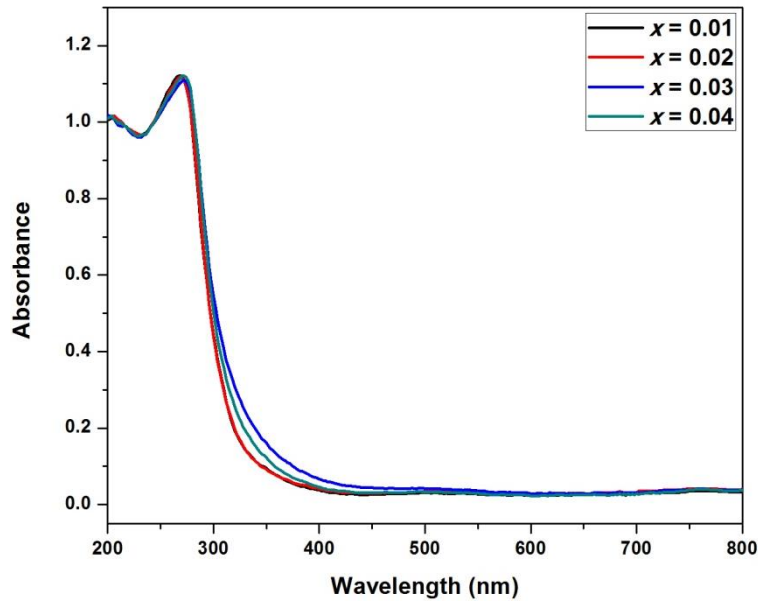


Figure 3.4 : UV-Visible absorption spectra of $\text{CaLa}_{1-x}\text{SnNbO}_7 : x\text{Dy}^{3+}$ ($x = 0.01, 0.02, 0.03, 0.04$) phosphor powders.

The UV-Visible absorption spectra of Dy^{3+} doped $\text{CaLa}_{1-x}\text{SnNbO}_7$ is shown in Figure 3.4. Absorption spectra of all the samples show good absorption in the UV region around 388 nm enabling these phosphor materials to be used in pc WLEDs with UV LED chip.

The luminescence excitation and emission spectra of the $\text{CaLn}_{0.97}\text{SnNbO}_7 : 0.03\text{Dy}^{3+}$ ($\text{Ln} = \text{La}, \text{Gd}, \text{Lu}, \text{Y}$) and $\text{CaLa}_{1-x}\text{SnNbO}_7 : x\text{Dy}^{3+}$ ($x = 0.01, 0.02, 0.03, 0.04$) samples have been carefully studied. The photoluminescence excitation spectra of the $\text{CaLn}_{0.97}\text{SnNbO}_7 : 0.03\text{Dy}^{3+}$ ($\text{Ln} = \text{La}, \text{Gd}, \text{Lu}, \text{Y}$) and $\text{CaLa}_{1-x}\text{SnNbO}_7 : x\text{Dy}^{3+}$ ($x = 0.01, 0.02, 0.03, 0.04$) samples were recorded and the spectrum profiles of the samples for an emission monitored at 477 nm, 487 nm and 589 nm are given in Figure 3.5, Figure 3.6, Figure 3.7, Figure 3.8, Figure 3.9 and Figure 3.10 respectively. A broad band from 250 nm to 310 nm is assigned to the charge transfer transition from the oxygen to the metal. [Yin *et al.* 2012] This broad CT band in the excitation spectra results from the resultant effect of $\text{O}_{2p} \rightarrow \text{Dy}_{4f}$ and $\text{O}_{2p} \rightarrow \text{Nb}_{4d}$ CT transitions. Among all the lanthanides $\text{Ln} = \text{La}$ exhibited the highest luminescent emission intensities leaving all the other lanthanides $\text{Ln} = \text{Gd}, \text{Lu}$ and Y far behind by a factor of more than 10. Considering the

requirements of a phosphor material to be applicable in device fabrication, we are focussing our study on the $\text{CaLa}_{1-x}\text{SnNbO}_7 : x\text{Dy}^{3+}$ system in detail.

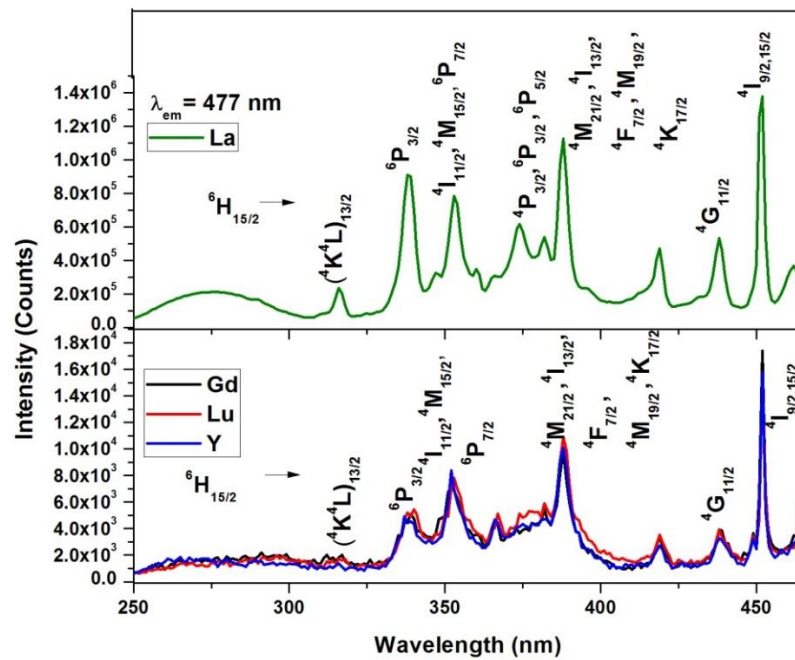


Figure 3.5 : Excitation spectra of $\text{CaLn}_{0.97}\text{SnNbO}_7 : 0.03 \text{Dy}^{3+}$ ($\text{Ln} = \text{La, Gd, Lu, Y}$) for an emission at 477 nm.

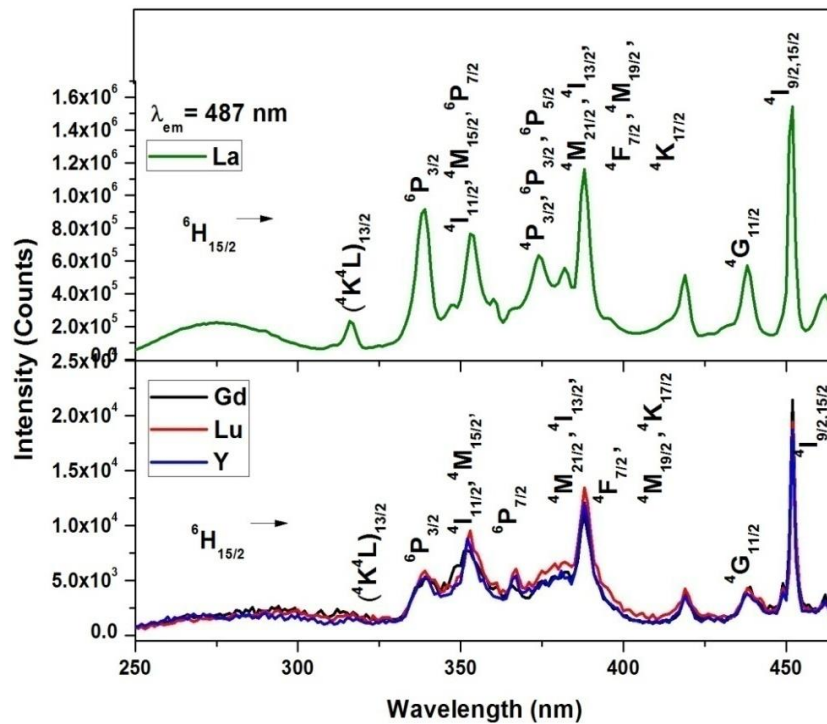


Figure 3.6 : Excitation spectra of $\text{CaLn}_{0.97}\text{SnNbO}_7 : 0.03 \text{Dy}^{3+}$ ($\text{Ln} = \text{La, Gd, Lu, Y}$) for an emission at 487 nm.

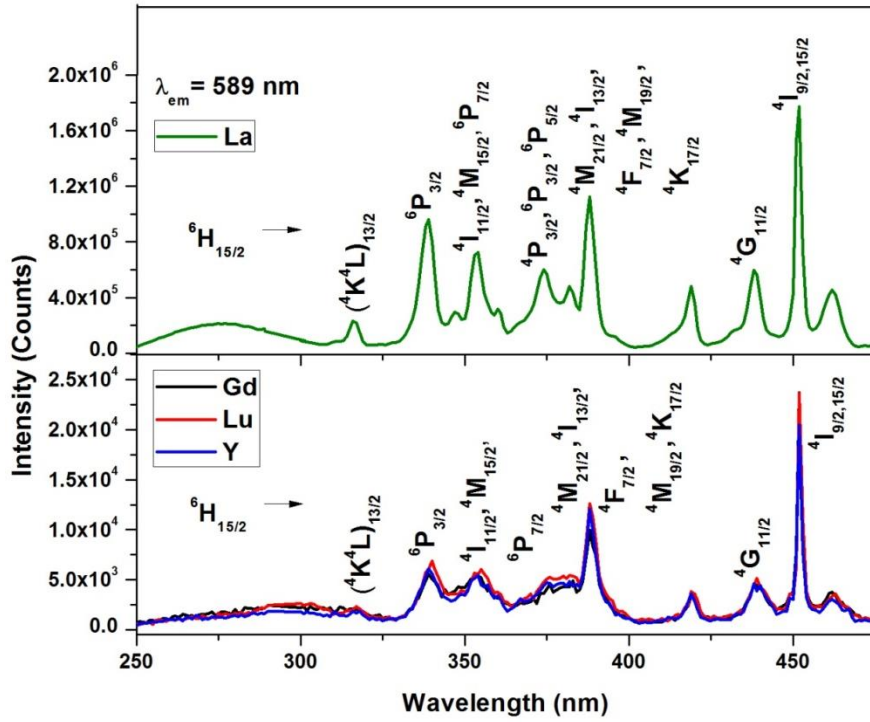


Figure 3.7 : Excitation spectra of $\text{CaLn}_{0.97}\text{SnNbO}_7 : 0.03 \text{Dy}^{3+}$ ($\text{Ln} = \text{La, Gd, Lu, Y}$) for an emission at 589 nm.

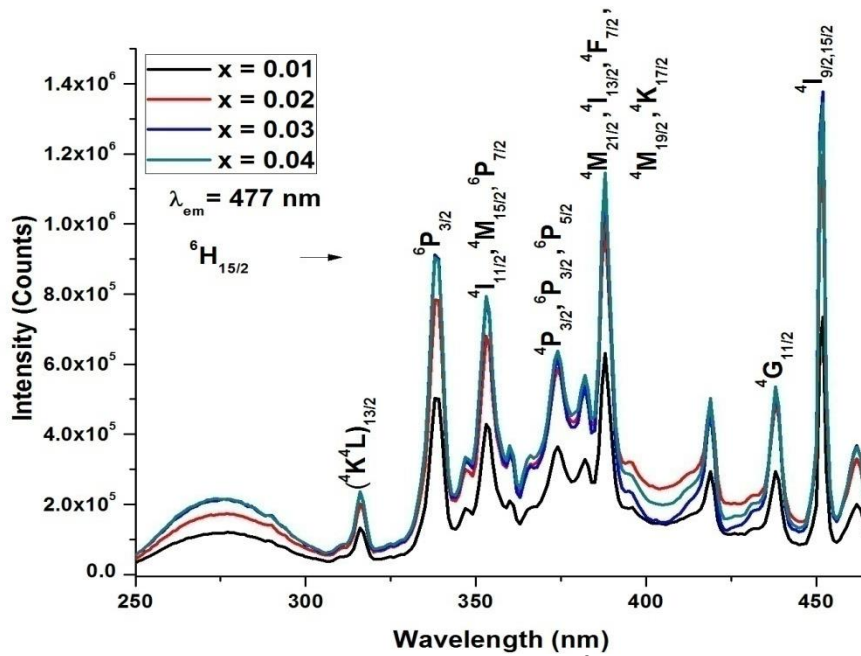


Figure 3.8 : Excitation spectra of $\text{CaLa}_{1-x}\text{SnNbO}_7 : x\text{Dy}^{3+}$ ($x = 0.01, 0.02, 0.03, 0.04$) for an emission at 477 nm.

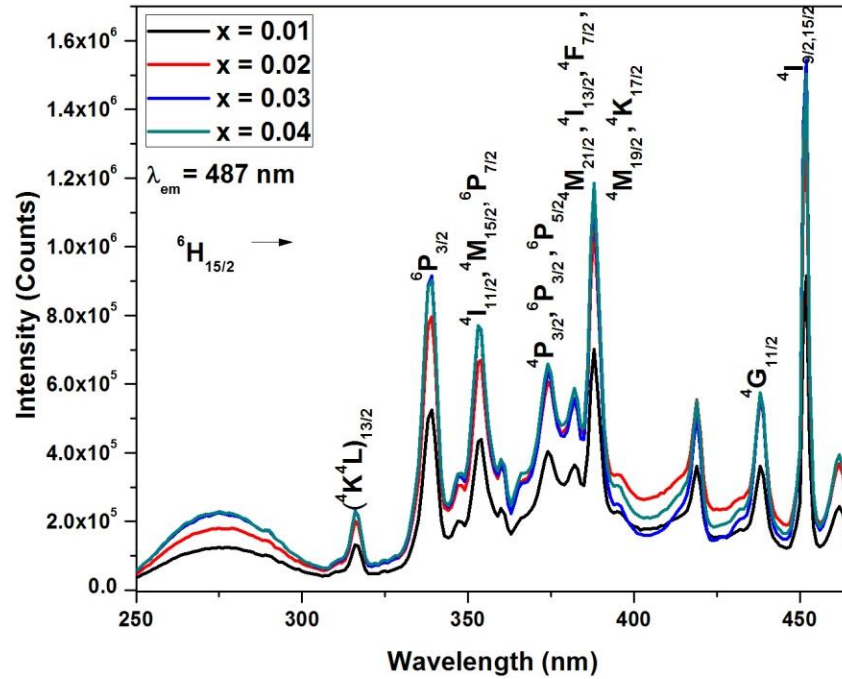


Figure 3.9 : Excitation spectra of $\text{CaLa}_{1-x}\text{SnNbO}_7:x\text{Dy}^{3+}$ ($x = 0.01, 0.02, 0.03, 0.04$) for an emission at 487 nm.

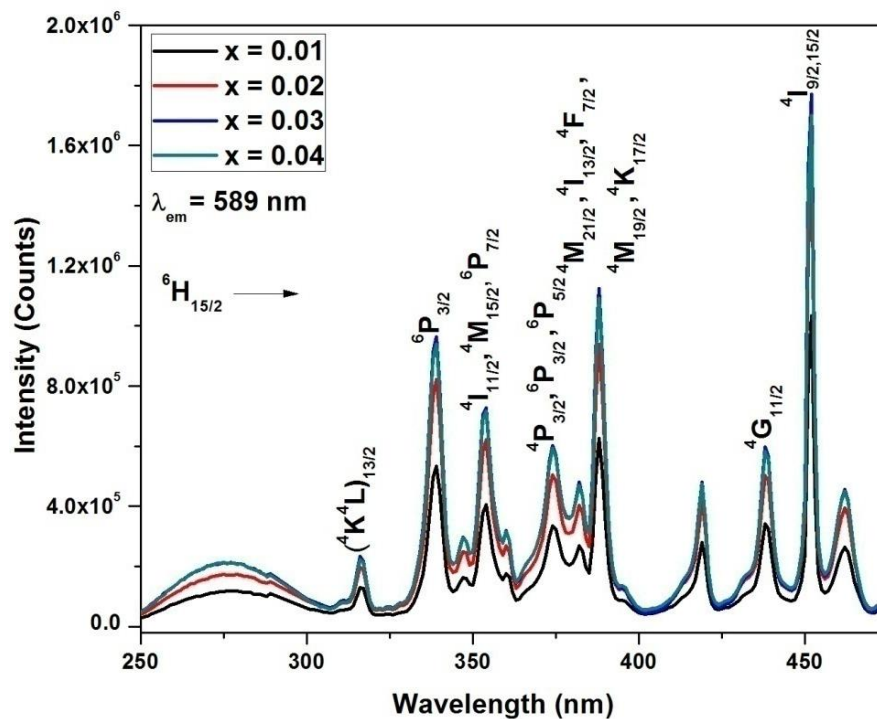


Figure 3.10 : Excitation spectra of $\text{CaLa}_{1-x}\text{SnNbO}_7:x\text{Dy}^{3+}$ ($x = 0.01, 0.02, 0.03, 0.04$) for an emission at 589 nm.

The sharp and intense characteristic absorption lines in the UV region and blue region beyond 310 nm owing to the intra-configurational f-f transitions of Dy^{3+} peaks at 338 nm (${}^6\text{H}_{15/2} \rightarrow {}^6\text{P}_{3/2}$), 353 nm (${}^6\text{H}_{15/2} \rightarrow {}^4\text{I}_{11/2} + {}^4\text{M}_{15/2} + {}^6\text{P}_{7/2}$), 374 nm (${}^6\text{H}_{15/2} \rightarrow {}^4\text{P}_{3/2} + {}^6\text{P}_{3/2} + {}^6\text{P}_{5/2}$), 388 nm (${}^6\text{H}_{15/2} \rightarrow {}^4\text{M}_{21/2} + {}^4\text{I}_{13/2} + {}^4\text{F}_{7/2} + {}^4\text{M}_{19/2} + {}^4\text{K}_{17/2}$), 418 nm, 438 nm (${}^6\text{H}_{15/2} \rightarrow {}^4\text{G}_{11/2}$) and 452 nm (${}^6\text{H}_{15/2} \rightarrow {}^4\text{I}_{9/2} + {}^4\text{I}_{15/2}$) which are attributed to the ground state of ${}^6\text{H}_{15/2}$ to the various excited states of $4f^9$ electronic configurations of the Dy^{3+} ions. The intensities of the f-f transitions are more stronger than the charge transfer band. Among all the excitation peaks, the peak located at 452 nm has the highest intensity, therefore the emission spectra were recorded for different doping concentrations of Dy^{3+} doped $\text{CaLa}_{1-x}\text{SnNbO}_7$ samples under the excitation at 452 nm wavelength in order to know the optimized Dy^{3+} concentration. The excitation levels of the intra-configurational $4f$ transitions of Dy^{3+} are greatly enhanced with increased concentration of dysprosium. This particular excitation wavelength matches to the emission of the blue LED chip and hence these phosphor material can be easily excited by the electroluminescence of the blue LED chip for developing phosphor converted WLEDs.

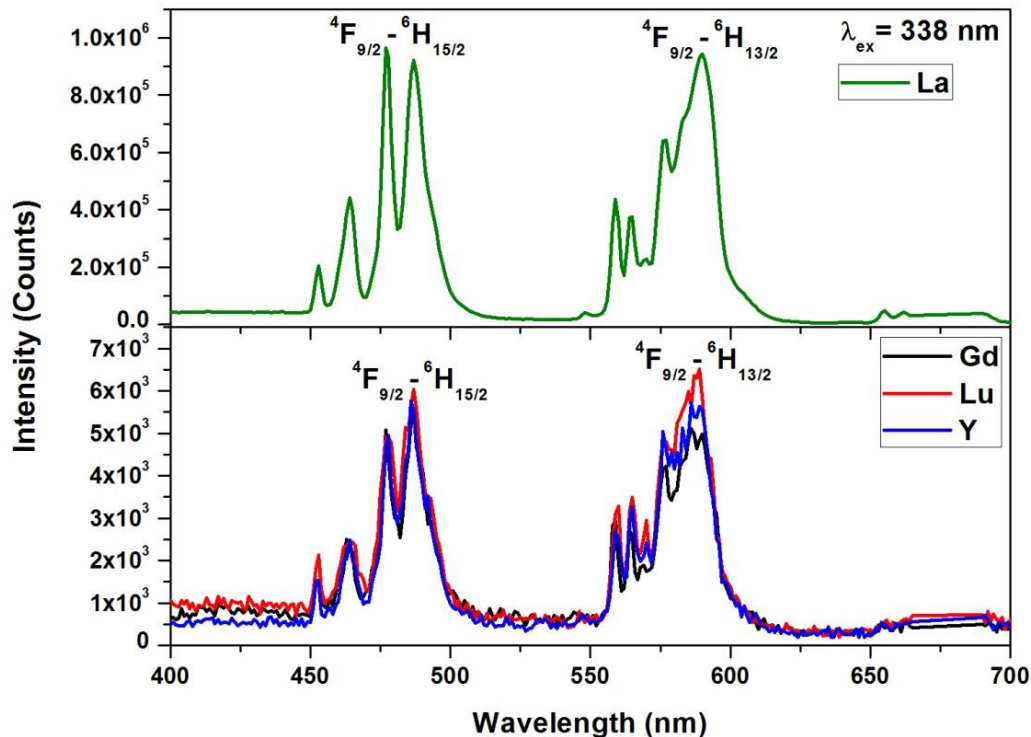


Figure 3.11 : Emission spectra of $\text{CaLn}_{0.97}\text{SnNbO}_7 : 0.03 \text{Dy}^{3+}$ ($\text{Ln} = \text{La, Gd, Lu, Y}$) under 338 nm excitation.

The photoluminescence emission spectra of $\text{CaLn}_{0.97}\text{SnNbO}_7 : 0.03 \text{Dy}^{3+}$ ($\text{Ln} = \text{La, Gd, Lu, Y}$) and $\text{CaLa}_{1-x}\text{SnNbO}_7 : x\text{Dy}^{3+}$ ($x = 0.01, 0.02, 0.03, 0.04$) samples under an excitation of 338 nm, 388 nm and 452 nm are given in Figure 3.11, Figure 3.12, Figure 3.13, Figure 3.14, Figure 3.15 and Figure 3.16 respectively.

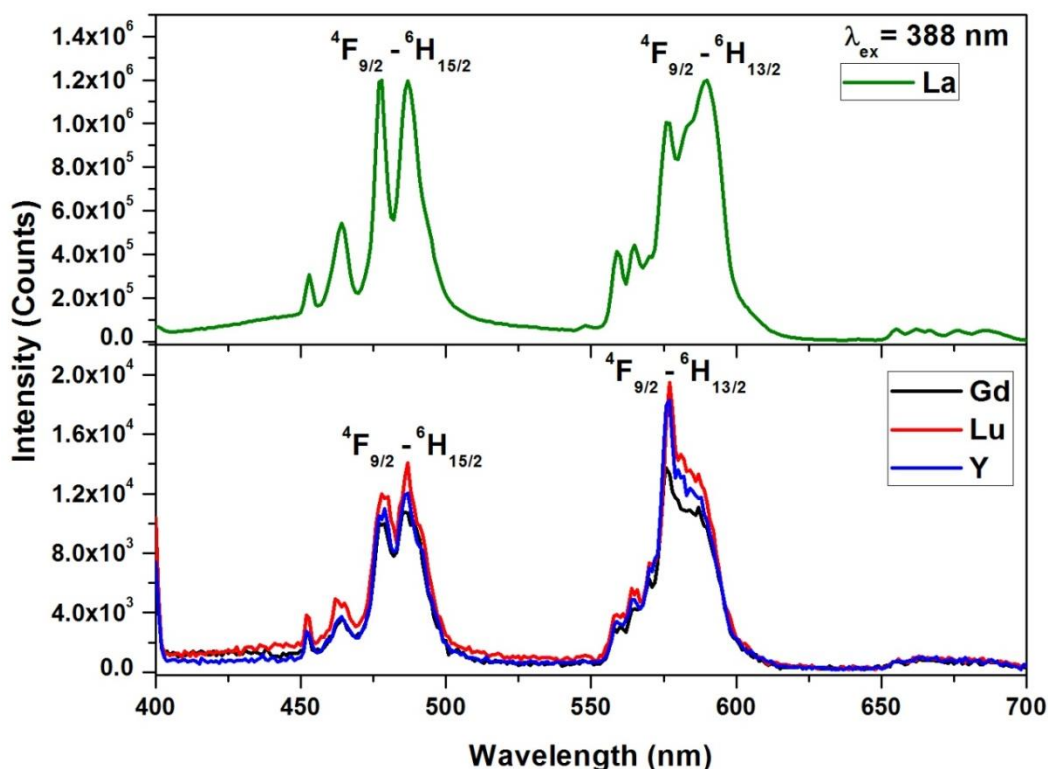


Figure 3.12 : Emission spectra of $\text{CaLn}_{0.97}\text{SnNbO}_7 : 0.03 \text{Dy}^{3+}$ ($\text{Ln} = \text{La, Gd, Lu, Y}$) under 388 nm excitation.

The Dy^{3+} ions emit in the visible and near infrared regions of the spectrum due to the intraionic transitions from the $^4\text{F}_{9/2}$ excited state to the $^6\text{H}_{15/2}$ ground state and the $^6\text{H}_{13/2,11/2,9/2}$ levels under ultraviolet excitation. In a distorted crystalline field, the degeneracy of the Dy^{3+} ion levels is lifted, allowing the mixing of the wave function of opposite parity. This promotes the hypersensitive $^4\text{F}_{9/2} \rightarrow ^6\text{H}_{13/2}$ ($\Delta L = 2, \Delta J = 2$) transition of Dy^{3+} of forced electric dipole nature, otherwise parity forbidden, resulting in the yellow band emission centred at 589 nm that is strongly affected by changes in the surrounding ions. In addition to the yellow luminescence, blue emission bands at 487 nm and 477 nm assigned to the magnetic dipole allowed transition of $^4\text{F}_{9/2} \rightarrow ^6\text{H}_{15/2}$ is also observed. For Dy^{3+} ions located at a low symmetry local site and without an inversion

center, the ${}^4\text{F}_{9/2} \rightarrow {}^6\text{H}_{13/2}$ transition is dominant and at high symmetry sites with an inversion center a higher intensity of the ${}^4\text{F}_{9/2} \rightarrow {}^6\text{H}_{15/2}$ transition is observed in comparison with the intensity of the yellow emission. [Soares *et al.* 2011]

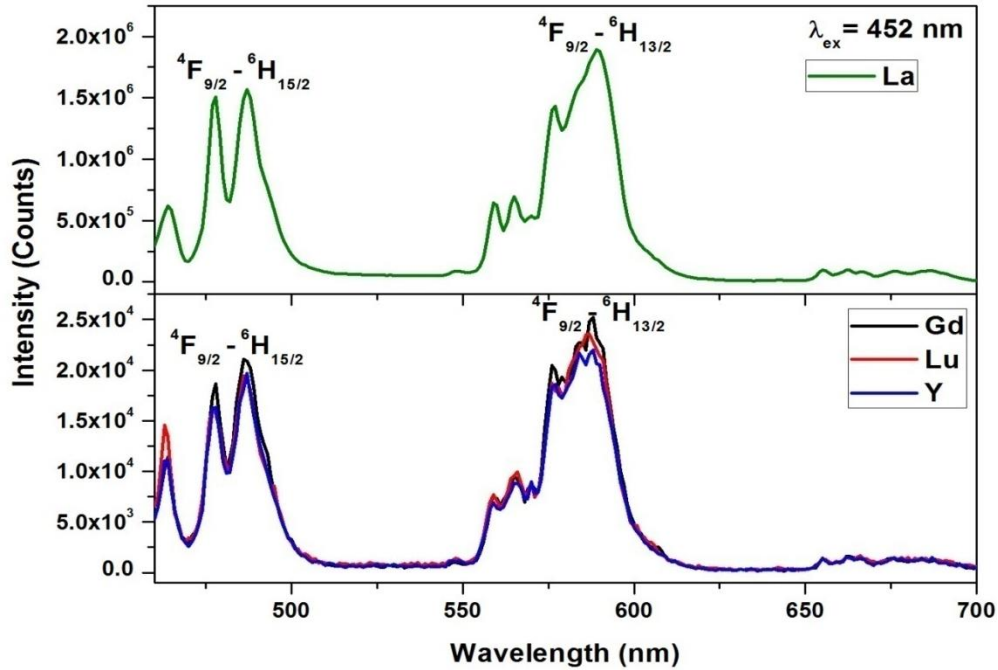


Figure 3.13 : Emission spectra of $\text{CaLn}_{0.97}\text{SnNbO}_7 : 0.03 \text{Dy}^{3+}$ ($\text{Ln} = \text{La, Gd, Lu, Y}$) under 452 nm excitation.

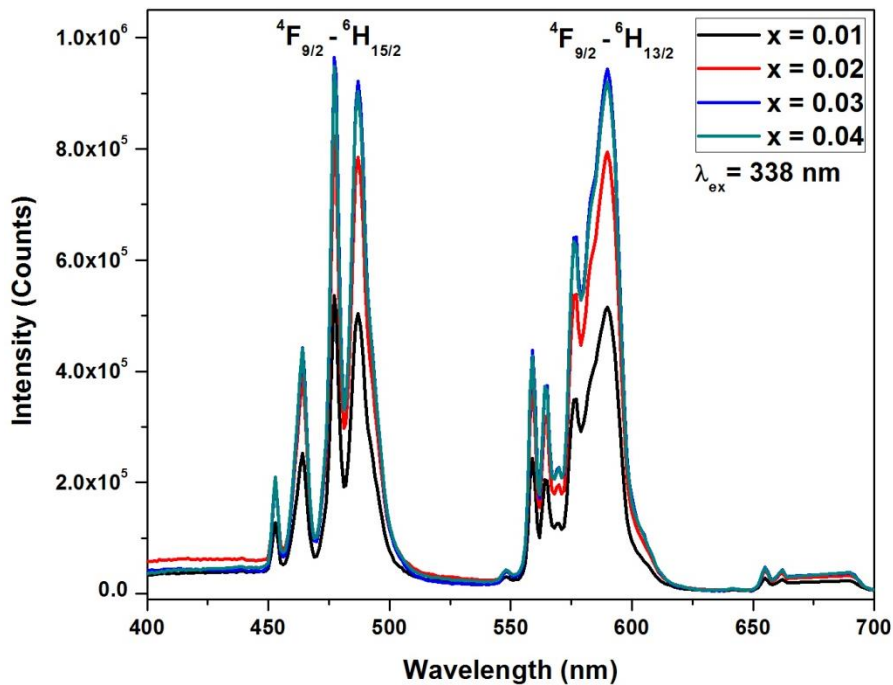


Figure 3.14 : Emission spectra of $\text{CaLa}_{1-x}\text{SnNbO}_7 : x\text{Dy}^{3+}$ ($x = 0.01, 0.02, 0.03, 0.04$) under 338 nm excitation.

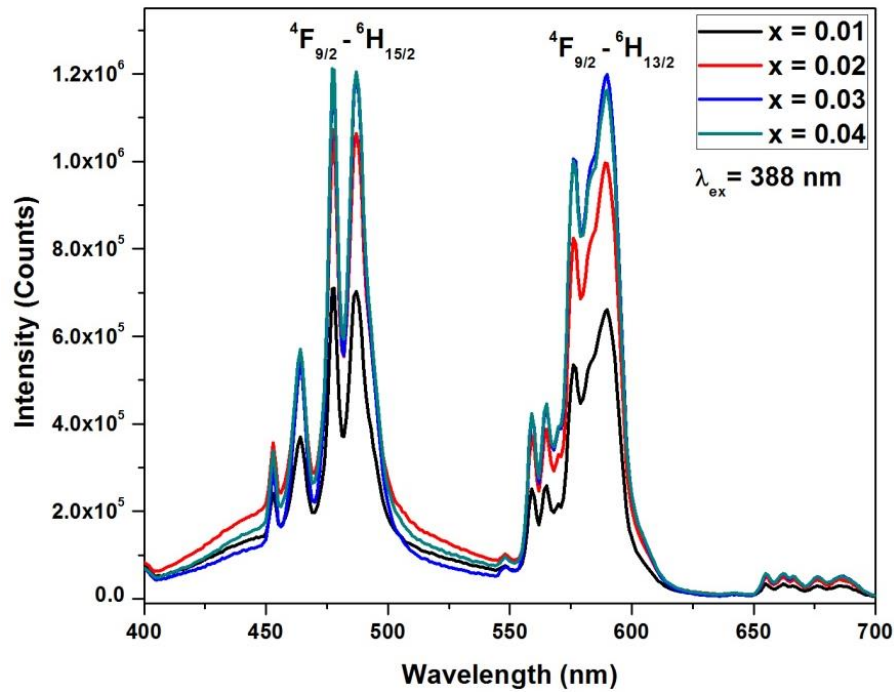


Figure 3.15 : Emission spectra of $\text{CaLa}_{1-x}\text{SnNbO}_7:x\text{Dy}^{3+}$ ($x = 0.01, 0.02, 0.03, 0.04$) under 388 nm excitation.

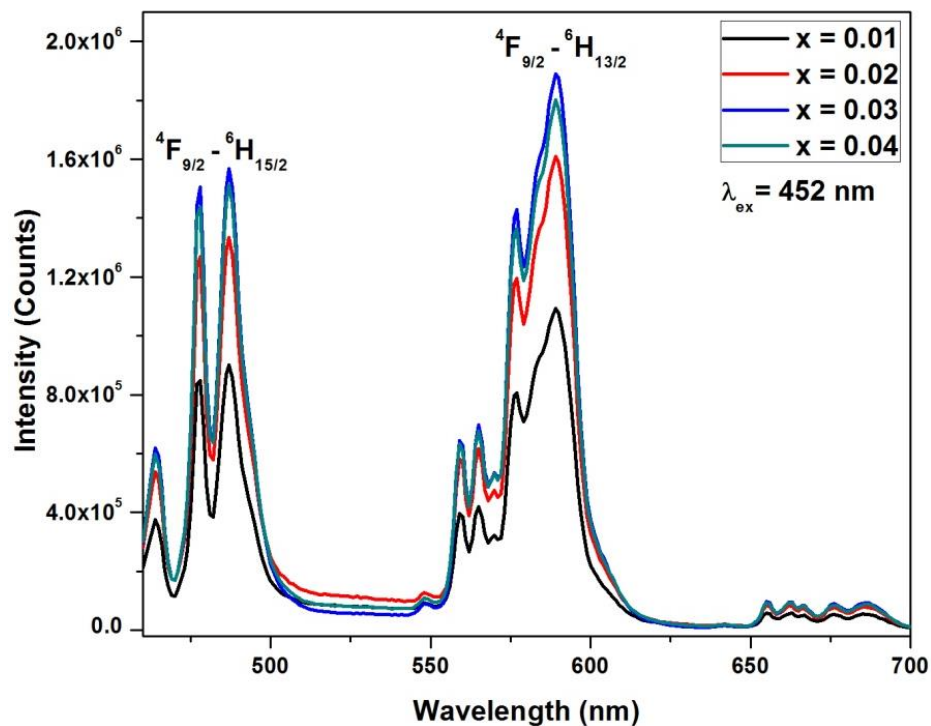


Figure 3.16 : Emission spectra of $\text{CaLa}_{1-x}\text{SnNbO}_7:x\text{Dy}^{3+}$ ($x = 0.01, 0.02, 0.03, 0.04$) under 452 nm excitation.

Both the transitions are of comparable intensity leading to a small deviation from inversion symmetry. Splitting of the ${}^4F_{9/2} \rightarrow {}^6H_{15/2}$ magnetic dipole transition is observed and provides information on the crystal field effect at the activator sites. Upon all the excitation wavelengths, the $CaLn_{0.97}SnNbO_7 : 0.03 Dy^{3+}$ ($Ln = La, Gd, Lu, Y$) and $CaLa_{1-x}SnNbO_7 : xDy^{3+}$ ($x = 0.01, 0.02, 0.03, 0.04$) phosphors show the characteristic blue yellow luminescence of Dy^{3+} . The emission profiles of all the phosphor samples are similar in shape under the various excitation wavelengths but only change in the band intensity. White light is obtained by the mixing of the complimentary blue and the yellow emission bands.

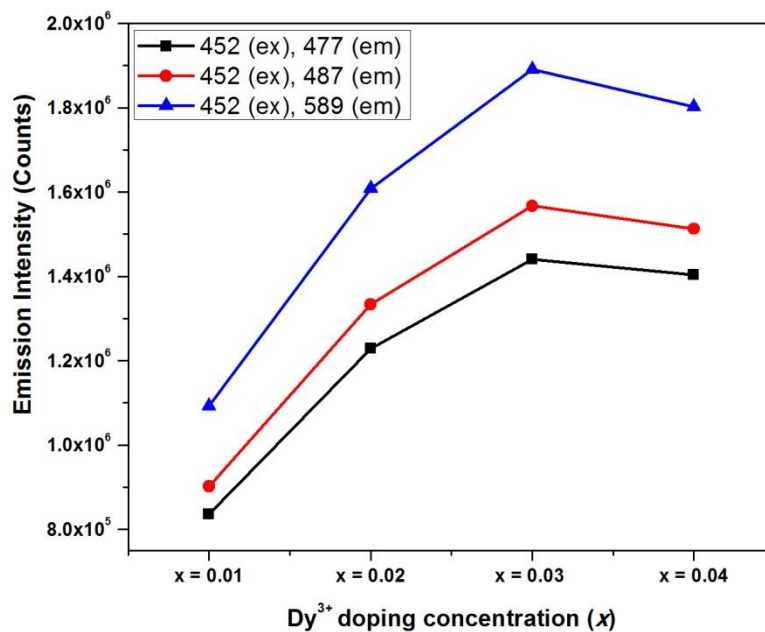
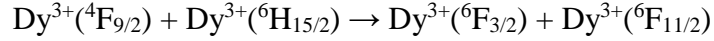


Figure 3.17 : Variation in the luminescent intensities with Dy^{3+} doping concentrations of $CaLa_{1-x}SnNbO_7 : xDy^{3+}$ ($x = 0.01, 0.02, 0.03, 0.04$) under 452 nm excitation for the emissions at 477nm (black line), 487 nm (red line) and 589 nm (blue line).

Figure 3.17 shows the PL intensity variations for different Dy^{3+} doping concentrations under 452 nm excitation. The concentration of the activator ions, excitation wavelength, host composition, chemical nature of the surrounding ions and the luminescent centres has direct influence on the luminescence properties of phosphors. Generally, lower amounts of activator doping exhibit weak luminescence whereas higher amounts of doping leads to quenching of luminescence. As the concentration of the Dy^{3+} ions increases, the emission intensities of all the samples increases, and it reaches to a maximum at $x = 0.03$, beyond this optimum doping concentration, the intensity decreases with further increase in Dy^{3+} ions concentration due to the concentration quenching

phenomena and the quenching of Dy³⁺ ions luminescence often occurs at low concentration. The quenching of the luminescence results from the resonance energy transfer between the activator ions at high activator concentrations. During this process, the excitation energy will be trapped at the crystal defects or the quenching site non-radiatively leading to a decrease of the PL emission intensity. [Yen *et al.* 2007] These transitions are mainly



According to the method given by Blasse, using the critical concentration for the concentration quenching, the critical distance, R_c , for which the probability of energy transfer between the activators equals the probability of radiative emission of the activators, can be calculated as

$$R_c \approx 2(3V/4\pi x_c N)^{1/3}$$

where, V is the volume of the unit cell, x_c is the critical concentration of the activator ion and N is the number of the sites available to the activator ions in the unit cell. This implies that for the critical concentration the average shortest distance between nearest activator ions in which energy transfer occurs is equal to the critical distance. For the CaLaSnNbO₇ host, $V = 1171.8722 \text{ (\AA)}^3$, $x_c \approx 0.03$, $N = 8$, the value of critical distance was found to be 10.526 Å. [Blasse G. 1969] A value of R_c greater than 5 Å favours multipole–multipole interaction and is the major cause of concentration quenching of Dy³⁺ in the phosphors.

The luminescence emission spectra of CaLa_{0.97}SnNbO₇ : 0.03 Dy³⁺ under the different excitation wavelengths ($\lambda_{\text{ex}} = 338 \text{ nm}$, 353 nm, 388 nm and 452 nm) given in Figure 3.18 reveals that the emission band shape and the band position has no much observable differences except in the emission intensity. Asymmetric ratio, the relative integrated intensity ratio of the electric dipole allowed (⁴F_{9/2}-⁶H_{13/2}) to the magnetic dipole allowed (⁴F_{9/2}-⁶H_{15/2}) transition depends on the host crystal structure and gives a measure of the structural distortion around Dy³⁺ ions and the nature of the doping sites. [Zhou *et al.* 2007] Reports show that the Y/B ratio of Dy³⁺ increases with the increase in the ionic radius of its surrounding elements. Thus, Dy³⁺ can be used as a luminescent structural probe to determine the site symmetry of rare earth ions. The yellow-to-blue

emission intensity ratios (Y/B) of Dy^{3+} in CaLaSnNbO_7 were not much affected by exciting the samples at different wavelengths.

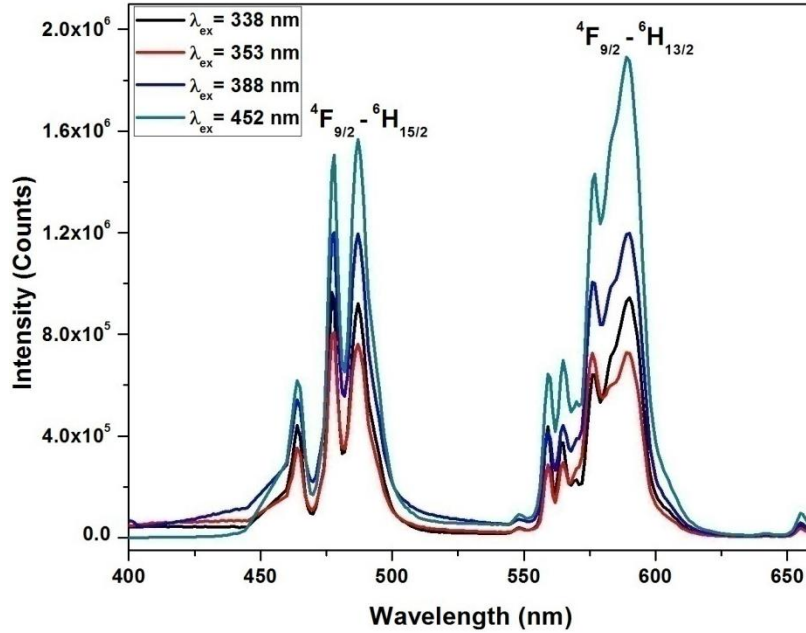


Figure 3.18 : Emission spectra of $\text{CaLa}_{0.97}\text{SnNbO}_7:0.03\text{Dy}^{3+}$ under different excitation wavelengths. ($\lambda_{\text{ex}} = 338 \text{ nm}, 353 \text{ nm}, 388 \text{ nm}$ and 452 nm)

Table 3.2 : Y/B ratio of Dy^{3+} doped $\text{CaLa}_{1-x}\text{SnNbO}_7$ samples under different excitation wavelengths.

x	Y/B ratio 338 nm (Ex)	Y/B ratio 388 nm (Ex)	Y/B ratio 452 nm (Ex)
0.01	1.0228	0.942	1.212
0.02	1.011	0.935	1.206
0.03	1.024	1.003	1.207
0.04	1.019	0.966	1.191

For the optimum concentration $x = 0.03$, the Y/B values are obtained as 1.024, 0.956, 1.003 and 1.207 under 338 nm, 353 nm, 388 nm and 452 nm respectively. This points that there is only one crystallographic site available for the activator Dy^{3+} ions resulting in a single emission centre. Dy^{3+} ions are located in the CaLaSnNbO_7 crystal lattice without any distortion as the asymmetric ratio has almost a constant value for

different UV excitations. When Dy^{3+} is substituted for La^{3+} with the same valency in the phosphor host $CaLaSnNbO_7$, the Y/B ratio does not vary much with the variation in the concentration of Dy^{3+} . The Y/B ratios are given in the Table 3.2. The CIE color coordinates of all the samples are very close to the standard chromaticity coordinates of white light and are given in the Table 3.3. Hence, Dy^{3+} doped quaternary pyrochlore system $CaLa_{1-x}SnNbO_7$ is found to be a promising candidate for a single phase white light emitting phosphor.

Table 3.3 : CIE values of Dy^{3+} doped $CaLa_{1-x}SnNbO_7$ samples under different excitation wavelengths.

x	Color Co-ordinates	Color Co-ordinates	Color Co-ordinates
	(x, y) 338 nm (Ex)	(x, y) 388 nm (Ex)	(x, y) 452 nm (Ex)
0.01	(0.359, 0.344)	(0.321, 0.328)	(0.314, 0.272)
0.02	(0.359, 0.342)	(0.324, 0.329)	(0.314, 0.270)
0.03	(0.372, 0.351)	(0.355, 0.348)	(0.384, 0.365)
0.04	(0.368, 0.350)	(0.342, 0.342)	(0.379, 0.368)

The photoluminescence decay curves of $Dy^{3+} {}^4F_{9/2} \rightarrow {}^6H_{13/2}$ transition under 452 nm excitation of $CaLa_{1-x}SnNbO_7 : xDy^{3+}$ ($x = 0.01, 0.02, 0.03, 0.04$) are shown in Figure 3.19. All the decay curves can be fitted well with the single exponential decay function,

$$y = y_0 + Ae^{(-x/t)}$$

where y_0 and A are constants and t is the decay time. The lifetimes of $CaLa_{1-x}SnNbO_7 : xDy^{3+}$ ($x = 0.01, 0.02, 0.03, 0.04$) ${}^4F_{9/2} \rightarrow {}^6H_{13/2}$ transition are obtained as 0.814, 0.797, 0.759 and 0.746 ms respectively.

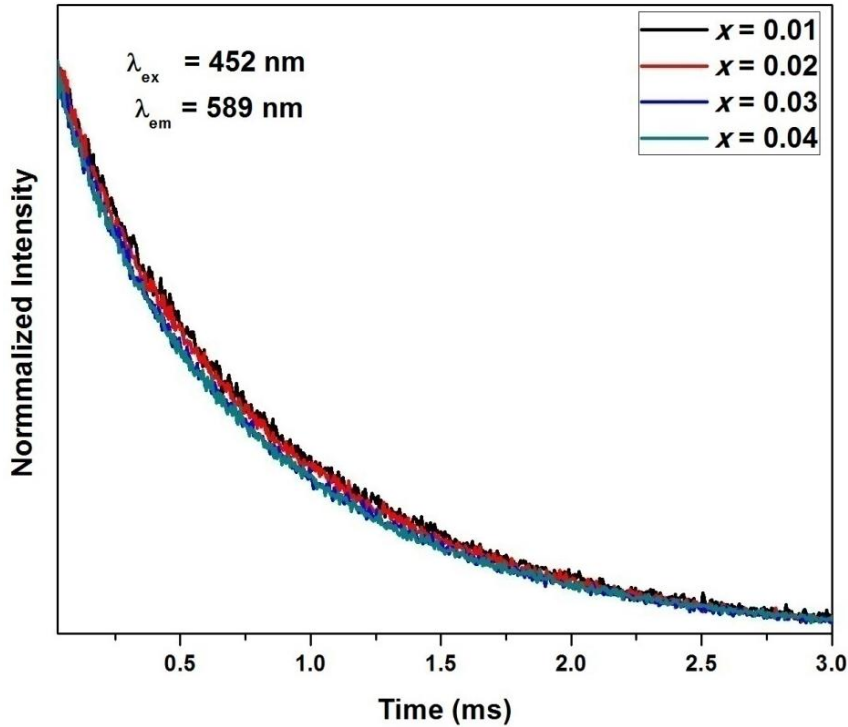


Figure 3.19 : Decay curves of $\text{CaLa}_{1-x}\text{SnNbO}_7 : x\text{Dy}^{3+}$ ($x = 0.01, 0.02, 0.03, 0.04$) under an excitation of 452 nm monitoring the emission at 589 nm.

3.3.4. The effect of Sr^{2+} ions substitution on the optical properties of

$\text{Ca}_{1-y}\text{Sr}_y\text{La}_{0.97}\text{SnNbO}_7 : 0.03 \text{Dy}^{3+}$ ($y = 0, 0.1, 0.2, 0.3$) samples.

The substitution of Ca^{2+} ions by the Sr^{2+} ions doesn't alter the crystalline lattice and it has some effect on the A-O_{8b} chains as Sr^{2+} ions are bigger compared to Ca^{2+} ions. Figure 3.20 presents the XRD patterns of $\text{Ca}_{1-y}\text{Sr}_y\text{La}_{0.97}\text{SnNbO}_7 : 0.03 \text{Dy}^{3+}$ ($y = 0, 0.1, 0.2, 0.3$) samples. The expansion of the crystal lattice as the cubic lattice parameter values increases from 10.5487 Å to 10.5693 Å with the increase in strontium substitution confirms the incorporation of Sr^{2+} ions into the lattice. Based on the valency and nature of ion, strontium is likely to occupy the calcium lattice site. Lattice parameters and unit cell volumes of $\text{Ca}_{1-y}\text{Sr}_y\text{La}_{0.97}\text{SnNbO}_7 : 0.03 \text{Dy}^{3+}$ ($y = 0, 0.1, 0.2, 0.3$) samples are given in Table 3.4.

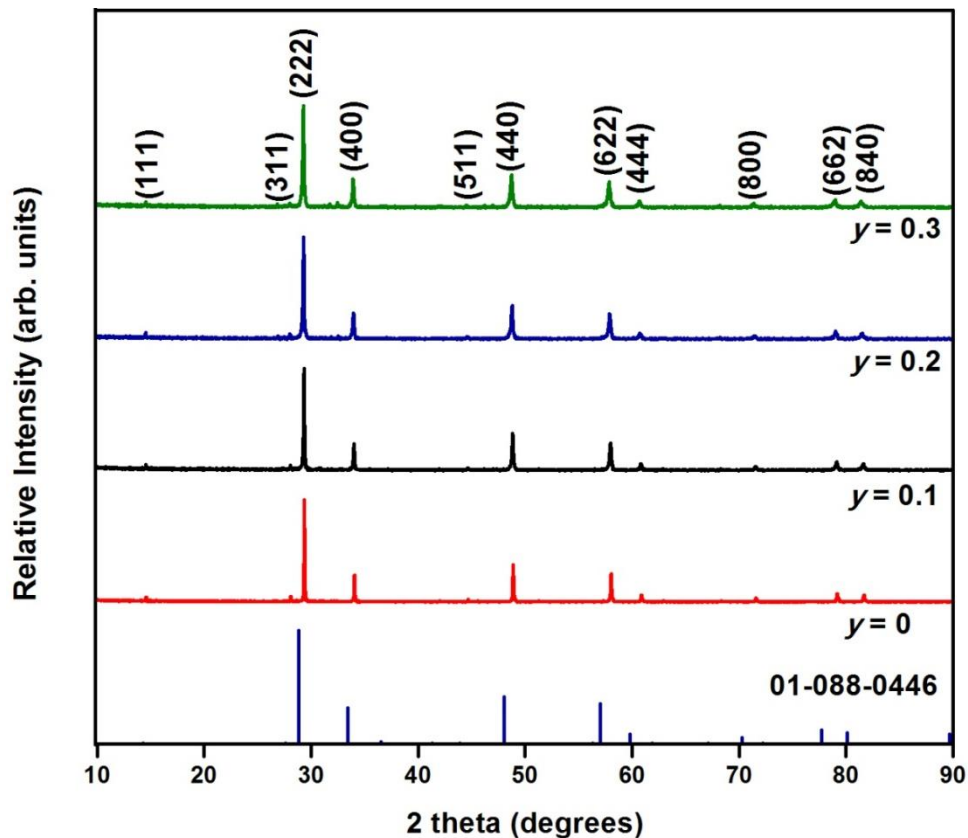


Figure 3.20 : Powder X-ray diffraction patterns of $Ca_{1-y}Sr_yLa_{0.97}SnNbO_7 : 0.03 Dy^{3+}$ ($y = 0, 0.1, 0.2, 0.3$) samples.

Table 3.4 : Lattice parameters and unit cell volumes of $Ca_{1-y}Sr_yLa_{0.97}SnNbO_7 : 0.03 Dy^{3+}$ ($y = 0, 0.1, 0.2, 0.3$) samples.

Composition	Lattice Parameters $a = b = c$ (Å)	Unit Cell Volume (Å) ³
$CaLa_{0.97}SnNbO_7 : 0.03 Dy^{3+}$	10.5429	1171.8722
$Ca_{0.9}Sr_{0.1}La_{0.97}SnNbO_7 : 0.03 Dy^{3+}$	10.5487	1173.8074
$Ca_{0.8}Sr_{0.2}La_{0.97}SnNbO_7 : 0.03 Dy^{3+}$	10.5561	1176.2794
$Ca_{0.7}Sr_{0.3}La_{0.97}SnNbO_7 : 0.03 Dy^{3+}$	10.5693	1180.6976

Scanning electron micrographs of $Ca_{1-y}Sr_yLa_{0.97}SnNbO_7 : 0.03 Dy^{3+}$ phosphor powders with varying Sr^{2+} concentrations ($y = 0.1, 0.2, 0.3$) are shown in Figure 3.21. Particle size is in the range of 0.5-1 μm .

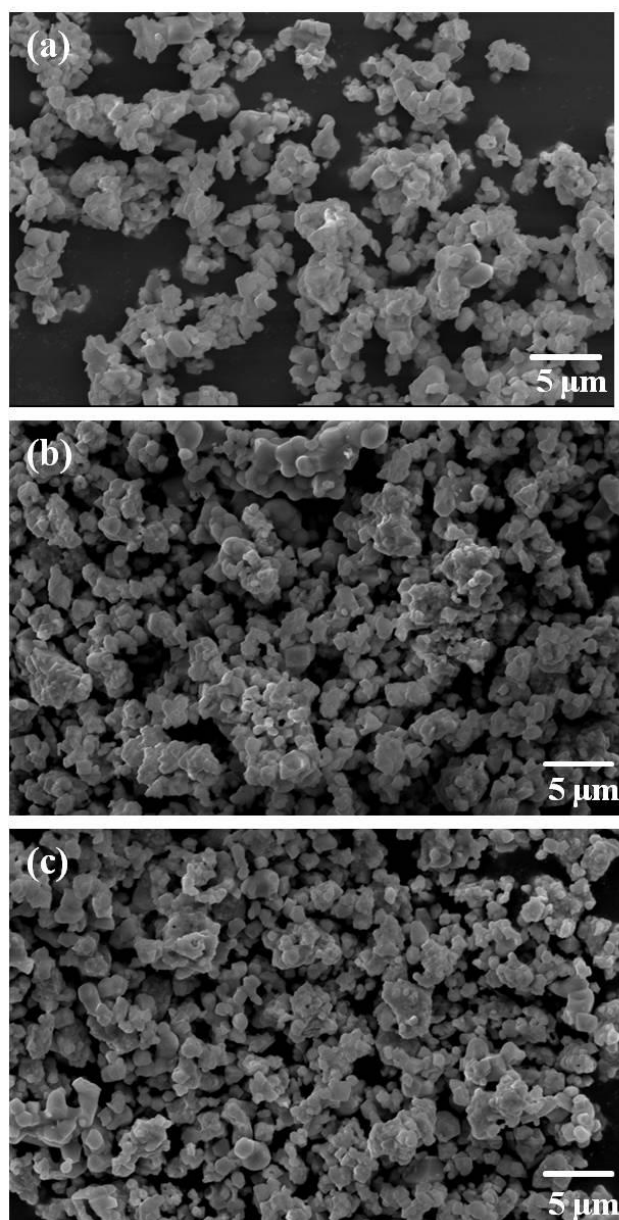


Figure 3.21 : Scanning electron micrographs of $Ca_{1-y}Sr_yLa_{0.97}SnNbO_7 : 0.03 Dy^{3+}$ phosphor powders with varying Sr^{2+} concentrations: (a) $y = 0.1$, (b) $y = 0.2$, (c) $y = 0.3$.

The quaternary pyrochlore system allows to modify the photoluminescence properties by aliovalent cation substitutions at A and B sites to introduce distortion and polarizability leading to enhance the luminescence properties.

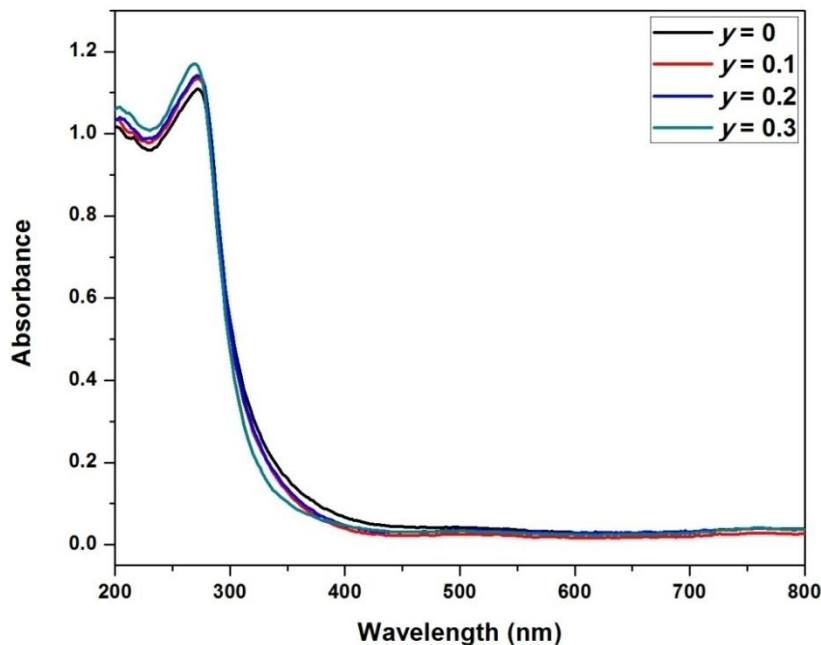


Figure 3.22 : UV-Visible absorption spectra of $Ca_{1-y}Sr_yLa_{0.97}SnNbO_7 : 0.03 Dy^{3+}$ ($y = 0, 0.1, 0.2, 0.3$) phosphor powders.

The UV-Visible absorption spectra of $Ca_{1-y}Sr_yLa_{0.97}SnNbO_7 : 0.03 Dy^{3+}$ ($y = 0, 0.1, 0.2, 0.3$) phosphor powders are shown in Figure 3.22. The absorption spectra of $Ca_{1-y}Sr_yLa_{0.97}SnNbO_7 : 0.03 Dy^{3+}$ exhibits a strong absorption band around 290 nm in the UV region. It is expected that these phosphors are excitable under both near UV and blue irradiation, which is one of the prerequisites for a phosphor material for pc WLEDs.

From the excitation spectra of $Ca_{1-y}Sr_yLa_{0.97}SnNbO_7 : 0.03 Dy^{3+}$ ($y = 0, 0.1, 0.2, 0.3$) for an emission at 589 nm shown in Figure 3.23, it is observed that f-f transition intensities are significantly improved due to increased lattice expansion by substitution of a bigger ion like Sr^{2+} leading to higher polarizability. [Mahesh *et al.* 2013] It is also further noticed that the CT band positions remains more or less same with the Sr^{2+} substitution because it has a comparable Pauling's electronegativity of Ca^{2+} (1 and 0.95).

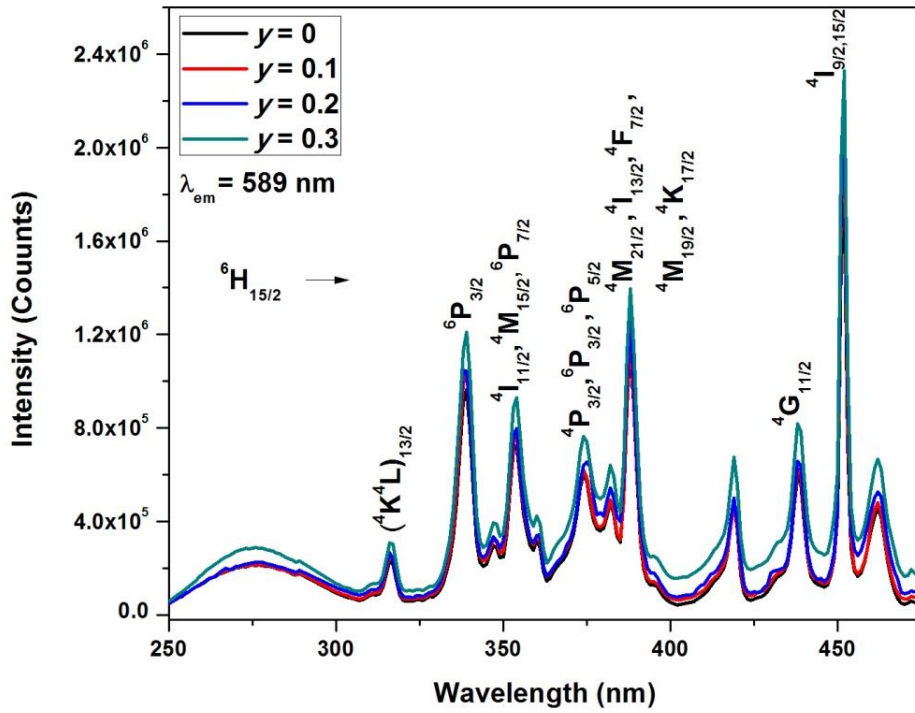


Figure 3.23 : Excitation spectra of $\text{Ca}_{1-y}\text{Sr}_y\text{La}_{0.97}\text{SnNbO}_7 : 0.03 \text{Dy}^{3+}$ ($y = 0, 0.1, 0.2, 0.3$) for an emission at 589 nm.

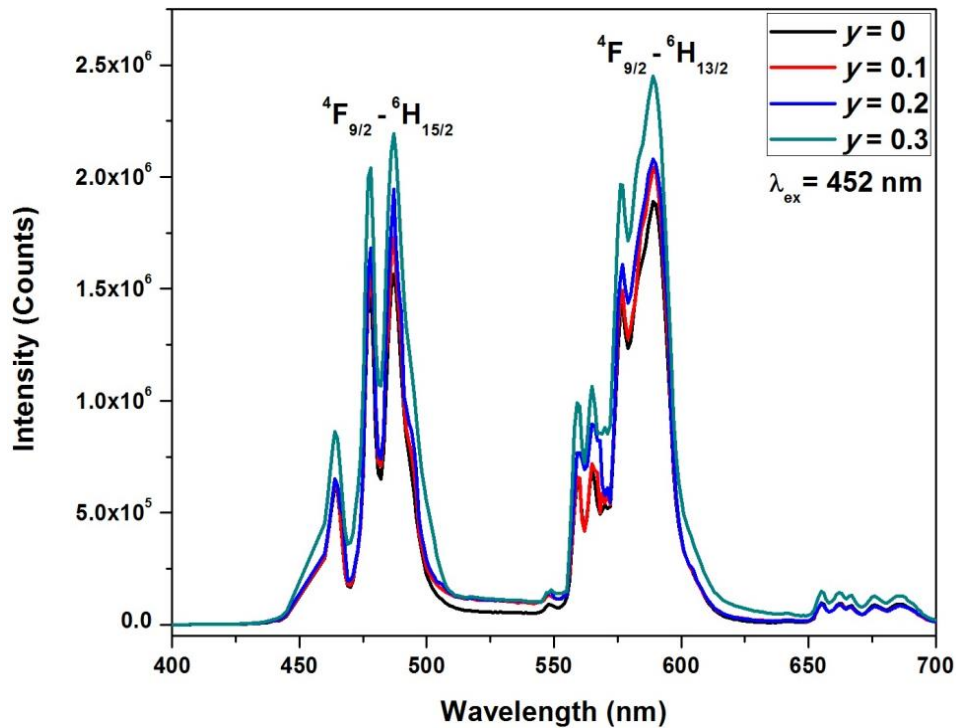


Figure 3.24 : Emission spectra of $\text{Ca}_{1-y}\text{Sr}_y\text{La}_{0.97}\text{SnNbO}_7 : 0.03 \text{Dy}^{3+}$ ($y = 0, 0.1, 0.2, 0.3$) samples under 452 nm excitation.

The emission spectra profiles of $\text{Ca}_{1-y}\text{Sr}_y\text{La}_{0.97}\text{SnNbO}_7 : 0.03 \text{Dy}^{3+}$ ($y = 0, 0.1, 0.2, 0.3$) samples under 452 nm excitation are similar with that of $\text{CaLa}_{1-x}\text{SnNbO}_7 : x\text{Dy}^{3+}$ ($x = 0.01, 0.02, 0.03, 0.04$), but emission intensities are improved with strontium substitution as shown in Figure 3.24. Figure 3.25 shows the variation in the luminescent intensities for the Sr^{2+} substituted compositions.

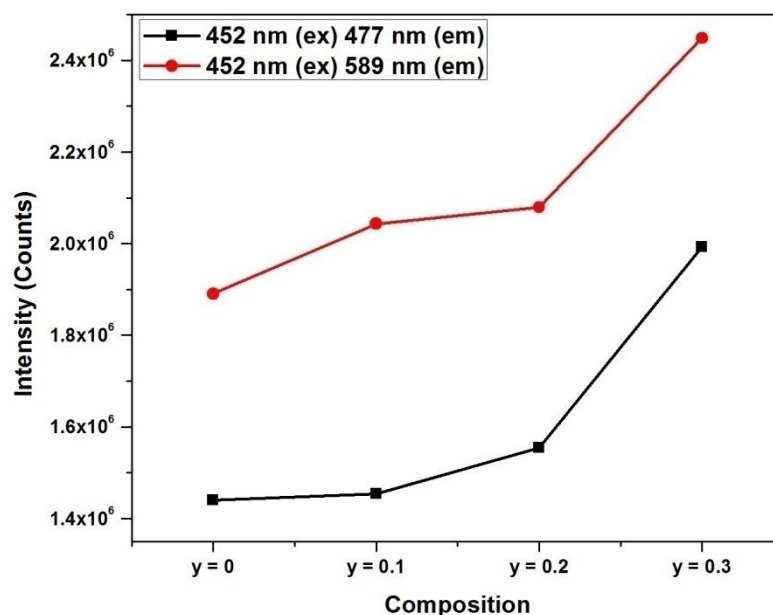


Figure 3.25 : Variation in the luminescent intensities of $\text{Ca}_{1-y}\text{Sr}_y\text{La}_{0.97}\text{SnNbO}_7 : 0.03 \text{Dy}^{3+}$ ($y = 0, 0.1, 0.2, 0.3$) samples under 452 nm excitation for the emissions at 477 nm (black line) and 589 nm (red line).

Table 3.5 : Y/B ratios and CIE values of $\text{Ca}_{1-y}\text{Sr}_y\text{La}_{0.97}\text{SnNbO}_7 : 0.03 \text{Dy}^{3+}$ ($y = 0, 0.1, 0.2, 0.3$) samples under 452 nm excitation wavelengths.

Composition	Y/B ratio	Color Co-ordinates (x, y)
$\text{CaLa}_{0.97}\text{SnNbO}_7 : 0.03 \text{Dy}^{3+}$	1.207	(0.384, 0.365)
$\text{Ca}_{0.9}\text{Sr}_{0.1}\text{La}_{0.97}\text{SnNbO}_7 : 0.03 \text{Dy}^{3+}$	1.185	(0.381, 0.373)
$\text{Ca}_{0.8}\text{Sr}_{0.2}\text{La}_{0.97}\text{SnNbO}_7 : 0.03 \text{Dy}^{3+}$	1.179	(0.343, 0.368)
$\text{Ca}_{0.7}\text{Sr}_{0.3}\text{La}_{0.97}\text{SnNbO}_7 : 0.03 \text{Dy}^{3+}$	1.116	(0.359, 0.391)

Y/B ratios and CIE values of $\text{Ca}_{1-y}\text{Sr}_y\text{La}_{0.97}\text{SnNbO}_7 : 0.03 \text{Dy}^{3+}$ ($y = 0, 0.1, 0.2, 0.3$) samples under 452 excitation wavelengths are given in Table 3.5. The Y/B ratio decreases slightly with Sr substitution. This ratio is also considered as asymmetric ratio which mainly depends on the distortion of the Dy^{3+} ions in the lattice. However, on Sr^{2+} ion substitution for Ca improves the symmetry at the A site because of increasing the average ionic radius of A site against Dy^{3+} ions substitution.

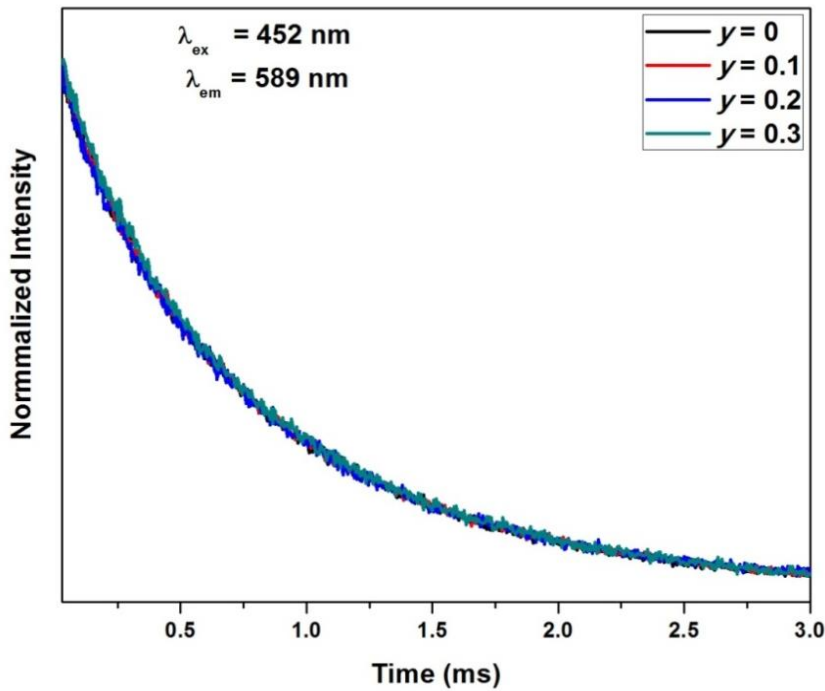


Figure 3.26 : Decay curves of $\text{Ca}_{1-y}\text{Sr}_y\text{La}_{0.97}\text{SnNbO}_7 : 0.03 \text{Dy}^{3+}$ ($y = 0, 0.1, 0.2, 0.3$) samples under an excitation of 452 nm monitoring the emission at 589 nm.

From the photoluminescence decay curve of $\text{Ca}_{1-y}\text{Sr}_y\text{La}_{0.97}\text{SnNbO}_7 : 0.03 \text{Dy}^{3+}$ ($y = 0, 0.1, 0.2, 0.3$) shown in Figure 3.26 the lifetimes of ${}^4\text{F}_{9/2} \rightarrow {}^6\text{H}_{13/2}$ transition under 452 nm excitation are obtained as 0.760, 0.759, 0.755, and 0.750 ms, respectively. The improvement in the luminescence intensity on Sr substitution is mainly due to the increased polarizability and blocking the cross relaxation between the Dy^{3+} ions due to incorporation of the bigger Sr^{2+} ion. Hence the radiation probabilities remain more or less the same without losing much of the transfer energy due to exchange interaction. Thus, there is not much change in the lifetime values with Sr substitution.

3.4. Conclusions

In the present study, new white light emitting single phase phosphors based on a quaternary pyrochlore system $CaLn_{0.97}SnNbO_7 : 0.03 Dy^{3+}$ ($Ln = La, Gd, Lu, Y$), $CaLa_{1-x}SnNbO_7 : xDy^{3+}$ ($x = 0.01, 0.02, 0.03, 0.04$) and $Ca_{1-y}Sr_yLa_{0.97}SnNbO_7 : 0.03 Dy^{3+}$ ($y = 0.1, 0.2, 0.3$) were developed successfully. The photoluminescence studies indicate that the phosphor material can be easily excited by the emission outputs of UV and blue LED chip and the phosphor samples exhibit the characteristic f-f transitions of Dy^{3+} at 477 nm, 487 nm and 589 nm assigned to the forced electric dipole transition of ${}^4F_{9/2} \rightarrow {}^6H_{13/2}$ and the magnetic dipole transition of ${}^4F_{9/2} \rightarrow {}^6H_{15/2}$ respectively with excellent chromaticity coordinates. The variation of the emission intensity upon the different excitation wavelengths for the optimised sample at $x = 0.03$ was also studied and the asymmetric ratio and Commission Internationale de l'Eclairage color coordinates were in good agreement with the standard chromaticity coordinates of white light (0.33, 0.33). The photoluminescence properties are enhanced by using Sr^{2+} ions along with Ca^{2+} in the Pyrochlore A site, though the CT band position does not show any significant change. Accounting for the good morphology, excellent photoluminescence characteristics, the obtained phosphors have potential applications for designing phosphor converted (pc) white-light emitting materials.

Chapter 4

Photoluminescent Properties of $\text{La}_{3-x}\text{MO}_7 : x\text{Dy}^{3+}$ (M = Sb, Ta, Nb) phosphors

Abstract

New white phosphor materials Dy^{3+} doped lanthanide based antimonates, tantalates and niobates of the general formula $\text{La}_{3-x}\text{MO}_7$ ($M = \text{Sb}, \text{Ta}, \text{Nb}$) were prepared by a high temperature solid state reaction. The crystalline structure and the spectra of the as-prepared phosphor samples were characterised by powder X-ray diffraction and photoluminescence measurements, respectively. Powder X-ray diffraction analysis confirms orthorhombic CmCm phase for all the Dy^{3+} doped phosphor samples. The luminescence properties such as photoluminescence excitation under ultraviolet and blue wavelengths and emissions in the visible region and the dependence of luminescence intensity on the Dy^{3+} doping levels are investigated. The luminescence properties have a strong dependence on the nature of the M atom and the Dy^{3+} doping levels. The yellow and blue emissions upon UV excitation resulted from the forced electric dipole transition of ${}^4\text{F}_{9/2} \rightarrow {}^6\text{H}_{13/2}$ and the magnetic dipole transition of ${}^4\text{F}_{9/2} \rightarrow {}^6\text{H}_{15/2}$ respectively. Therefore, Dy^{3+} doped $\text{La}_{3-x}\text{MO}_7$ phosphors have potential application as a single-phase white-light emitting phosphors under near UV excitation.

4.1 Introduction

During the past few decades, with the emerging energy crisis, rare-earth (RE) ions doped inorganic phosphors has been gaining extensive attention owing to their rich luminescence efficiency, good stability and a strong excitation band in the blue or UV region and finds potential applications in plasma display panels, optical temperature sensors, white light-emitting diodes, and field-emission displays (FEDs). [Ronda C.2008, Justel *et al.* 2008] In the initial stages of phosphor technology, sulphide, nitride and oxynitride phosphors were largely used. The sulphide phosphors decompose readily and emit sulphide gas which is very harmful to the environment. Moreover, it deteriorates the cathodes, thereby lowering the luminous efficiency of phosphors. Rare earth ions doped oxide phosphors are studied keeping in view of its inherent high stability, luminescence efficiency, environment friendliness, ease of preparation and low cost. Research groups across the globe have been speculating on the white light generation from a single phase host due to tunable correlated color temperature (CCT), high color rendering index (CRI), and pure Commission Internationale de l'Eclairage (CIE) chromaticity coordinates, for application in phosphor converted white light-emitting diodes (pc-WLEDs). Single phase host lattices avert the re-absorption of emission colours produced by the red–green–blue (RGB) tricolor phosphors. White light generation in a single-phase host can be realized by four main methods: (1) singly doping a rare earth ion; (2) the combination of multiple rare earth ions; (3) co-doping ion pairs based on the energy transfer process; (4) defect-induced white light, [Shang *et al.* 2014] Among the various approaches of white light generation in a single phase host, singly doping a rare earth ion is still the simplest and most straightforward method.

Dysprosium has $4f^9$ configuration and trivalent dysprosium (Dy^{3+}) ion is an excellent activator and have wide applications in mercury free lamps, field emission displays, and plasma display panels. Dy^{3+} ion exhibits two main emissions in the visible region, the yellow (570-600 nm) and blue (470-500 nm) emission bands are assigned to the forbidden electric dipole transition of ${}^4\text{F}_{9/2} \rightarrow {}^6\text{H}_{13/2}$ and the allowed magnetic dipole transition of ${}^4\text{F}_{9/2} \rightarrow {}^6\text{H}_{15/2}$ respectively under n-UV or blue excitation. [Blasse G 1994] Near white light emission in Dy^{3+} doped luminescent materials is obtained by controlling the yellow to blue (Y/B) intensity ratio to a desired level. The above Dy^{3+} ion transitions mainly depends on the site symmetry, host composition, excitation wavelength and doping concentration of Dy^{3+} at the luminescent centers. [Liu *et al.* 2012, Deng *et al.*

2014] Thus, the Y/B ratio of Dy^{3+} emission is greatly influenced by the covalent effect between Dy^{3+} and O^{2-} and it inversely relates with Z/r , where Z is the charge and r the ionic radius, or electronegativity of the surrounding element M in the ternary oxide Dy-O-M. [Su *et al.* 1993] The intra-configurational f-f transitions of RE^{3+} ions have weak excitation levels on account of forbidden parity selection rules. Therefore, the luminescence efficiency of RE^{3+} ions can be greatly improved by transferring the energy from a foreign species to RE^{3+} ions. [Naidu *et al.* 2012] Thus, there is great demand for discovering white light emission in Dy^{3+} doped phosphors based on a single luminescent center.

In this work, ternary rare earth antimonates, tantalates and niobates with the general formula $La_{3-x}MO_7$ ($M = Sb, Ta, Nb$) were synthesized. The hosts have high chemical stability, lattice stiffness, and thermal stability. This kind of structures allows a wide variety of cation substitutions at the M sites including rare earth ions in the crystal lattice with mixed valences such as 3^+ and 4^+ or 2^+ and 5^+ together with oxygen vacancies. The ternary rare earth doped compounds generally have a fluorite structure (AO_2), $M_4^{4+}O_8$, if the four tetravalent metal ions M^{4+} in the A and B sites are replaced by three trivalent ions (La) and one pentavalent ion (Sb, Ta, Nb), one oxide vacancy is formed per fluorite cell. Due to the significant differences in radii between the La^{3+} and M^{5+} (Sb, Ta, Nb) ions, cation ordering occurs on the metal sites and the oxide-vacancy ordering on the anion sites. [Subramanian *et al.* 1983] Pyrochlore and weberite, which are superstructures or derivatives of the fluorite structures are anion-deficient fluorite-related structures ($A_2B_2O_7$), which maintains the closed-packed cation layers as in the fluorite structure. In the present study, $La_{2.95}MO_7 : 0.050 Dy^{3+}$ ($M = Sb, Ta, Nb$) and a series of $La_{3-x}SbO_7 : x Dy^{3+}$ ($x = 0.025, 0.050, 0.075, 0.100$) phosphor samples were developed by a ceramic high temperature route and their excitation and emission properties were investigated.

4.2 Experimental section

4.2.1 Synthesis

Preparation of $La_{2.95}MO_7 : 0.050 Dy^{3+}$ ($M = Sb, Ta, Nb$) and $La_{3-x}SbO_7 : x Dy^{3+}$ ($x = 0, 0.025, 0.050, 0.075, 0.100$) samples:

The phosphors, $La_{2.95}MO_7 : 0.050 Dy^{3+}$ ($M = Sb, Ta, Nb$) and a series of $La_{3-x}SbO_7 : x Dy^{3+}$ ($x = 0, 0.025, 0.050, 0.075, 0.100$) phosphor samples were synthesized by the conventional high temperature ceramic route by taking La_2O_3 , Sb_2O_5 , Ta_2O_5 , Nb_2O_5 , Dy_2O_3 (All chemicals are from Sigma Aldrich with 99.99% purity) as the starting raw materials. The right stoichiometric amounts of these chemicals were taken and then mixed nicely in an agate mortar using acetone medium. After homogeneous mixing the product was kept for drying in an air oven maintained at $100^{\circ}C$ temperature. The above process of mixing and drying was done many times to get a homogeneous product. The obtained product was made into a pellet and calcined twice at $1400^{\circ}C$ for 6 h on an alumina plate in an electrically heated furnace with an intermittent powdering to obtain the final single phase sample. The calcined pellet was made into a fine powder for further characterizations.

4.2.2 Characterisation techniques

The crystalline structure of the samples was verified by the X-ray powder diffraction (XRD) analysis using powder X-ray diffractometer (X'Pert Pro PANalytical). The diffraction patterns were recorded in the 2θ scan range from 10° to 90° with a step size of 0.016° with the system operating at 40 kV/30 mA with a Ni filtered Cu-K α radiation ($\lambda=0.15406$ nm). The photoluminescence excitation and emission measurements were made on a Fluorolog HORIBA fluorescence spectrophotometer with a Xenon lamp (450 W) as the excitation source.

4.3 Results and discussion

4.3.1 Powder X-ray diffraction analysis

Powder X-ray diffraction patterns of $La_{2.95}SbO_7 : 0.050 Dy^{3+}$, $La_{2.95}TaO_7 : 0.050 Dy^{3+}$ and $La_{2.95}NbO_7 : 0.050 Dy^{3+}$ phosphors are shown in Figure 4.1, Figure 4.2 and Figure 4.3 respectively. All the diffraction peaks of these samples can be assigned to

orthorhombic phase with a space group $CmCm(63)$ they match well with the standard values of PDF card (no. 01-071-1345 and 01-073-8085).

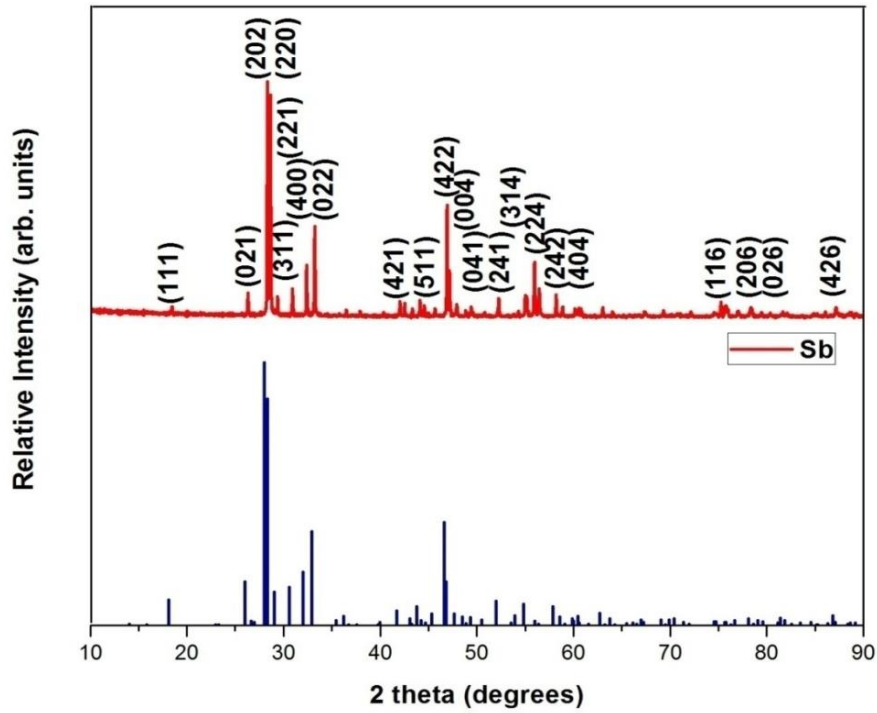


Figure 4.1 : Powder X-ray diffraction patterns of $La_{2.95}SbO_7: 0.050 Dy^{3+}$.

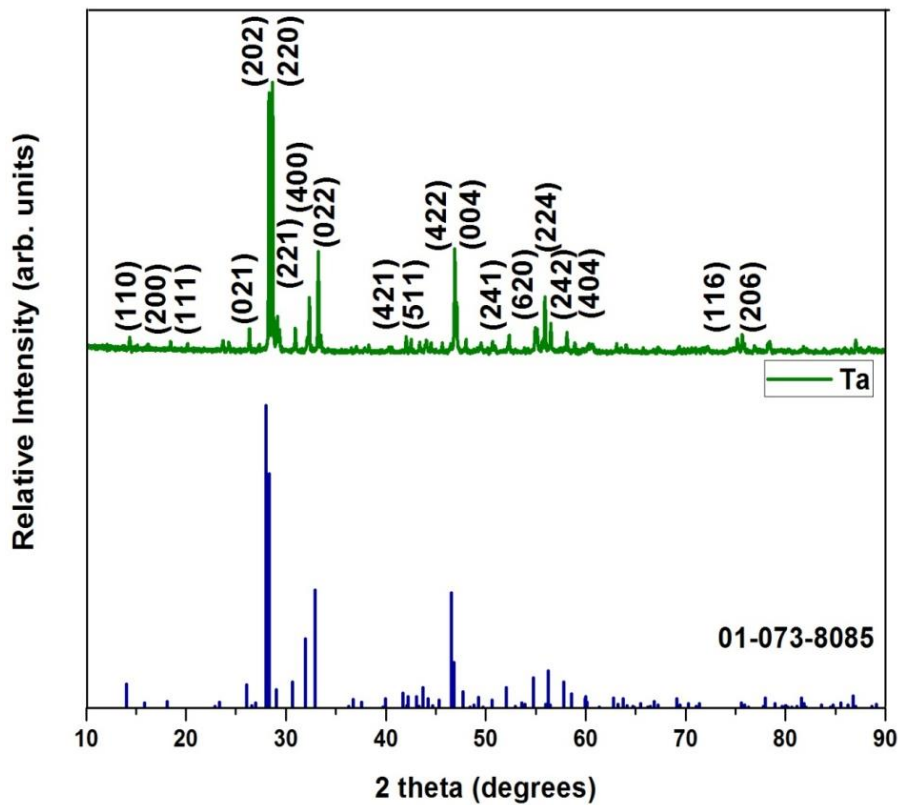


Figure 4.2 : Powder X-ray diffraction patterns of $La_{2.95}TaO_7: 0.050 Dy^{3+}$.

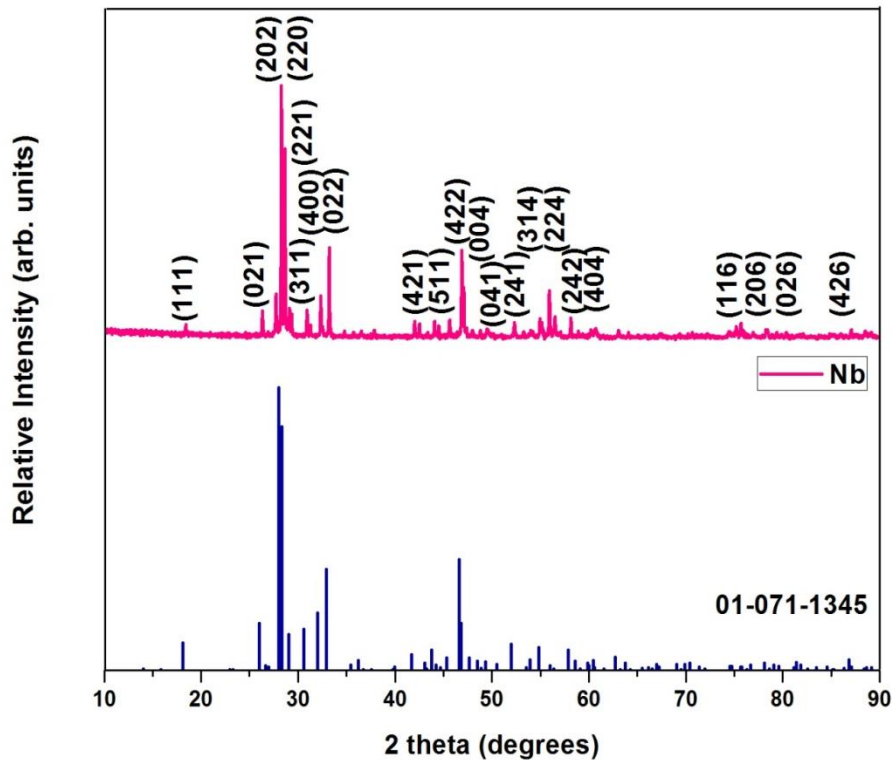


Figure 4.3 : Powder X-ray diffraction patterns of $La_{2.95}NbO_7: 0.050 Dy^{3+}$.

In this family of weberites, the MO_6 octahedra are corner linked to each other and form chains of MO_6 octahedra with parallel chains of LnO_8 distorted cubes. Thus in this structure there are equal numbers of VI and VIII coordinated cations in an ordered $BO_6 - AO_8$ layer arrangement. [Francis *et al.* 2016, Wang *et al.* 2014] The VIII coordinated and VII coordinated cations can also be realized in the case of orthorhombic structures where the possibility that the LnI and LnII cations may be of different types. The cation ordering in this specimen may not be complete. [Francis *et al.* 2012] The strong and sharp diffraction peaks indicate that samples are highly crystalline and no additional peaks from impurities were observed with incorporation of Dy^{3+} ions. Considering the matching ionic radius and coordination number of the ions, in all the three cases one expects the Dy^{3+} ions are incorporated to the La^{3+} sites. [Shannon R. D. 1976]

4.3.2 Photoluminescence Studies

The photoluminescence properties of all samples have been carefully studied and the photoluminescence excitation spectra of the samples $\text{La}_{2.95}\text{MO}_7 : 0.050 \text{Dy}^{3+}$, ($M = \text{Sb}, \text{Ta}, \text{Nb}$) for an emission at 479 nm and 489 nm are given in Figures 4.4 and 4.5 respectively.

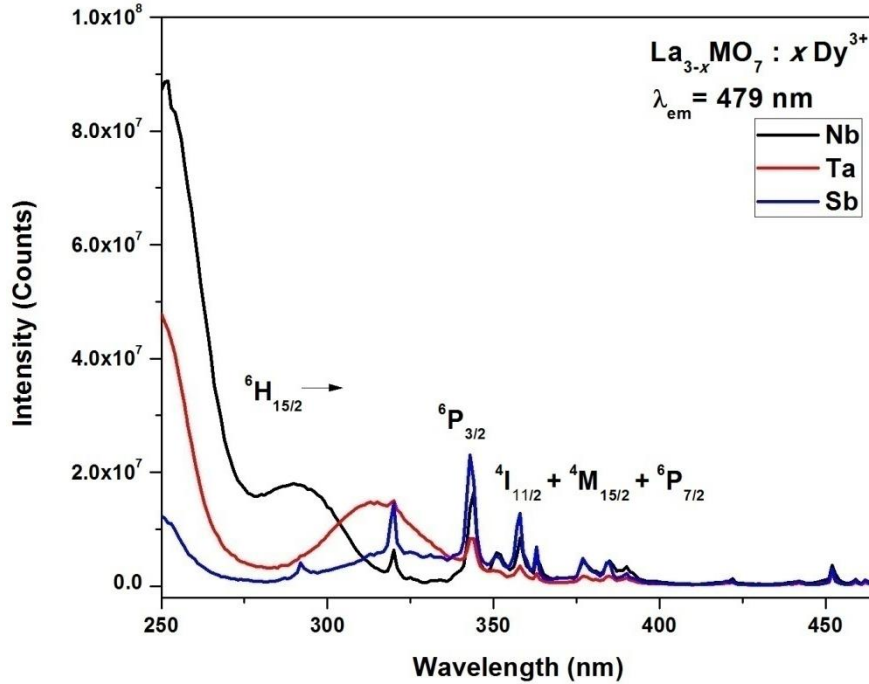


Figure 4.4 : Excitation spectra of $\text{La}_{2.95}\text{MO}_7 : 0.050 \text{Dy}^{3+}$ ($M = \text{Sb}, \text{Ta}, \text{Nb}$) for an emission at 479 nm.

A broad band from 250 nm to 300 nm is assigned to the charge transfer transition from the oxygen to the metal. [Yin *et al.* 2012] This broad CT band in the excitation spectra results from the resultant effect of $\text{O}_{2p} \rightarrow \text{Dy}_{4f}$ and $\text{O}_{2p} \rightarrow \text{M}_{4d}$ CT transitions. The sharp and intense characteristic absorption lines in the UV region and blue region beyond CT band owing to the intra-configurational f-f transitions of Dy^{3+} peaks at 320 nm (${}^6\text{H}_{15/2} \rightarrow {}^6\text{P}_{3/2}$), 344 nm (${}^6\text{H}_{15/2} \rightarrow {}^6\text{P}_{3/2}$), 358 nm (${}^6\text{H}_{15/2} \rightarrow {}^4\text{I}_{11/2} + {}^4\text{M}_{15/2} + {}^6\text{P}_{7/2}$), 363 nm (${}^6\text{H}_{15/2} \rightarrow {}^6\text{P}_{9/2}$), 377 nm (${}^6\text{H}_{15/2} \rightarrow {}^4\text{P}_{3/2} + {}^6\text{P}_{3/2} + {}^6\text{P}_{5/2}$), 385 nm (${}^6\text{H}_{15/2} \rightarrow {}^4\text{M}_{21/2} + {}^4\text{I}_{13/2} + {}^4\text{F}_{7/2} + {}^4\text{M}_{19/2} + {}^4\text{K}_{17/2}$) and 452 nm (${}^6\text{H}_{15/2} \rightarrow {}^4\text{I}_{9/2} + {}^4\text{I}_{15/2}$), which are attributed to the ground state of ${}^6\text{H}_{15/2}$ to the various excited states of $4f^9$ electronic configurations of the Dy^{3+} ions. The intensities of the f-f transitions are more stronger than the charge transfer band for the antimonate and the niobate samples. The tantalate sample has an intense and broad charge transfer band in the near UV region than the antimonate and the

niobate samples. However, the tantalate sample have very weak excitation spectra compared with the other two systems. The excitation wavelengths matches to the emission of the blue LED chip and hence these phosphor material can be easily excited by the electroluminescence of the blue LED chip for developing phosphor converted WLEDs.

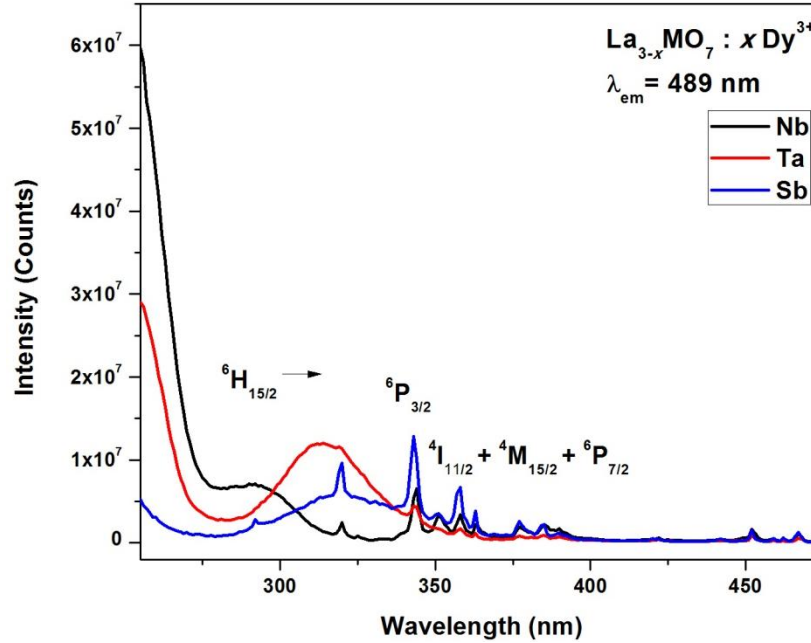


Figure 4.5 : Excitation spectra of $\text{La}_{2.95}\text{MO}_7: 0.050 \text{Dy}^{3+}$ ($M = \text{Sb}, \text{Ta}, \text{Nb}$) for an emission at 489 nm.

The photoluminescence emission spectra of $\text{La}_{2.95}\text{MO}_7: 0.050 \text{Dy}^{3+}$ ($M = \text{Sb}, \text{Ta}, \text{Nb}$) samples under an excitation of 344 nm, 358 nm and 377 nm are given in Figure 4.6, Figure 4.7 and Figure 4.8 respectively. The Dy^{3+} ions emits in the visible and near infrared regions of the spectrum due to the intraionic transitions from the $^4\text{F}_{9/2}$ excited state to the $^6\text{H}_{15/2}$ ground state and the $^6\text{H}_{13/2, 11/2, 9/2}$ levels under ultraviolet excitation. The yellow and blue emissions are attributed to the forced electric dipole (ED) transition of $^4\text{F}_{9/2} \rightarrow ^6\text{H}_{13/2}$ and the magnetic dipole (MD) transition of $^4\text{F}_{9/2} \rightarrow ^6\text{H}_{15/2}$ respectively. [Blasse G 1979] For Dy^{3+} ions located at a low symmetry local site and without an inversion center, the $^4\text{F}_{9/2} \rightarrow ^6\text{H}_{13/2}$ transition is dominant and at high symmetry sites with an inversion center a higher intensity of the $^4\text{F}_{9/2} \rightarrow ^6\text{H}_{15/2}$ transition is observed in comparison with the intensity of the yellow emission. [Soares *et al.* 2011] Both the transitions are of comparable intensity leading to a small deviation from inversion symmetry. Upon all the excitation wavelengths, the $\text{La}_{2.95}\text{MO}_7: 0.050 \text{Dy}^{3+}$ ($M = \text{Sb}, \text{Ta}, \text{Nb}$) phosphors show the characteristic blue yellow luminescence of Dy^{3+} .

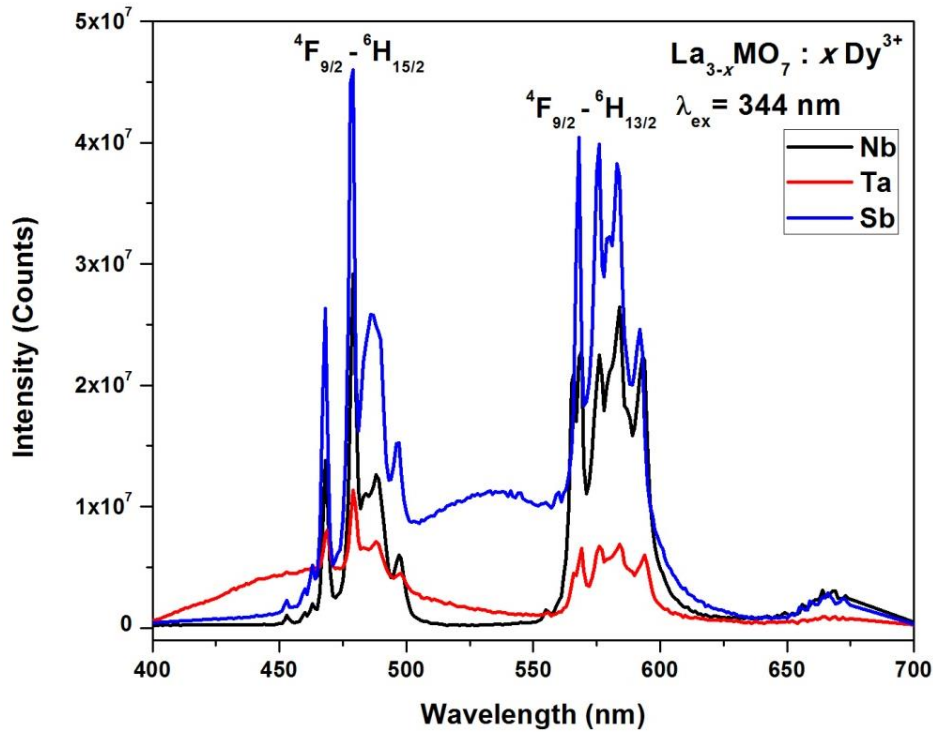


Figure 4.6 : Emission spectra of $La_{2.95}MO_7: 0.050 Dy^{3+}$ ($M = Sb, Ta, Nb$) under 344 nm excitation.

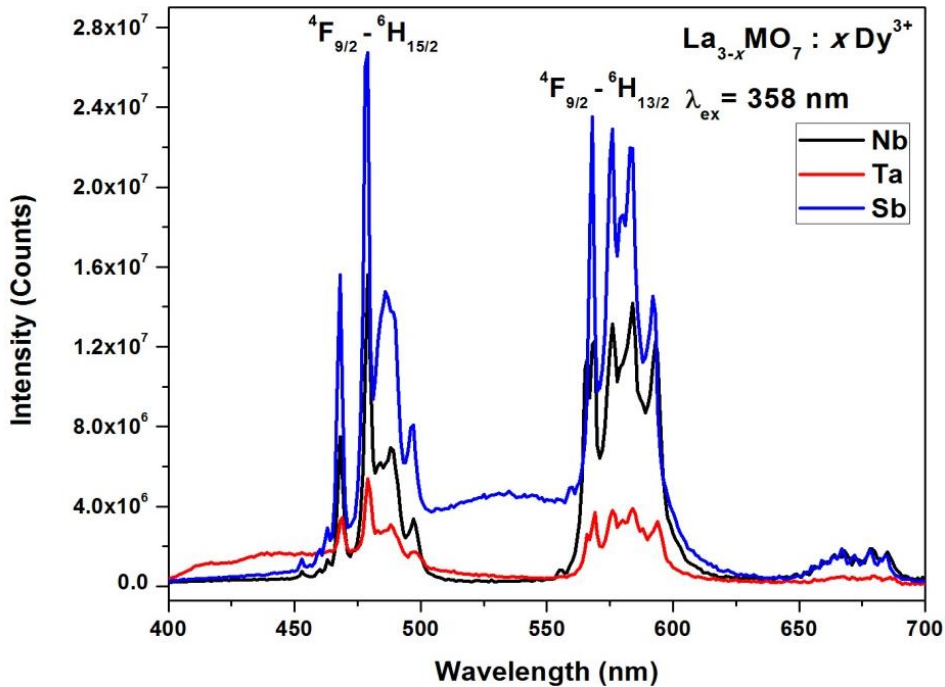


Figure 4.7 : Emission spectra of $La_{2.95}MO_7: 0.050 Dy^{3+}$ ($M = Sb, Ta, Nb$) under 358 nm excitation.

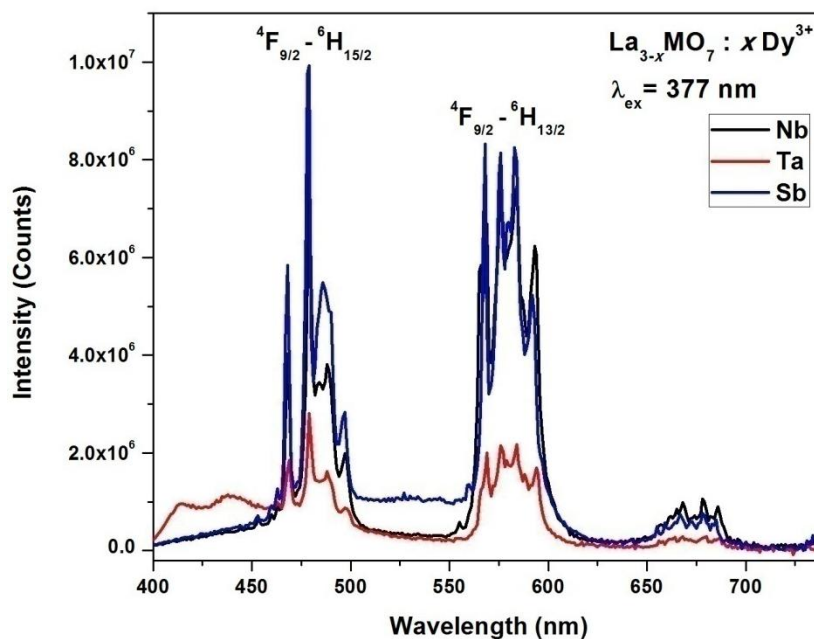


Figure 4.8 : Emission spectra of $La_{2.95}MO_7 : 0.050 Dy^{3+}$ ($M = Sb, Ta, Nb$) under 377 nm excitation.

The emission profiles of all the phosphor samples are similar in shape under the various excitation wavelengths but only change in the band intensity. White light is obtained by the mixing of the complimentary blue and the yellow emission bands. The antimonate samples exhibited better luminescent properties and further studies are confined to this system.

4.3.3. The effect of Dy^{3+} ions doping on the optical properties of $La_{3-x}SbO_7 : x Dy^{3+}$ ($x = 0, 0.025, 0.050, 0.075, 0.100$) samples.

Powder X-ray diffraction patterns of $La_{3-x}SbO_7 : x Dy^{3+}$ ($x = 0, 0.025, 0.050, 0.075, 0.100$) samples are given in Figure 4.9 reveal phase purity of all the samples and no additional peaks of other phases from impurities were detected, indicating the Dy^{3+} ions have been effectively incorporated into the La_3SbO_7 host lattice. Generally the impurity ions always take the place of the ions of similar radii and the same valence. The substitution of La^{3+} ions (ionic radius : 0.116 nm, CN = 8) by the Dy^{3+} ions (ionic radius : 0.1027 nm, CN = 8) results in lattice contraction and it is clearly evidenced by the shift of the diffraction peaks of $La_{3-x}SbO_7 : x Dy^{3+}$ ($x = 0, 0.025, 0.050, 0.075, 0.100$) towards the higher 2θ angle side with the increase in the Dy^{3+} ions concentration and is depicted in Figure 4.10.

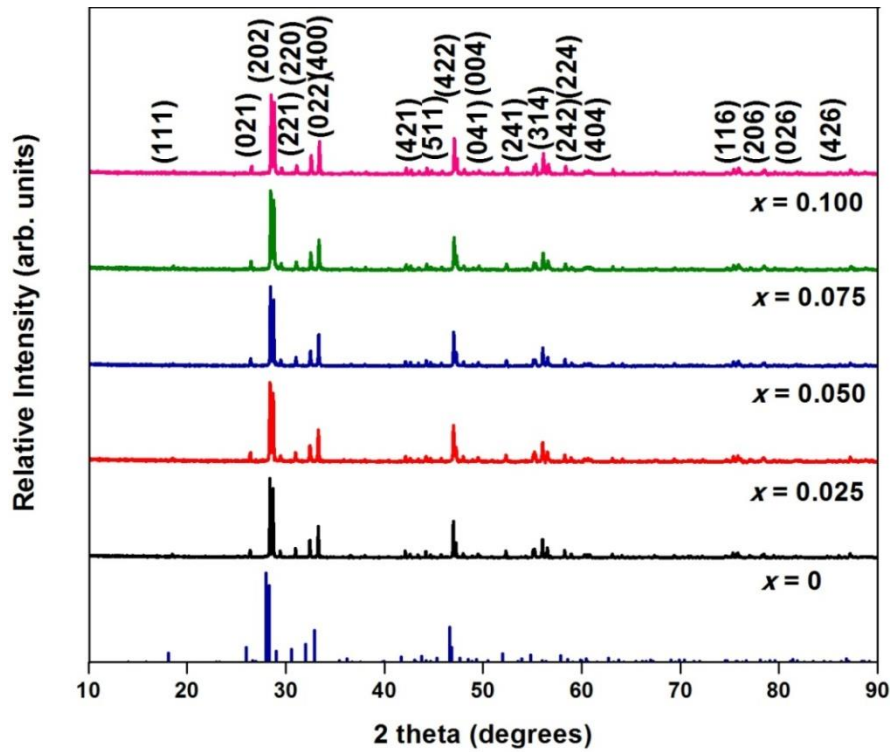


Figure 4.9: Powder X-ray diffraction patterns of $La_{3-x}SbO_7 : x Dy^{3+}$ ($x = 0, 0.025, 0.050, 0.075, 0.100$) samples.

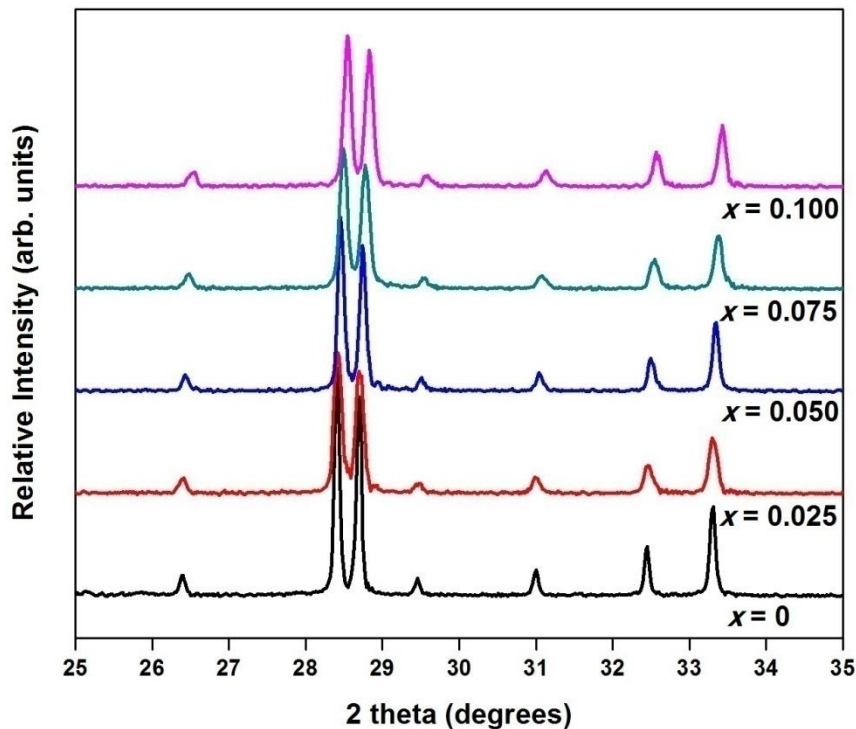


Figure 4.10: Enlarged view of the (202) and (220) diffraction peaks of $La_{3-x}SbO_7 : x Dy^{3+}$ ($x = 0, 0.025, 0.050, 0.075, 0.100$) showing the shift of the diffraction peaks towards the higher 2θ angle side with increasing concentration of Dy^{3+} ions.

The excitation spectra of $\text{La}_{3-x}\text{SbO}_7 : x\text{Dy}^{3+}$ ($x = 0, 0.025, 0.050, 0.075, 0.100$) for an emission at 479 nm and 489 nm are shown in Figure 4.11 and Figure 4.12 respectively.

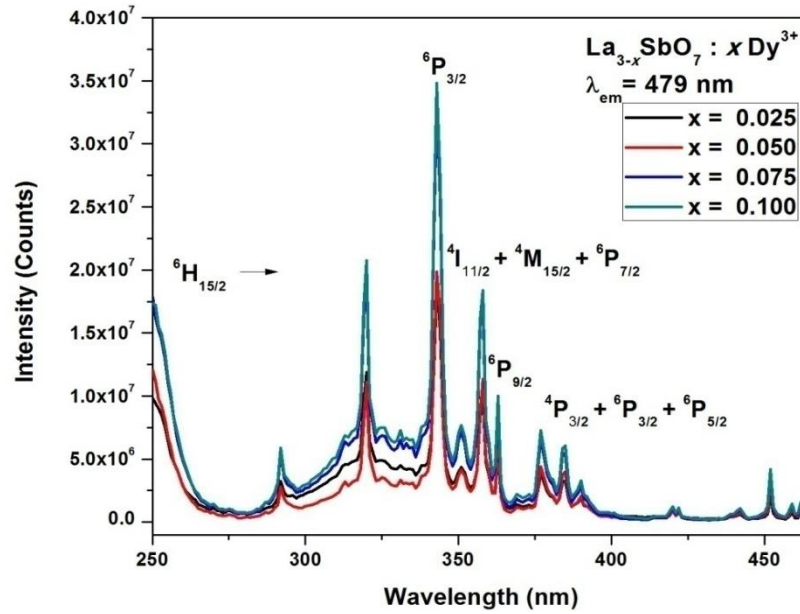


Figure 4.11 : Excitation spectra of $\text{La}_{3-x}\text{SbO}_7 : x\text{Dy}^{3+}$ ($x = 0.025, 0.050, 0.075, 0.100$) for an emission at 479 nm.

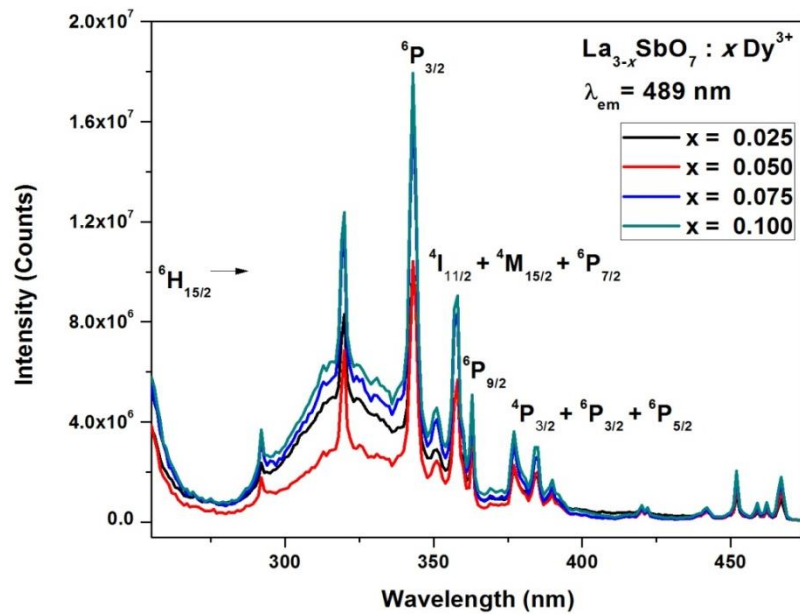


Figure 4.12 : Excitation spectra of $\text{La}_{3-x}\text{SbO}_7 : x\text{Dy}^{3+}$ ($x = 0.025, 0.050, 0.075, 0.100$) for an emission at 489 nm.

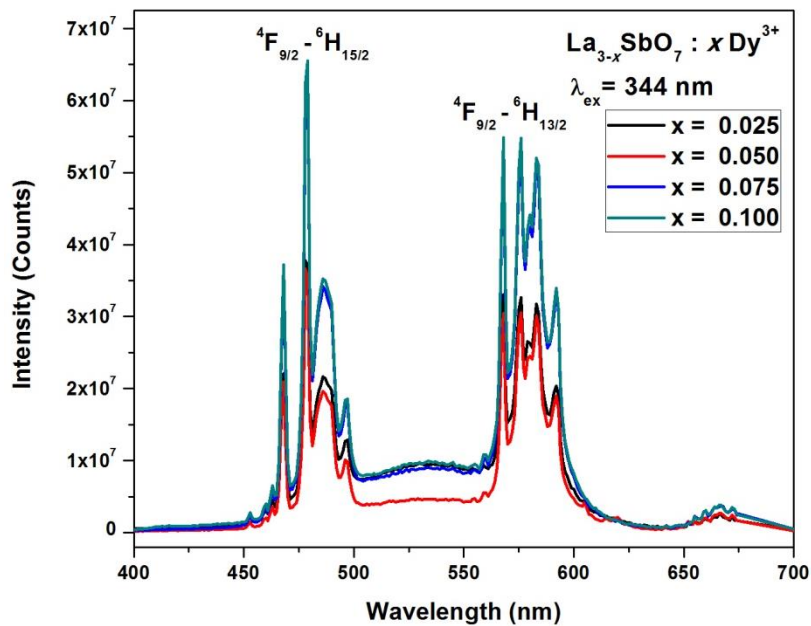


Figure 4.13 : Emission spectra of $La_{3-x}SbO_7 : x Dy^{3+}$ ($x = 0.025, 0.050, 0.075, 0.100$) under 344 nm excitation.

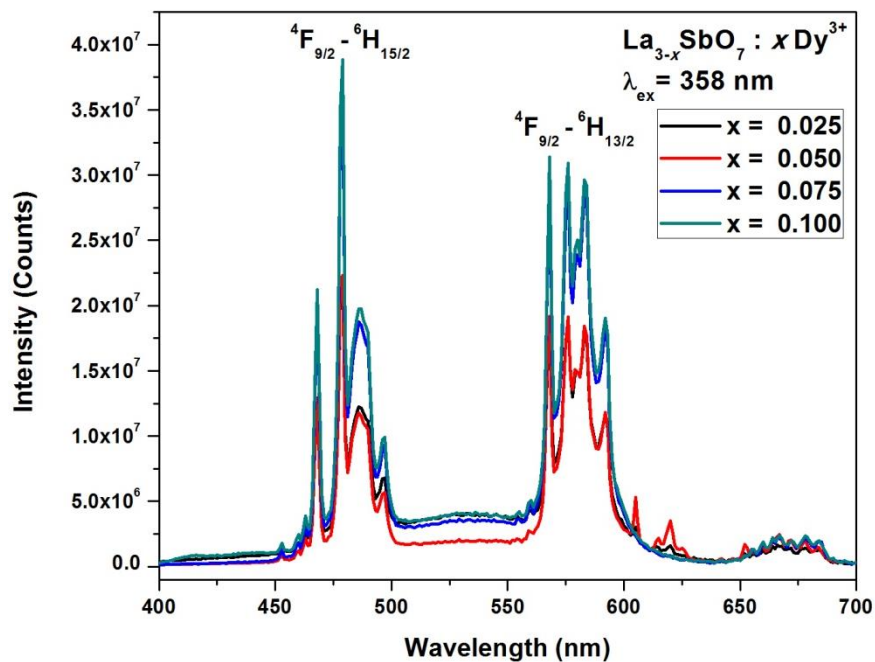


Figure 4.14 : Emission spectra of $La_{3-x}SbO_7 : x Dy^{3+}$ ($x = 0.025, 0.050, 0.075, 0.100$) under 358 nm excitation.

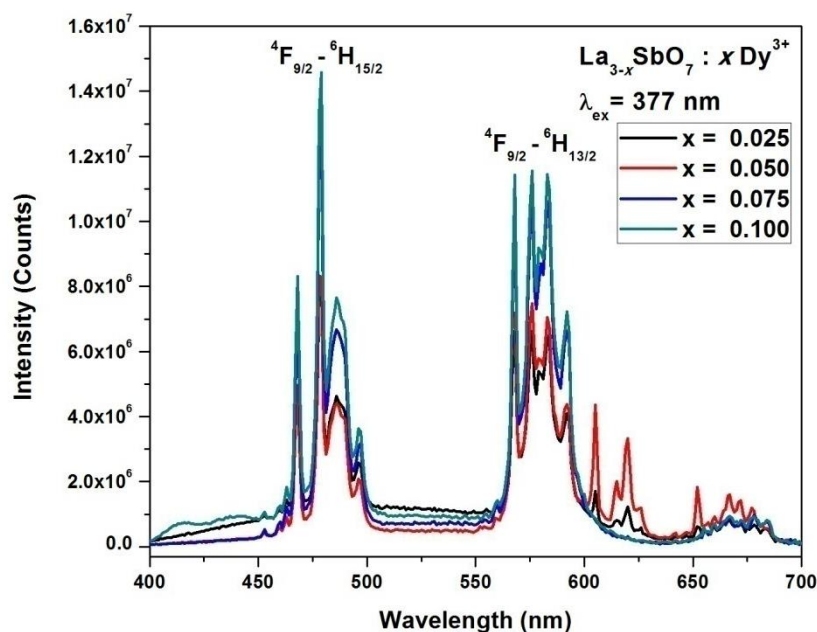


Figure 4.15 : Emission spectra of $\text{La}_{3-x}\text{SbO}_7 : x\text{Dy}^{3+}$ ($x = 0.025, 0.050, 0.075, 0.100$) under 377 nm excitation

It is observed that f-f transition intensities are improved with an increase in the Dy^{3+} concentration. The emission spectra profiles of $\text{La}_{3-x}\text{SbO}_7 : x\text{Dy}^{3+}$ ($x = 0, 0.025, 0.050, 0.075, 0.100$) samples under 344 nm, 358 nm and 378 nm excitations are shown in Figure 4.13, Figure 4.14 and Figure 4.15 respectively. The excitation and emission peak shape and the peak position has no much observable differences except in the emission intensity. From the emission spectra under all the excitation wavelengths, it is observed the emission intensity of the samples are increasing with the increase in the Dy^{3+} doping concentration and no concentration quenching is obtained under all the excitation wavelengths upto 100 mol% for $\text{La}_{3-x}\text{SbO}_7 : x\text{Dy}^{3+}$ phosphors.

4.4. Conclusions

In the present study, new white light emitting single phase phosphors based on a ternary rare earth oxide systems $\text{La}_{2.95}\text{MO}_7 : 0.050\text{Dy}^{3+}$ ($M = \text{Sb}, \text{Ta}, \text{Nb}$) and $\text{La}_{3-x}\text{SbO}_7 : x\text{Dy}^{3+}$ ($x = 0.025, 0.050, 0.075, 0.100$) were developed successfully. The photoluminescence studies indicate that the phosphor material can be easily excited by the emission outputs of UV and blue LED chip and the phosphor samples exhibit the characteristic blue and yellow f-f transitions of Dy^{3+} assigned to the forced electric dipole transition of $^4\text{F}_{9/2} \rightarrow ^6\text{H}_{13/2}$ and the magnetic dipole transition of $^4\text{F}_{9/2} \rightarrow ^6\text{H}_{15/2}$ respectively with excellent chromaticity coordinates. Owing to the excellent

photoluminescence characteristics, the obtained phosphors have potential applications for designing phosphor converted (pc) white-light emitting materials.

Chapter 5

Luminescence properties of Dy³⁺ in Ca₂Ln_{3-x}Nb₃O₁₄

(Ln = Gd, La, Y) host lattices

Abstract

Pyrochlore based single phase white emitting Dy^{3+} doped $Ca_2Ln_{3-x}Nb_3O_{14}$ ($Ln = Gd, La, Y$) phosphors were prepared by a conventional high temperature solid state reaction. The structural characterizations of the samples were performed by powder X-ray diffraction analysis and the phase and the structure were identified. The photoluminescence excitation and emission measurements were carried out to study the influence of structural disorder on the photoluminescence properties of the phosphors. The phosphors are excitable under n-UV wavelengths at 350 nm, 388 nm and blue light at 453 nm which is clearly evidenced from the photoluminescence excitation spectra. Sharp and broader emission peaks in the visible region at 479 nm and 489 nm (blue) and at 579 nm (yellow) upon UV excitation resulted from the characteristic intraconfigurational f-f magnetic dipole transition of ${}^4F_{9/2} \rightarrow {}^6H_{15/2}$ and the forced electric dipole transition of ${}^4F_{9/2} \rightarrow {}^6H_{13/2}$ of Dy^{3+} ions respectively. The emission has a white color by the combination of the blue and the yellow emissions of comparable intensities. Therefore, $Ca_2Ln_{3-x}Nb_3O_{14} : x Dy^{3+}$ are ideal candidates as phosphors and can be useful for pc-WLED applications.

5.1 Introduction

Research on inorganic luminescent materials or phosphors has achieved a new standard in the lighting industry and these materials find applications in plasma display panels and field emission displays. The current phosphors used for pc-WLEDs based on the blue emission from an InGaN chip and the yellow emission from a YAG Ce³⁺ phosphor. The blue LED plays a vital part in the white light generation and is strongly influenced by the drive current, quantity of phosphor and the temperature. The UV LED chip emits light at a wavelength shorter than 400 nm and replaces the blue LED chip used in the first method. UV LED chip approach offers good color stability as all the colors are produced by phosphors. Poor luminescence efficiency due to the strong reabsorption of emission colours produced by the phosphors for white light generation is a major drawback of the UV LED chip. Therefore the search of single phase white light emitting phosphors are essential for developing luminescent materials for white light generation.

The effect of the partial substitution of smaller cations on both A and B sites of the pyrochlore structure and the variation in the luminescence properties with respect to these parameters has been a subject of interest. The luminescence properties can be enhanced by destroying the symmetry of the pyrochlore A site from a perfect inversion centre which in turn leads to the distortion of the scalenohedra. The appearance of higher symmetry due to the displacive disorder has a dependence on the photoluminescence properties. There is a lot of literature relating to the substitution of small cation from the B site to the A site of the pyrochlore oxide. The occupation of medium size cations from A site to B site is much less investigated and in the present work, the variation in the photoluminescence properties due to the partial substitution of the medium size cation on both the A and B site is investigated. In the cubic pyrochlore structure, the A sites are occupied by Ca²⁺ and Y³⁺ and B site by Nb⁵⁺ ions. The medium size ions at the A site has a chance of occupying the B site if the number of ions in the A site is greater than that at the B site.

5.2 Experimental section

5.2.1 Synthesis

Preparation of $Ca_2Ln_{3-x}Nb_3O_{14} : x Dy^{3+}$ ($Ln = La, Gd, Y$) ($x = 0.050$) samples:

In the present work, $Ca_2Ln_{3-x}Nb_3O_{14} : x Dy^{3+}$ ($Ln = La, Gd, Y$) ($x = 0.050$) samples were developed by the conventional high temperature ceramic route by taking $CaCO_3$, Gd_2O_3 , La_2O_3 , Y_2O_3 , Nb_2O_5 , Dy_2O_3 (All chemicals are from Sigma Aldrich with 99.99% purity) as the starting raw materials. The right stoichiometric amounts of these chemicals were taken and then mixed nicely in an agate mortar using acetone medium. After homogeneous mixing the product was kept for drying in an air oven maintained at $100^\circ C$ temperature. The above process of mixing and drying was done many times to get a homogeneous product. The obtained products were made into a pellet and first calcined at $1400^\circ C$ for 6 h for all the samples on an alumina plate in an electrically heated furnace. Then the calcination was repeated at $1400^\circ C$ for 6 h for the Gadolinium and Lanthanum samples with an intermittent powdering. The calcination was again repeated at $1500^\circ C$ for 6 h for the Lanthanum sample with an intermittent powdering and the final single phase of all the samples are obtained. The calcined pellet was made into a fine powder for further characterizations.

5.2.2 Characterisation techniques

The crystalline structure was verified by the X-ray powder diffraction (XRD) analysis using powder X-ray diffractometer (X'Pert Pro PANalytical). The diffraction patterns were recorded in the 2θ scan range from 10° to 90° with a step size of 0.016° with the system operating at 40 kV/30 mA with a Ni filtered Cu-K α radiation ($\lambda=0.15406$ nm). The photoluminescence measurements were made on a Fluorolog HORIBA fluorescence spectrophotometer with a Xe lamp (450 W) as the excitation source. CIE chromaticity coordinates were obtained using the software CIE calculator.

5.3 Results and discussion

5.3.1 Powder X-ray diffraction analysis

Powder X-ray diffraction patterns of $Ca_2Ln_{3-x}Nb_3O_{14} : x Dy^{3+}$ ($Ln = La, Gd, Y$) ($x = 0.050$) phosphors are shown in Figure 5.1, Figure 5.2 and Figure 5.3 respectively. The sharp and intense peaks in the diffraction pattern confirm that the samples are highly crystalline. $Ca_2La_3Nb_3O_{14}$ and $Ca_2Y_3Nb_3O_{14}$ samples can be assigned to cubic phase with

a space group $Fd-3m$ (227) and can be indexed well with the standard values of PDF card no. 01-081-0841 whereas the $Ca_2Gd_3Nb_3O_{14}$ sample can be indexed as a fluorite phase.

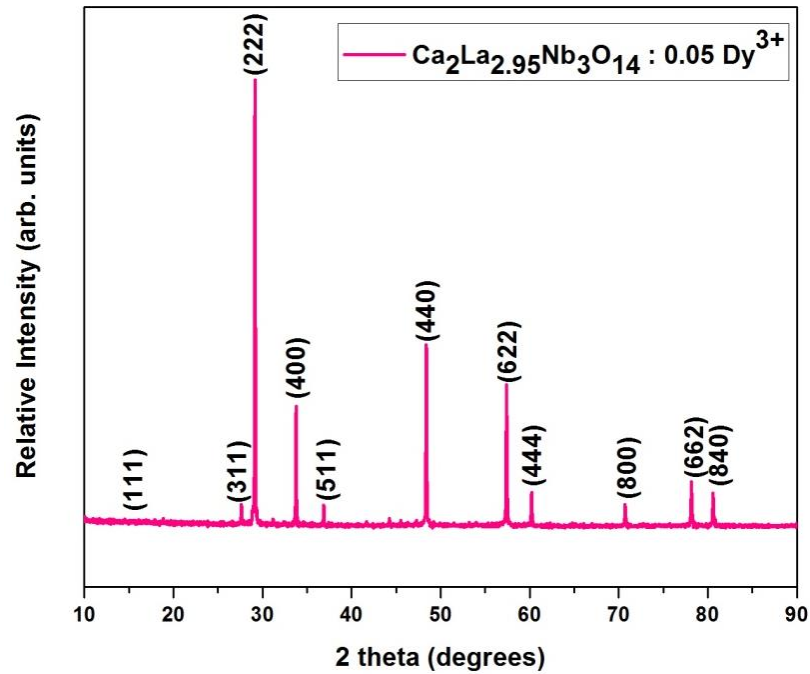


Figure 5.1 : Powder X-ray diffraction patterns of $Ca_2La_{2.95}Nb_3O_7 : 0.05 Dy^{3+}$.

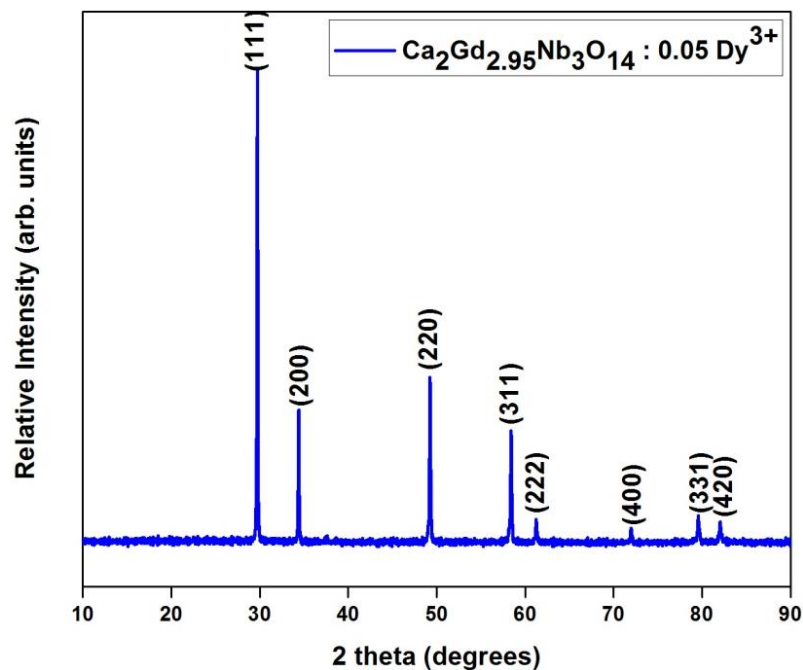


Figure 5.2: Powder X-ray diffraction patterns of $Ca_2Gd_{2.95}Nb_3O_7 : 0.05 Dy^{3+}$.

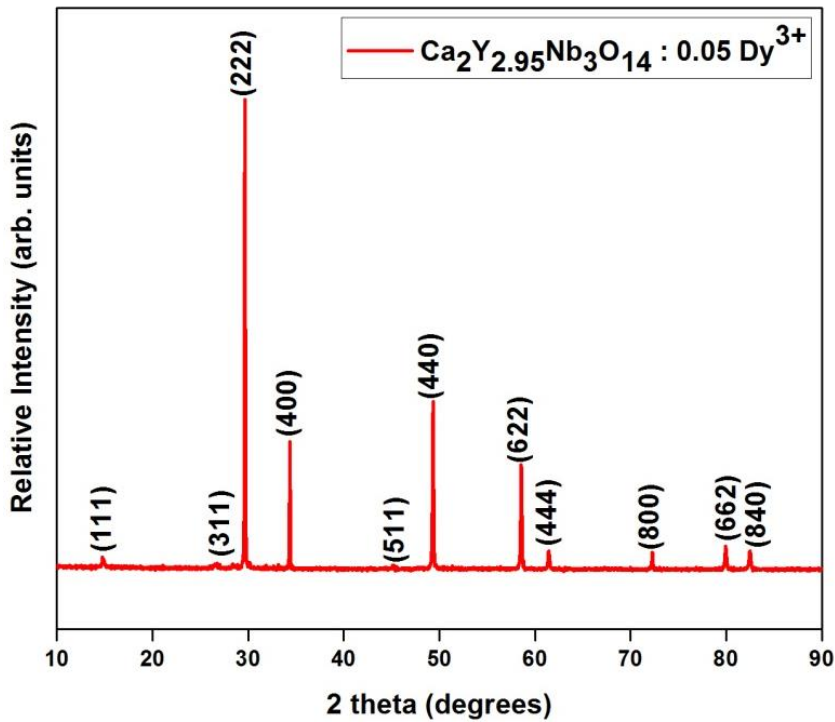


Figure 5.3: Powder X-ray diffraction patterns of $\text{Ca}_2\text{Y}_{2.95}\text{Nb}_3\text{O}_7 : 0.05 \text{Dy}^{3+}$.

The decrease in the intensity of the characteristic (111) superstructure peak of the pyrochlore structure thereby reducing the pyrochlore D_{3d} symmetry which also conforms the incorporation of Dy^{3+} ions into the lattice. On account of the matching ionic radius and valency, Dy^{3+} ions are expected to occupy the Ln sites in the crystal lattice.

5.3.2 Photoluminescence studies

The excitation spectra of $\text{Ca}_2\text{Ln}_{3-x}\text{Nb}_3\text{O}_{14} : x \text{Dy}^{3+}$ ($\text{Ln} = \text{La}, \text{Gd}, \text{Y}$) ($x = 0.050$) for an emission at 479 nm, 489 nm and 579 nm are shown in Figure 5.4, Figure 5.5 and Figure 5.6 respectively. The excitation spectra consists of a weak charge transfer band from 250 nm to 300 nm followed by a series of sharp and intense f-f transitions of the Dy^{3+} ions. The sharp peaks beyond 300 nm due to the intra-configurational f-f transitions of Dy^{3+} peaks at 350 nm (${}^6\text{H}_{15/2} \rightarrow {}^4\text{I}_{11/2} + {}^4\text{M}_{15/2} + {}^6\text{P}_{7/2}$), 388 nm (${}^6\text{H}_{15/2} \rightarrow {}^4\text{M}_{21/2} + {}^4\text{I}_{13/2} + {}^4\text{F}_{7/2} + {}^4\text{M}_{19/2} + {}^4\text{K}_{17/2}$) and 453 nm (${}^6\text{H}_{15/2} \rightarrow {}^4\text{I}_{9/2} + {}^4\text{I}_{15/2}$). The sharp and intense excitation peaks in the UV region matches well to the outputs of the UV led chips. The absorption peaks of the intra-configurational 4f transitions of Dy^{3+} increases with increasing concentration of dysprosium. The enhancement in the emission of Dy^{3+} is

mainly due to the increased absorption of ${}^6H_{15/2} \rightarrow {}^6P_{7/2}$, ${}^6H_{15/2} \rightarrow {}^6P_{9/2}$ and ${}^6H_{15/2} \rightarrow {}^4F_{7/2} + {}^4I_{13/2}$ transitions.

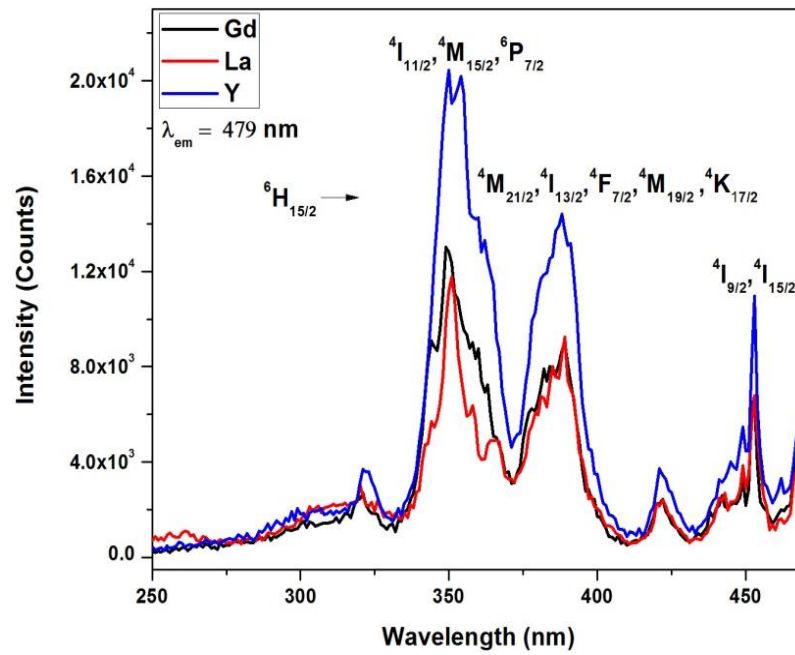


Figure 5.4: Excitation spectra of $Ca_2Ln_{2.95}Nb_3O_7 : 0.05 Dy^{3+}$ ($Ln = La, Gd, Y$) for an emission at 479 nm.

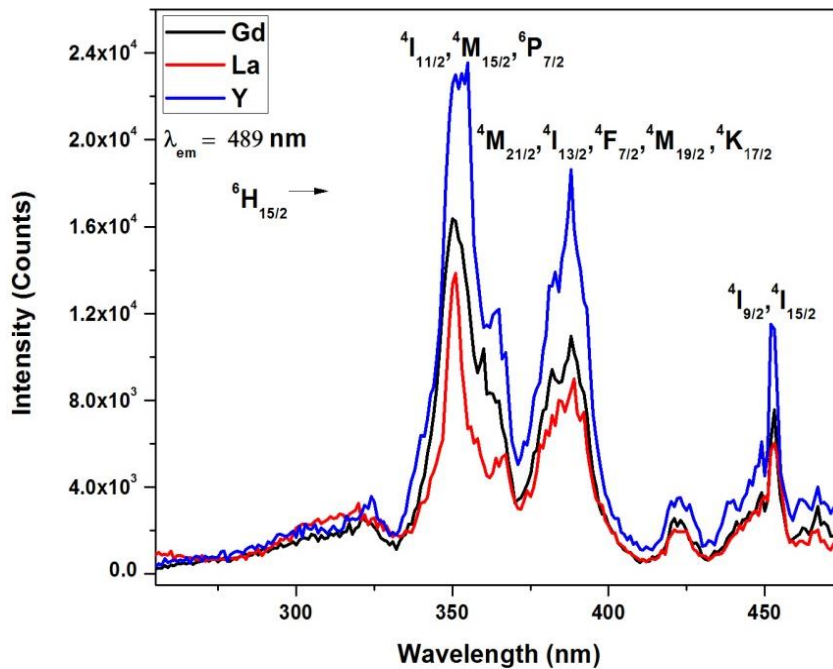


Figure 5.5 : Excitation spectra of $Ca_2Ln_{2.95}Nb_3O_7 : 0.05 Dy^{3+}$ ($Ln = La, Gd, Y$) for an emission at 489 nm.

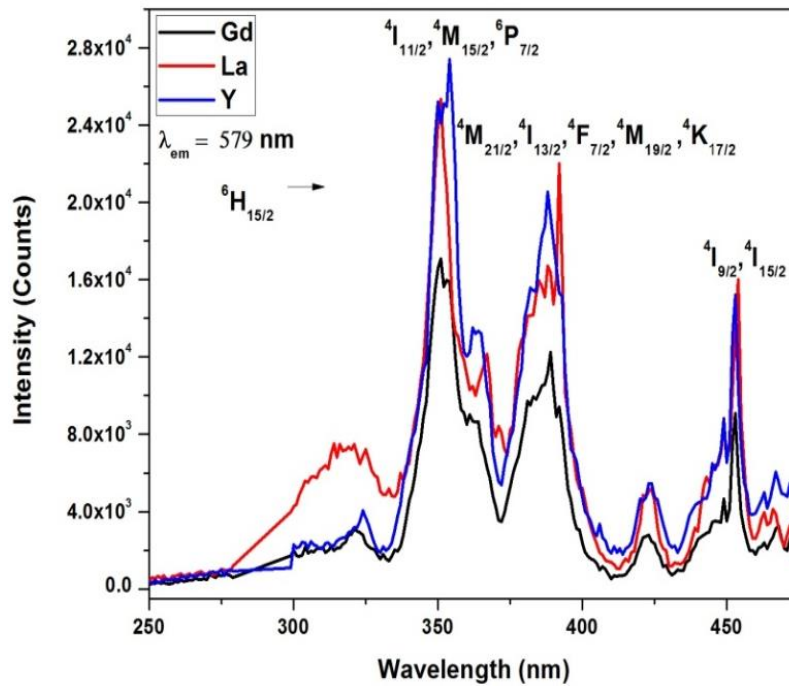


Figure 5.6 : Excitation spectra of $\text{Ca}_2\text{Ln}_{2.95}\text{Nb}_3\text{O}_7 : 0.05 \text{Dy}^{3+}$ ($\text{Ln} = \text{La}, \text{Gd}, \text{Y}$) for an emission at 579 nm.

Photoluminescence emission spectra of $\text{Ca}_2\text{Ln}_{2.95}\text{Nb}_3\text{O}_7 : 0.05 \text{Dy}^{3+}$ ($\text{Ln} = \text{La}, \text{Gd}, \text{Y}$) samples under an excitation of 350 nm, 388 nm and 453 nm are given in Figure 5.7, Figure 5.8 and Figure 5.9 respectively. The luminescence emission properties have been studied upon 350 nm, 388 nm, and 453 nm excitations for the $\text{Ca}_2\text{Ln}_{2.95}\text{Nb}_3\text{O}_7 : 0.05 \text{Dy}^{3+}$ ($\text{Ln} = \text{La}, \text{Gd}, \text{Y}$) samples. Upon all excitations the phosphor samples exhibited sharp peaks in the visible regions at 479 nm, 489 nm and 579 nm which are attributed to the magnetic dipole transition of ${}^4\text{F}_{9/2} \rightarrow {}^6\text{H}_{15/2}$ and the forced electric dipole transition of ${}^4\text{F}_{9/2} \rightarrow {}^6\text{H}_{13/2}$ respectively. A feeble red emission at 664 nm due to the ${}^4\text{F}_{9/2} \rightarrow {}^6\text{H}_{11/2}$ transition is also observed. When Dy^{3+} is situated at a site with low symmetry and without an inversion center, the yellow emission is dominant and the blue emission is stronger when Dy^{3+} ions occupy a site with high symmetry and with an inversion center. The yellow and the blue emission are of comparable intensities and the resultant complementary emission gives white light.

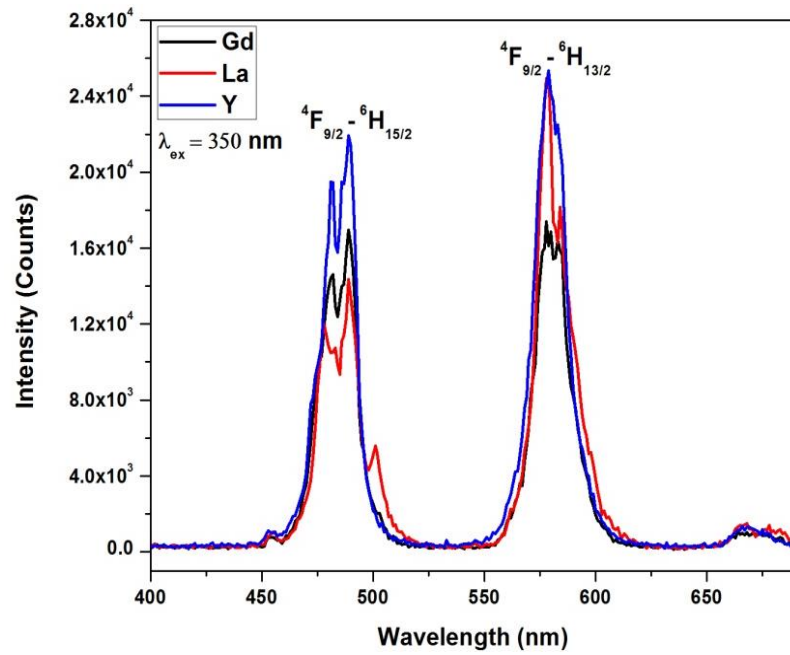


Figure 5.7 : Emission spectra of $Ca_2Ln_{2.95}Nb_3O_7 : 0.05 Dy^{3+}$ ($Ln = La, Gd, Y$) under 350 nm excitation.

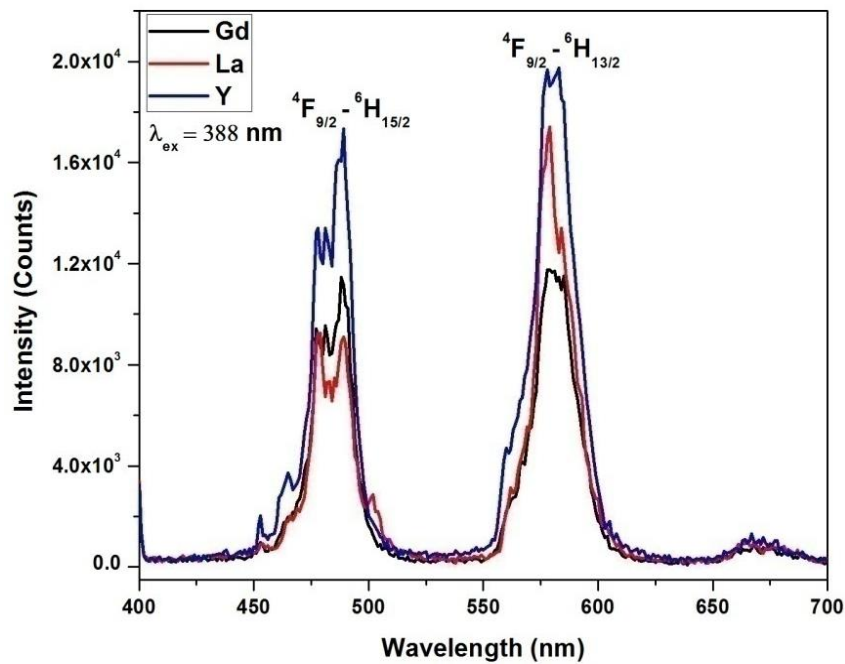


Figure 5.8: Emission spectra of $Ca_2Ln_{2.95}Nb_3O_7 : 0.05 Dy^{3+}$ ($Ln = La, Gd, Y$) under 388 nm excitation.

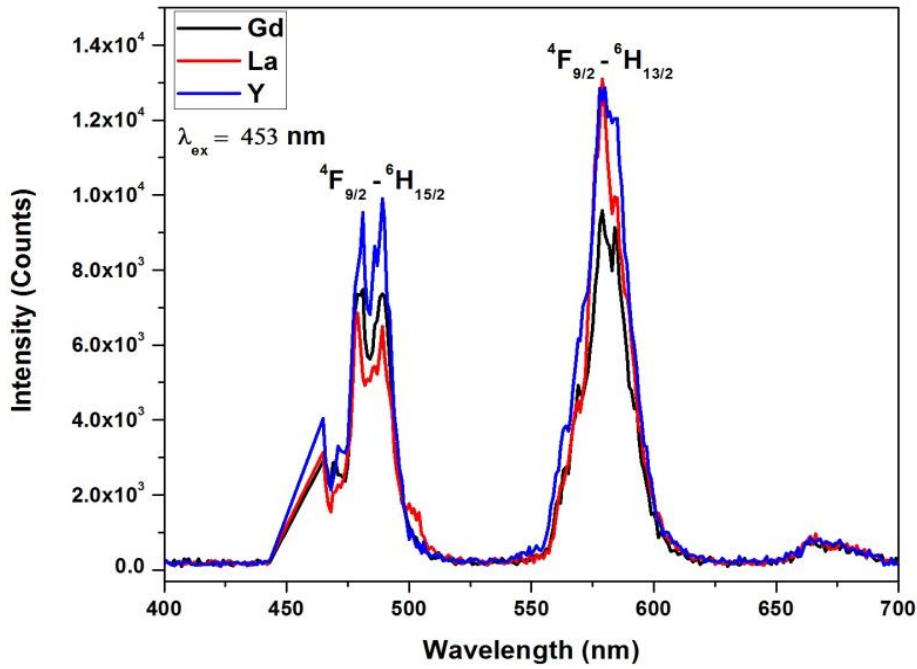


Figure 5.9: Emission spectra of $\text{Ca}_2\text{Ln}_{2.95}\text{Nb}_3\text{O}_7 : 0.05 \text{Dy}^{3+}$ ($\text{Ln} = \text{La}, \text{Gd}, \text{Y}$) under 453 nm excitation.

5.4. Conclusions

$\text{Ca}_2\text{Ln}_{2.95}\text{Nb}_3\text{O}_7 : 0.05 \text{Dy}^{3+}$ ($\text{Ln} = \text{La}, \text{Gd}, \text{Y}$) phosphors were prepared by a conventional solid state method. The powder X-ray diffraction studies conform pyrochlore phase for the $\text{Ca}_2\text{La}_3\text{Nb}_3\text{O}_7$ and $\text{Ca}_2\text{Y}_3\text{Nb}_3\text{O}_7$ whereas the $\text{Ca}_2\text{Gd}_3\text{Nb}_3\text{O}_7$ belongs to the fluorite phase. Upon 350 nm, 388 nm, and 453 nm excitation wavelengths the phosphor samples exhibited sharp peaks at 479 nm, 489 nm and 579 nm which are attributed to the magnetic dipole transition of ${}^4\text{F}_{9/2} \rightarrow {}^6\text{H}_{15/2}$ and the forced electric dipole transition of ${}^4\text{F}_{9/2} \rightarrow {}^6\text{H}_{13/2}$ respectively. The $\text{CaLa}_{1-x}\text{NbMoO}_8 : x\text{Dy}^{3+}$ phosphors exhibited excellent luminescent properties in terms of the excitation and emission intensities and CIE values are closer to the NTSC values of white light and can be a potential candidate as a single phase white light emitting phosphor for WLED applications.

Chapter 6

CONCLUSIONS AND FUTURE SCOPE

Conclusions of the Investigations

The work presented in this thesis is an attempt to develop white light emission from a single phase host lattice. A series of Dy^{3+} activated powellite/scheelite based molybdate/tungstate phosphors, pyrochlore based quaternary lanthanide stannates, ternary rare earth antimonates, tantalates, niobates were prepared by the conventional solid state route. The various influencing parameters on the luminescence properties are discussed. Some of the important conclusions drawn from the present study.

- ✚ Molybdate and tungstate based white emitting phosphors were developed which has strong absorption in the near UV and blue region.
- ✚ Stannate based pyrochlore phosphors exhibiting strong white emission under both NUV & blue excitations are developed .
- ✚ By using complex pyrochlore oxides we can control symmetry of A-site cation thereby luminous emission region.
- ✚ Substitution of bigger cations to the A site of pyrochlore enhances the photoluminescence emission properties.
- ✚ The photoluminescence properties can be enhanced by simple compositional adjustments in the quaternary pyrochlore-type phosphors
- ✚ The effect of Dy^{3+} doping concentration on the emission characteristics of La_3SbO_7 phosphors was also discussed and the trend in the photoluminescence properties was analysed. The emission colours of all the doped samples are located in the white light region. The variation in the luminescence properties with the substitution of the rare earths $\text{M} = \text{Nb}, \text{Ta}, \text{Sb}$ in the $\text{La}_3\text{M}_{1-x}\text{O}_7 : x \text{Dy}^{3+}$ is also discussed.
- ✚ Influence of various lanthanide ion (La, Gd, Y) substitution on the Dy^{3+} photoluminescence properties in $\text{Ca}_2\text{Ln}_3\text{Nb}_3\text{O}_7 : x \text{Dy}^{3+}$ host structures was studied. These phosphors exhibit the blue yellow emissions of Dy^{3+} ions with equally competing intensities and emit white light.

Future scope

The phosphors synthesized in this work can be used for practical purposes if further studies are carried out on the influencing parameters on the luminescence properties. Some of the aspects that can be improved from the present systems are listed as follows.

- ✚ Effect of synthesis methods of phosphors on the enhanced luminescent properties thereby controlling the morphology to spherical symmetry to increase the absorption strength.
- ✚ The role of distribution of particle size on the variation of luminescence emission intensity.
- ✚ The quantum efficiency of phosphors depending on the position and intensity of the charge transfer band.
- ✚ Effect of codoping with various activators to get a full colour emission
- ✚ Optimization of thermal stability of developed phosphors
- ✚ Incorporation of developed white phosphors for fabrication of LED chips.

REFERENCES

1. Blasse G., Chemistry and physics of R –activated phosphors. In : Gschneidner K. A. Jr., Eyring L., editors. Handbook on the Physics and Chemistry of Rare-Earths, North-Holland : Amsterdam, **1979**.
2. Blasse G., Energy Transfer in Oxidic Phosphors, Philips Res. Repts, 24, **1969**, 131 – 144.
3. Blasse G., Grabmaier B. C., Luminescent Materials, Berlin : Springer - Verlag; **1994**.
4. Cheng H., Wang L., Lu Z., A general aqueous sol-gel route to $\text{Ln}_2\text{Sn}_2\text{O}_7$ nanocrystals, Nanotechnology, 19, **2008**, 025706(7 pp).
5. Deng Y., Yi S., Huang J., Xian J., Zhao W., White light emission and energy transfer in $\text{Dy}^{3+}/\text{Eu}^{3+}$ co-doped BaLa_2WO_7 phosphors, J. Mater. Res. Bull., 57, **2014**, 85 – 90.
6. Du P., Bharat L. K., Guan X. Y., Yu J. S., Synthesis and luminescence properties of color-tunable Dy^{3+} -activated CaWO_4 phosphors, J. Appl. Phys., 117, **2015**, 083112-1 – 083112-6.
7. Dutta S., Som S., Sharma S. K., Luminescence and photometric characterization of K^+ compensated $\text{CaMoO}_4:\text{Dy}^{3+}$ nanophosphors, Dalton Trans., 42, **2013**, 9654 – 9661.
8. Francis L. T., Rao P. P., Thomas M., Mahesh S. K., Reshmi V. R., Thampi V. D. S., Mater. Lett., 81, **2012**, 142 – 144.
9. Francis T. L., Rao P. P., Mahesh S. K., Sreena T. S., Babu S. P., Effect of host structure on the photoluminescence properties of $\text{Ln}_3\text{TaO}_7 : \text{Eu}^{3+}$ red phosphors, Opt. Mater., 52, **2016**, 134 – 143.
10. Fujihara S., Tokumo K., Multiband Orange-Red Luminescence of Eu^{3+} Ions Based on the Pyrochlore-Structured Host Crystal, Chem. Mater., 17, **2005**, 5587 – 5593.
11. Hatakoshi G. I., Phosphor Handbook, ed. Yen W. M., Shionoya S., Yamamoto H., CRC Press, New York, **2007**, 191 – 214.
12. Jena P., Gupta S. K., Natarajan V., Sahu M., Satyanarayana N., Venkateswarlu M., Structural characterization and photoluminescence properties of sol-gel derived nanocrystalline $\text{BaMoO}_4:\text{Dy}^{3+}$, J. Lumin., 158, **2015**, 203 – 210.
13. Justel T., Nikol H., Ronda C., New Developments in the Field of Luminescent Materials for Lighting and Displays, Angew. Chem. Int. Ed., 37, **1998**, 3084 – 3103.
14. Kaczmarek A. M., Deun R. V., Rare earth tungstate and molybdate compounds – from 0D to 3D architectures, Chem. Soc. Rev., 42, **2013**, 8835 – 8848.
15. Kaufman J. E., Christensen J. F., Lighting Handbook, Waverly Press, Maryland **1972**.

16. Kazakova L. I., Bykov I. S., Dubovsky A. B., The luminescence of rare-earth tantalate single crystals, *J. Lumin.*, 72 – 74, **1997**, 211 – 212.
17. Kennedy B. J., Hunter B. A., Howard C. J., Structural and Bonding Trends in Tin Pyrochlore Oxides, *J. Solid State Chem.*, 130, **1997**, 58 – 65.
18. Khan M. N., Understanding LED illumination, CRC Press, Taylor & Francis group, Florida, **2014**.
19. Lin C. C., Liu R. S., Advances in Phosphors for Light-emitting Diodes, *J. Phys. Chem. Lett.*, 2, **2011**, 1268 – 1277.
20. Liu X., Liu Y., Yan D., Zhu H., Liu C., Xu C., Liu Y., Wang X., Single-phased white-emitting $12\text{CaO} \cdot 7\text{Al}_2\text{O}_3\text{:Ce}^{3+}, \text{Dy}^{3+}$ phosphors with suitable electrical conductivity for field emission displays, *J. Mater. Chem.*, 22, **2012**, 16839 – 16843.
21. Mahesh S. K., Rao P. P., Thomas M., Francis T. L., Koshy P., Influence of Cation Substitution and Activator Site Exchange on the Photoluminescence Properties of Eu^{3+} -Doped Quaternary Pyrochlore Oxides, *Inorg. Chem.*, 52, **2013**, 13304 – 13313.
22. Mahesh S. K., Rao P. P., Thomas M., Radhakrishnan A. N., Koshy P., Photoluminescence characteristics of new stannate pyrochlore based red phosphors: $\text{CaLaSnNbO}_7\text{:Eu}^{3+}$, *J. Mater. Sci.: Mater. Electron.*, 23, **2012**, 1605 – 1609.
23. McKittrick J., Shea-Rohwer L. E., Review: Down Conversion Materials for Solid-State Lighting, *J. Am. Ceram. Soc.*, 97 [5], **2014**, 1327 – 1352.
24. Naidu S. A., Boudin S., Varadaraju U. V., Raveau B., A crystal chemical approach to tuning of emission properties in rare earth doped ternary niobates, *J. Mater. Chem.*, 22, **2012**, 1088 – 1093.
25. Narukawa Y., Ichikawa M., Sanga D., Sano M., Mukai T., White light emitting diodes with super-high luminous efficacy, *J. Phys. D: Appl. Phys.*, 43, **2010**, 354002 (6 pp).
26. Nobre M. A. L., Lanfredi S., Dielectric spectroscopy on $\text{Bi}_3\text{Zn}_2\text{Sb}_3\text{O}_{14}$ ceramic: an approach based on the complex impedance, *J. Phys. Chem. Solids*, 64, **2003**, 2457 – 2464.
27. Phillips J. M., Coltrin M. E., Crawford M. H., Fischer A. J., Krames M. R., Mach R. M., Mueller G. O., Ohno Y., Rohwer L. E. S., Simmons J. A., Tsao J. Y., Research challenges to ultra-efficient inorganic solid-state lighting *Laser & Photon. Rev.* 1, No. 4, **2007**, 307 – 333.
28. Ronda C., Luminescence: From Theory to Applications, ed. Ronda C., Wiley-VCH Verlag GmbH & Co. KGaA, Weinheim, Germany, 2008.

29. Shang M., Li C., Lin J., How to produce white light in a single-phase host?, *Chem. Soc. Rev.*, 43, **2014**, 1372 – 1386.
30. Shannon R. D., Revised Effective Ionic Radii and Systematic Studies of Interatomic Distances in Halides and Chalcogenides, *Acta Cryst.*, A32, **1976**, 751 – 767.
31. Sharma K. G., Singh N. R., Synthesis and luminescence properties of $\text{CaMO}_4:\text{Dy}^{3+}$ (M = W, Mo) nanoparticles prepared via an ethylene glycol route, *New J. Chem.*, 37, **2013**, 2784 – 2791.
32. Soares M. R. N., Soares M. J., Fernandes A. J. S., Rino L., Costa F. M., Monteiro T., $\text{YSZ}:\text{Dy}^{3+}$ single crystal white emitter, *J. Mater. Chem.*, 21, **2011**, 15262 – 15265.
33. Stevens W. R., *Building Physics: Lighting*, Pergamon Press, London, **1969**.
34. Su Q., Pei Z., Chi L., Zhang H., Zhang Z., Zou F., The yellow-to-blue intensity ratio (Y/B) of Dy^{3+} emission, *J. Alloy. Compd.*, 192, **1993**, 25 – 27.
35. Subramanian M. A., Aravamudan G., Subba Rao G. V., Oxide Pyrochlores – A Review, *Prog. Solid St. Chem.*, 15, **1983**, 55 – 143.
36. Thomas M., Rao P. P., Deepa M., Chandran M. R., Koshy P., Novel powellite-based red-emitting phosphors: $\text{CaLa}_{1-x}\text{NbMoO}_8:x\text{Eu}^{3+}$ for white light emitting diodes, *J. Solid State Chem.* 182, **2009**, 203 – 207.
37. Thomas M., Rao P. P., Mahesh S. K., Kumari L. S., Koshy P., Luminescence properties of Eu^{3+} , Bi^{3+} coactivated CaLaNbWO_8 red phosphors under near UV and blue excitations, *Phys. Status Solidi A*, 208[9], **2011**, 2170 – 2175.
38. Wang J., Cheng Y., Huang Y., Cai P., Kim S.I., Seo H. J., Structural and luminescent properties of red-emitting Eu^{3+} -doped ternary rare earth antimonates R_3SbO_7 (R = La, Gd, Y), *J. Mater. Chem. C*, 2, **2014**, 5559 – 5569.
39. Wang S. M., Lu M. K., Zhou G. J., Zhou Y. Y., Zhang H. P., Wang S. F., Yang Z. S., Synthesis and luminescence properties of $\text{La}_{2-x}\text{RE}_x\text{Sn}_2\text{O}_7$ (RE = Eu and Dy) phosphor nanoparticles, *Mater. Sci. Eng. B*, 133, **2006**, 231 – 234.
40. Wang S. M., Xiu Z. L., Lu M. K., Zhang A. Y., Zhou Y. Y., Yang Z. S., Combustion synthesis and luminescent properties of Dy^{3+} - doped $\text{La}_2\text{Sn}_2\text{O}_7$ nanocrystals, *Mater. Sci. Eng., B*, 143, **2007**, 90 – 93.
41. Ye S., Xiao F., Pan Y. X., Ma Y. Y., Zhang Q. Y., Phosphors in phosphor-converted white light-emitting diodes : Recent advances in materials, techniques and properties, *Mater. Sci. Eng., R* 71, **2010**, 1 – 34.
42. Yen W. M., Shionoya S., Yamamoto H., *Fundamentals of Phosphors*. 2nd ed. Boca Raton: CRC Press; **2007**, p. 199-200.

43. Yen W. M., Shionoya S., Yamamoto H., *Fundamentals of Phosphors*. 2nd ed. Boca Raton: CRC Press; **2007**, p. 96-97.
44. Yin X., Shi L., Wei A., Wan D., Wang Y., Huang F., Effect of structural packing on the luminescence properties in tungsten bronze compounds $M_2KNb_5O_{15}$ ($M = Ca, Sr, Ba$), *J. Solid State Chem.*, **192**, **2012**, 182 – 185.
45. Yuhua W., Ge Z., Shuangyu X., Qian W., Yanyan L., Quansheng W., Chuang W., Xicheng W., Xin D., Wanying G., *J. Rare Earth*, **33** [1], **2015**, 1 – 12.
46. Zhang A., Lu M., Zhou G., Wang S., Zhou Y, Combustion synthesis and photoluminescence of Eu^{3+} , Dy^{3+} - doped $La_2Zr_2O_7$ nanocrystals, *J. Phys. Chem. Solids*, **67**, **2006**, 2430 – 2434.
47. Zhao W. Y., An S. L., Fan B., Li S. B., Dai Y. T., Photoluminescence and cathodoluminescence properties of a novel $CaLaGa_3O_7:Dy^{3+}$ phosphor, *Chin. Sci. Bull.*, **57**, **2012**, 827 – 831.
48. Zhou Y., Qiu Z., Lu M., Ma Q., Zhang A., Zhou G., Zhang H., Yang Z., Photoluminescence Characteristics of Pure and Dy-Doped $ZnNb_2O_6$ Nanoparticles Prepared by a Combustion Method, *J. Phys. Chem. C*, **111**, **2007**, 10190 – 10193.
49. Zhu H., Jin D., Zhu L., Yang H., Yao K., Xi Z., A general hydrothermal route to synthesis of nanocrystalline lanthanide stannates: $Ln_2Sn_2O_7$ ($Ln = Y, La-Yb$), *J. Alloys Compd.*, **464**, **2008**, 508 – 513.

List of publications in SCI journals

1. **Parvathi S. Babu**, P. Prabhakar Rao, Sreena T.S., White light emitting stannate pyrochlore based single phase phosphor $\text{CaLa}_{1-x}\text{SnNbO}_7 : x \text{Dy}^{3+}$ for pc-white LED applications, *Journal of Material Science Materials in Electronics*, (2019), 30, 16174–16183.
2. **Parvathi S. Babu**, P. Prabhakar Rao, S.K. Mahesh, T.Linda Francis, T.S. Sreena, Studies on the photoluminescent properties of a single phase white light emitting phosphor $\text{CaLa}_{1-x}\text{NbMoO}_8 : x \text{Dy}^{3+}$ for pc-white LED applications, *Materials Letters*, (2016), 170, 196–198.
3. **Parvathi S. Babu**, P. Prabhakar Rao, Sreena T.S., Optical studies on the single phase white emitting phosphor $\text{La}_3\text{M}_{1-x}\text{O}_7 : x \text{Dy}^{3+}$ (M = Nb, Ta, Sb) (Manuscript under preparation).
4. **Parvathi S. Babu**, P. Prabhakar Rao, Sreena T.S., Influence of Lanthanide ion substitution on the photoluminescent properties of white light emitting phosphor $\text{Ca}_2\text{Ln}_{3-x}\text{Nb}_3\text{O}_{14} : x \text{Dy}^{3+}$ (Ln = La, Gd, Y) (Manuscript under preparation).
5. T. S. Sreena, P. Prabhakar Rao, Athira K. V. Raj, **Parvathi S. Babu**, Influence of Structural Disorder on the Photoluminescence Properties of Eu^{3+} Doped Red Phosphors: $\text{Ca}_2\text{Y}_{3-x}\text{Nb}_3\text{O}_{14} : x \text{Eu}^{3+}$, *Chemistry Select*, (2016), 1, 3413 -3422.
6. T. Linda Francis, P. PrabhakarRao, S. K. Mahesh, T. S. Sreena, **S. Parvathi Babu**, Effect of host structure on the photoluminescence properties of $\text{Ln}_3\text{TaO}_7 : \text{Eu}^{3+}$ red phosphors, *Optical Materials* (2015), 52, 134-143.
7. Linda T. Francis, P. PrabhakarRao, S. K. Mahesh, T. S. Sreena, **Parvathi S. Babu**, Novel red phosphors $\text{Gd}_2\text{GaTaO}_7 : \text{Eu}^{3+}$, Bi^{3+} for white LED applications, *Journal of Material Science Materials in Electronics* (2015) 26, 5743-5747.
8. T. S. Sreena, P. PrabhakarRao, T. Linda Francis, Athira K. V. Raj, **Parvathi S. Babu**, Structural and photoluminescence properties of stannate based displaced pyrochlore-type red phosphors : $\text{Ca}_{3-x}\text{Sn}_3\text{Nb}_2\text{O}_{14} : x \text{Eu}^{3+}$, *Dalton Transactions* (2015), 44, 8718–8728.

List of Conference proceedings

1. **Parvathi S. Babu**, P. PrabhakarRao*, Mahesh S.K., Linda Francis T., Reshmi V.R., Sreena T. S., Studies on the Optical Properties of $\text{Ca}_{0.8}\text{Sr}_{0.2}\text{La}_{0.965}\text{NbMoO}_8 : 0.035 \text{Dy}^{3+}$ Phosphors, *National Seminar on Photonics and its Applications (NSPA-2015)*.
2. **Parvathi S. Babu**, P. PrabhakarRao, Mahesh S. K., Linda Francis T., Resmi V. R., Sreena T. S., Enhanced Luminescence in $\text{CaMoO}_4 : \text{Dy}^{3+}$ phosphors prepared by Solid State Method, *International Conference on Science, Technology and Applications of Rare earths (ICSTAR 2015), Thiruvananthapuram, Kerala, 2015*.
3. **Parvathi S. Babu**, P. PrabhakarRao, S. K. Mahesh, T. Linda Francis, V. R. Reshmi, T. S. Sreena, Studies on the Optical Properties of $\text{Dy}^{3+}/\text{Eu}^{2+}$ Co-Doped CaSrLaNbMoO_8 Phosphors, *5th International Conference on Luminescence and its Applications (ICLA), Bangalore, 2015*.
4. **Parvathi S. Babu**, P. PrabhakarRao, Mahesh S.K., Linda Francis T., Reshmi V.R., Sreena T.S., Photoluminescence studies of $\text{CaLaNbMoO}_8 : \text{Dy}^{3+}$ for full color emission phosphors, *27th Kerala Science Congress, Alappuzha, 2015*.
5. Sreena T. S., P. Prabhakar Rao, T. Linda Francis, Athira K.V. Raj, **Parvathi S. Babu**, Synthesis and Characterization of Eu^{3+} doped Pyrochlore-type Red Phosphors $\text{Ca}_3\text{Sn}_3\text{M}_2\text{O}_{14}$ (M = Nb, Sb, Ta) for White Light Emitting Diode Applications, *NSPA, 2015*.
6. Sreena T. S., P. Prabhakar Rao, T. Linda Francis, Athira K.V. Raj, **Parvathi S. Babu**, Synthesis and Characterization of Eu^{3+} Doped Pyrochlore-Type Red Phosphors $\text{Ca}_3\text{Sn}_3\text{M}_2\text{O}_{14}$ (M = Nb, Sb and Ta) for White Light Emitting Diode Applications, *International Conference on Science, Technology and Applications of Rare earths (ICSTAR 2015), Thiruvananthapuram, Kerala, 2015*.
7. S. K. Mahesh, P. Prabhakar Rao, T. Linda Francis, T. S. Sreena, Athira K. V. Raj, **Parvathi S. Babu** and Peter Koshy, Enhanced Red Luminescence in Eu^{3+} - Ion Activated Quaternary Pyrochlore Oxides Through Compositional Modification, *5th International Conference on Luminescence and its Applications (ICLA), Bangalore, 2015*.
8. S. K. Mahesh, P. PrabhakarRao, T. Linda Francis, T. S. Sreena, Athira K. V. Raj, **Parvathi S. Babu** and Peter Koshy, Eu^{3+} Doped Intense Red Emitting Fergusonite

- Phosphors for pc-WLED Applications, *5thInternational Conference on Luminescence and its Applications (ICLA), Bangalore, 2015.*
9. T. Linda Francis, P. PrabhakarRao, S. K. Mahesh, V. R. Reshmi, T. S. Sreena, **Parvathi S. Babu**, Effect of Ba²⁺ substitution in Ln³⁺ site in the photoluminescence properties of Eu³⁺ activated Ln₃MO₇ Red Phosphors, *5thInternational Conference on Luminescence and its Applications (ICLA), Bangalore, 2015.*
 10. T. S. Sreena, P. PrabhakarRao, S. K. Mahesh, T. Linda Francis, Athira K. V. Raj, **Parvathi S. Babu**, Studies on the Photoluminescence Properties of CaMoO₄ : 0.2 Eu³⁺ Red Phosphors by the Addition of SmPO₄, *5thInternational Conference on Luminescence and its Applications (ICLA), Bangalore, 2015.*
 11. Athira K. V. Raj, P. Prabhakar Rao, S. K. Mahesh, T. Linda Francis, T. S. Sreena, **Parvathi S. Babu**, Enhanced Photoluminescence in CeO₂ by Y₂O₃ Addition through Oxygen Vacancy Ordering and the Modification in Cerium Oxidation States, *5thInternational Conference on Luminescence and its Applications (ICLA), Bangalore, 2015.*
 12. Sreena T. S., P. Prabhakar Rao, Athira K. V. Raj, Mahesh S. K., Linda Francis, Reshmi V. R., **Parvathi S. Babu**, Photoluminescence of pyrochlore type red emitting phosphors, *National Conference on Advanced Technologies for Materials Processing and Diagnostics, (ISAS) 2014*